Climate reconstructions from ice cores: New techniques to understand the information preserved in the South Pole ice core

Emma Carolyn Kahle

A dissertation
submitted in partial fulfillment of the
requirements for the degree of

Doctor of Philosophy

University of Washington

2020

Reading Committee:

Eric J. Steig, Chair

Michelle R. Koutnik

Edwin D. Waddington

Program Authorized to Offer Degree:
Department of Earth and Space Sciences

University of Washington

Abstract

Climate reconstructions from ice cores: New techniques to understand the information preserved in the South Pole ice core

Emma Carolyn Kahle

Chair of the Supervisory Committee:

Professor Eric J. Steig

Department of Earth and Space Sciences

Polar ice cores preserve information about past changes in climate and ice dynamics. Studying changes that have occurred in the past improves understanding of Earth's climate system. Large climate changes, such as the most recent glacial-interglacial transition, provide opportunities to detect a strong signal in changes within the climate system. In this thesis I develop new techniques for interpreting information from ice-core records in order to create robust reconstructions of past climate change. The South Pole ice-core record spans the last 54 ka, encompassing the entirety of the last glacial-interglacial change. I make use of high-resolution data from the South Pole ice core to apply new techniques for interpreting ice-core water-isotope data. I use a novel inverse approach to simultaneously constrain records of temperature, accumulation, and ice-sheet vertical strain from multiple ice-core measurements. The temperature reconstruction improves upon previous ice-core estimates for deglacial warming in East Antarctica and reconciles a longstanding discrepancy between data and model estimates of Antarctic temperature change. I use a simple climate model to examine the physical processes underlying large changes in climate. This thesis improves our understanding of Antarctic climate change over glacial-interglacial transitions.

TABLE OF CONTENTS

ACKNOWLEDGMENTS

I would like to express sincere appreciation to the many people and institutions who have supported this work. First, I am deeply grateful to my adviser, Eric Steig, for his insightful and kindhearted guidance, mentorship, and support throughout my time at the University of Washington. I would also like to thank the members of my PhD committee, Michelle Koutnik, Ed Waddington, and Gerard Roe, for their helpful advice and suggestions in developing this work. My experience in graduate school has been enriched academically and socially by my fellow graduate students in Earth and Space Sciences and in the Program on Climate Change. In particular I would like to thank Brad Markle, Jess Badgeley, Gemma O'Connor, Lindsey Davidge, and Michael Diamond for their friendship and partnership in many projects. I would also like to thank the folks from INSTAAR at the University of Colorado Boulder for their hard work to measure the water isotopes in the South Pole ice core, and especially Tyler Jones for his advice and support. I am grateful to the Program on Climate Change and the University of Washington for the opportunity to pursue this research. Finally, I would like to thank my friends, my frisbee family, and my actual family for their love always.

DEDICATION

to all of my parents:
Charlie and Carrie Kahle
Ruth and Greg Berkman
and Mary Lowry

Chapter 1

INTRODUCTION

Emma Carolyn Kahle

1.1 Introduction

In this thesis I describe new methods for reconstructing past climate variability from ice-core records. I have developed these methods and present them here with water-isotope data from the South Pole ice core. In this chapter I provide background information on the use of water-isotope records in ice cores as well as the South Pole ice core project. I then describe the structure of this thesis and provide an overview of each of the following chapters. Chapters two and three are independent manuscripts, while chapter four is an application of this work for the purpose of this thesis. Lastly, I describe how each of these chapters comes together to create a coherent body of work, and I provide some recommendations for future work building on this thesis.

1.1.1 Water Isotopes in Ice Cores

The focus of this thesis is the interpretation of water stable-isotopes from ice-core records. Starting with the first studies of polar snow and ice cores, water-isotope ratios have long been integral to the analysis of climate variability (Langway, 1958; Gonfiantini and Picciotto, 1959; Dansgaard, 1964). Water isotopes in precipitation record the integrated experience of fractionation of water vapor as it moves through the atmosphere to higher latitudes (Dansgaard, 1954; Craig, 1961; Dansgaard, 1964). Ultimately, at middle and high latitudes, water isotopes in precipitation reflect the condensation temperature of the air (Merlivat and Jouzel, 1979; Jouzel and Merlivat, 1984). Because of this connection, there is a strong linear correlation between mean-annual site temperature and water-isotope ratios across polar ice sheets (Dansgaard, 1964; Lorius and Merlivat, 1977; Johnsen et al., 1989). Based on this relationship, variations in water isotopes measured in ice cores have been interpreted as a proxy for temperature variations back in time (Jouzel et al., 1982; Dansgaard et al., 1993; Jouzel et al., 2003; Masson-Delmotte et al., 2004).

The relative amount of heavy and light isotopologues in a water sample is reported in delta

notation, defined as the deviation in per mil (‰) from their relative abundance in a standard water. Traditionally for water isotopes, Vienna Standard Mean Ocean Water (VSMOW) is used as the standard. The delta notation is defined as:

$$\delta_{sample} = \left(\frac{R_{sample}}{R_{VSMOW}} - 1 \right) \times 1000,$$

where R is the ratio of heavy to light isotopologue. The two traditional water isotope ratios measured in ice cores, δ^{18}O and δD, reflect the ratios of $R = \frac{^{18}O}{^{16}O}$ and $R = \frac{^{2}H}{^{1}H}$, respectively. With recent improvements in measurement capabilities, δ^{17}O, reflecting $R = \frac{^{17}O}{^{16}O}$, can now be measured as well (Barkan and Luz, 2005; Landais et al., 2008; Schoenemann et al., 2011; Steig et al., 2014).

Although numerous studies have used water isotopes as a paleothermometer, this approach remains subject to some uncertainty because the isotope-temperature relationship is not necessarily constant through time (Jouzel et al., 1997). Many of the factors that influence this relationship, including the seasonality of snowfall and the rate-dependent fractionation of vapor in clouds, are poorly known and have likely changed in the past (Cuffey and Patterson, 2010). In locations where ice-core borehole thermometry is possible, the temperature profile of the ice sheet has been used to calibrate the isotope-temperature relationship back in time (Dahl-Jensen and Johnsen, 1986; Cuffey et al., 1994, 1995; Johnsen et al., 1995; Dahl-Jensen et al., 1998; Cuffey et al., 2016). At sites where abrupt temperature changes have occurred, measurements of gas stable-isotopes, such as δ^{15}N of N_2 trapped in air bubbles, can be used to estimate the magnitude of these temperature changes (Severinghaus et al., 1998; Lang et al., 1999; Severinghaus and Brook, 1999; Landais et al., 2004, 2006; Buizert et al., 2014). However, these methods are applicable only at certain ice-core sites, and additional approaches are required to constrain past temperature at other sites.

Water-isotope diffusion, a recent development in ice-core water-isotope analysis, provides a novel approach to constraining past temperature. After deposition, the inherently noisy iso-

tope signal in precipitation is altered by molecular vapor diffusion through interconnected air pathways in the firn layer (Langway, 1967; Johnsen, 1977; Whillans and Grootes, 1985; Cuffey and Steig, 1998). This process is temperature-dependent and damps the high-frequency power in the isotope signal, affecting its spectral characteristics (Johnsen et al., 1999, 2000). The extent of diffusion is quantified as the diffusion length. Below the firn, diffusion length continues to be affected by vertical strain due to ice flow (Gkinis et al., 2014). There is also continued diffusion within the solid ice, but this diffusion is orders of magnitude slower than firn diffusion and becomes important only towards the bottom of ice sheets where ice temperatures are higher and where older ice has had more time to diffuse.

Although the fundamental theory of water-isotope diffusion is well-established, only with recent ice-core measurement advances has water-isotope diffusion length been analyzed over the length of an entire core. With the development of continuous-flow analysis systems, entire ice cores can now be measured at very high resolution (Sigg et al., 1994; Huber and Leuenberger, 2005; Gkinis et al., 2010, 2011; Jones et al., 2017a). This high-resolution data enables spectral analysis of water-isotope diffusion for an entire ice core record (Simonsen et al., 2011; Gkinis et al., 2014; Jones et al., 2017b; Kahle et al., 2018). These new high-resolution data provide opportunities for many new types of water-isotope analysis, such as the work described in this thesis.

1.1.2 The South Pole Ice Core

The South Pole ice core (SPC14) was drilled and recovered over three field seasons between 2014 and 2016. I assisted in two of the field seasons as a core processor. The core reached a depth of 1751 m, corresponding to an age of approximately 54,000 years, surpassing the original goal of 1500 m and 40,000 years (Winski et al., 2019). SPC14 was the first core longer than 2000 m drilled south of 82°S, filling an important spatial gap in the collection of deep Antarctic ice cores. Further, SPC14 is located in a unique region of the East Antarctic plateau that is influenced by storm systems coming across West Antarctica. With a combination

of low mean-annual temperature (-49°C), relatively high accumulation rate (8 cm water-equivalent yr^{-1}), and low impurities in the ice, the site has ideal conditions for trace gas and chemistry analysis, the driving goal of the ice-core project. The relatively high accumulation rate also provides the highest temporal-resolution record from East Antarctica (Casey et al., 2014).

Due to its location on the flank of an ice divide, SPC14 lacks complete constraints on certain glaciological characteristics. While logistical support was readily available at the nearby South Pole station, the core was drilled at a non-ideal site about 200 km away from an ice divide. The modern surface ice velocity is 10 m yr^{-1}, meaning that ice at depth originated at the surface many kilometers upstream (Casey et al., 2014). When interpreting the climate record preserved in the ice, an advection correction must be made to account for differences in the modern ice-core site and the origin of the ice at the surface (Fudge et al., 2019; Lilien et al., 2018). The advection of ice also produces heating from horizontal strain, complicating any potential record of temperature from borehole thermometry. Furthermore, the advection creates some uncertainty in modeling the vertical strain experienced by the ice in the core, particularly at depth where influence from the bed topography is important. The methods that I apply in this thesis are well suited to the strengths (relatively high-accumulation) and weaknesses (complications with vertical-strain history and with borehole thermometry) of the SPC14 location.

The water-isotope measurements on SPC14 were completed at the INSTAAR lab at the University of Colorado, Boulder. A continuous flow analysis system connected to a Picarro L2130-i CRDS instrument was used to measure $\delta^{18}O$ and δD through the entire core at an effective resolution of 2 measurements per cm (Jones et al., 2017a). I participated in these measurements at CU, and we produced an extremely high-quality water-isotope record, refining the measurement system already developed for the WAIS Divide ice core. $\delta^{17}O$ was also measured continuously on a Picarro L2140-i instrument below a depth of 556 m and was validated with discrete measurements at IsoLab at the University of Washington (Steig

et al., in prep). I used these high-resolution measurements to estimate water-isotope diffusion length for all three water-isotope ratios through the entire core.

1.2 Structure of Thesis

In this thesis I investigate the climatic and glaciological information recorded in the South Pole ice core through the use of novel techniques. Building on previous work (Gkinis et al., 2014; Jones et al., 2017b), Chapter 2 describes an automated method for estimating the diffusion-length parameter from water-isotope data. While the foundation of this thesis is the water-isotope measurements, I also use information from the ice and gas timescales (Winski et al., 2019; Epifanio et al., in prep). Chapter 3 describes a method for combining these data sets in order to constrain climate variables (temperature and accumulation rate) as well as glaciologic variables (vertical strain) from the ice-core record. Though these methods are demonstrated on SPC14, a similar approach could be applied to other ice cores with similar measurements. As an application of my results, Chapter 4 uses a climate model to investigate the implications of my climate reconstructions within the broader context of atmospheric dynamics.

1.2.1 Overview Chapter 2

This chapter establishes the methodology that I use in analyzing the SPC14 water-isotope record. Previous studies use other effective approaches, but lack the combination of efficiency, objectivity, and flexibility (Gkinis et al., 2014; Jones et al., 2017b). Given recent improvements in techniques to measure water-isotopes at extremely high resolution (Jones et al., 2017a), a new approach was needed to estimate diffusion lengths regardless of how the water-isotope data were measured. In this chapter, I develop an automated method for estimating diffusion length efficiently and effectively from any water-isotope data set. The method isolates the effects of smoothing by lab measurements from the smoothing that

occurred in the ice sheet.

First, I demonstrate the need for such a method by considering water-isotope data sets measured by different techniques from both Greenland and Antarctic ice cores. The spectral characteristics of these different data sets vary due to different measurement techniques. I propose several candidate models to describe the noise generated from measurements. These models isolate the natural diffusion signal and estimate the diffusion length realized in the ice sheet. To evaluate the proposed models, I compare their resulting diffusion-length estimates against one another, against the results of a manual method in Jones et al. (2017b), and against synthetic data with known diffusion-length.

Ultimately, I recommend a three-function model for estimating diffusion length. The automation of this approach yields high-resolution diffusion-length records. A high-resolution record is necessary for recovering relatively small-scale features in the record, which is important for comparison with other firn-related ice-core data sets, such as the total air content. Such comparisons improve understanding of firn processes at a particular ice-core site. More broadly, high-resolution diffusion-length records can be compared with the output of synthetic diffusion-length records from firn models to improve our general understanding of firn processes.

1.2.2 Overview Chapter 3

In this chapter I use the SPC14 diffusion-length record, estimated with the approach in Chapter 2, to reconstruct past climatic and glaciologic conditions at the South Pole site. To constrain past temperature and accumulation rate, I combine the diffusion-length record with the Δage, another data set related to firn processes (Epifanio et al., in prep). Because the diffusion length also depends on the vertical strain in the ice sheet, I use the annual-layer thickness data to provide sufficient constraints on the ice thinning function (Winski et al., 2019). This combination of data sets provides three known variables to solve completely for

three unknown variables through the length of the record.

I use a statistical inverse approach to combine these data sets using a simple forward model (e.g. Mosegaard and Sambridge (2002); Steen-Larsen et al. (2010)). The forward model consists of a firn-densification model, an isotope-diffusion model, and the simple relationship between accumulation rate, annual-layer thickness, and thinning function. I use this forward model in a Monte-Carlo approach, evaluating the results of many possible model inputs, to determine a set of solutions for the input parameters that best match the data sets. The result is an ensemble of reconstructions for temperature, accumulation rate, and ice thinning for SPC14. I discuss the sensitivity of these results to the method itself as well as to each of the data sets included in the optimization.

The mean and standard deviation of the reconstruction ensemble provide comparisons against naive expectations about each of these data sets. Comparison of the temperature reconstruction against the water-isotope record provides an independent scaling of the isotope-temperature relationship through time. Contrary to previous work suggesting that the relationship should be fairly constant in central Antarctica (Jouzel et al., 2003), my results suggest that the relationship may vary significantly between glacial and interglacial conditions, at least at a site such as the South Pole. Furthermore, the glacial-interglacial temperature change, a key target of paleoclimate sensitivity studies (Genthon et al., 1987; Lorius et al., 1990), is approximately 6°C. This change is less than previous estimates from East Antarctic ice cores in the range of 8-11°C (Parrenin et al., 2013), which rely on linear scaling of water isotopes without a direct, independent temperature calibration. A change of 6°C is more in line with results from modern general circulation models (GCMs), which estimate a change of about 5-8.5°C (Crowley and North, 1981; Masson-Delmotte et al., 2006).

The thinning-function reconstruction suggests that the output of a 1-dimensional ice flow model overestimates the vertical strain at the bottom of the core. This overestimation is likely due to insufficient constraints on the bedrock topography upstream along the flowline reaching the core site. A two-dimensional ice flow model suggests that details in upstream

bedrock topography can account for the discrepancy between the simple model output and my reconstruction. The thinning function affects the reconstruction of the accumulation rate, which is important as an input for firn-densification models and as a climate variable in its own right. Together, this set of results provides an important interpretation of the SPC14 record.

1.2.3 Overview Chapter 4

This chapter uses a climate model to examine the physical mechanisms underlying glacial-interglacial climate changes. This work is motivated by the agreement between estimates of glacial-interglacial temperature change from GCM results and from the temperature construction from Chapter 3. I use a climate model as a tool to analyze the factors within the climate system that determine the temperature response to a glacial-interglacial-like change.

An aquaplanet GCM provides a mid-complexity model to simulate changes in highly idealized topography and atmospheric CO_2 levels within a comprehensive scheme of atmospheric physics. I simulate the responses of three different Antarctic topography configurations to glacial-interglacial CO_2 changes of 180ppm to 280ppm. I examine the response of the model results in temperature, energy balance, cloud cover, and winds. The responses of these variables agree well with previous work examining Antarctic topography change in GCMs. The response to combined changes in topography and CO_2 indicates that lower elevation enhances polar amplification of surface warming due to a fundamental gradient in the stability of air with height even without the presence of a surface temperature inversion.

This result that topography impacts polar amplification is important for understanding past Antarctic temperature changes and for comparison between model results and data reconstructions. The gradient in the stability of air with height provides a basic explanation for why Antarctic polar amplification is damped compared to the Arctic, where the mean topography is lower. Other factors related to albedo and atmospheric circulation that differentiate

the Antarctic from the Arctic may be important as well, but the stability of the atmosphere provides a simple basis for explaining the difference in polar amplification between hemispheres. This result is also important for interpreting ice-core data from sites at different elevations.

1.2.4 Overview Appendix A

Although the theory behind water-isotope diffusion has long been established (Johnsen, 1977), a comprehensive description of all the math involved is absent from the literature. In Appendix A, I compile detailed derivations related to firn diffusion to supplement the existing literature. I combine the fundamental physics of the advection-diffusion equation with various approaches taken by previous papers, textbooks, and online resources. This collection describes multiple approaches to the same problems, which leads to a deeper understanding of the underlying physical processes through multiple perspectives. The work presented in this section is not novel, but is an important synthesis of these derivations all in one place.

I provide derivations for three different equations related to water-isotope diffusion. First, I present two different approaches to deriving an expression for the diffusivity of water molecules within the firn (Johnsen, 1977; Whillans and Grootes, 1985). I compare the final formulations of each approach, and, despite their differences, I show that they are equivalent. Second, I compare an analytical and a statistical approach to solving the advection-diffusion equation in the context of firn diffusion (Strang, 2006; Lasaga, 2014). Again, though the methods are different they arrive at the same solution. Finally, I describe a statistical derivation for the diffusion length, which provides intuitive insight into the meaning of the parameter (Lasaga, 2014). For each of these derivations, I expand on the details provided in the original, clarifying all necessary steps and assumptions.

1.3 Synthesis

The work developed in this thesis presents an integrated approach to combine multiple data sets and models to constrain information from an ice-core record. Like other types of proxy records in the earth system, ice cores preserve useful information about the past. However, interpretation of that information requires understanding the proxy systems and constraining the environmental influences on those systems to extract the desired information (Evans et al., 2013). The challenge in this interpretation is in how to most effectively combine measured information with modeled information to tease apart the original environmental influences. I use the South Pole ice core to show how our understanding of the ice-core proxy system can be applied to measured data sets to extract information about the past.

To constrain information from an ice core, the first step is to maximize the information obtained from available measurements. Water-isotope records from ice cores have long been used for their correlation with temperature, but additional information exists within the spectral content of those records. Expanding on previous work that established the theory and analysis of water-isotope diffusion records (Johnsen et al., 2000; Gkinis et al., 2014; Jones et al., 2017b), the Appendix provides full details of the physical theory, and Chapter 2 shows how the spectral information from environmental influences can be separated from that originating from lab measurements. The diffusion length is a unique parameter in ice-core analysis because it connects processes that occur in the firn to processes that occur in the rest of the ice sheet. In addition to the diffusion-length record, other work on SPC14 (e.g. Winski et al. (2019); Epifanio et al. (in prep); Fudge et al. (2019)) also provides important information needed to fully constrain the proxy record.

Armed with as much information as possible about the ice-core proxy system, the next step is to use models to combine the different sources of information. Models of firn processes and ice-sheet dynamics connect our understanding of past environmental processes with the data sets measured in the core. Individually, no measurement can fully constrain all processes

described in the models, but multiple measurements together provide sufficient information. Chapter 3 shows how multiple data sets can be combined with simple models to solve for past environmental processes. This inverse approach is common in geophysical problems where we want to know the initial conditions that led to the measurable results (Mosegaard and Tarantola, 2002). The inverse approach described here shares some strategy with previous ice-core work analyzing borehole thermometry and diffusion of gases in the firn (e.g. Cuffey et al. (2016); Landais et al. (2006)). However, this approach combines a novel collection of data sets that bridges the gap between firn and solid-ice processes to create a self-consistent reconstruction of climate and glaciologic variables.

The final step in interpreting the ice-core record involves relating the climate reconstruction to GCM experiments in order to understand the broader dynamical implications of the reconstructions. Zooming out from the relatively small-scale processes that influence the firn and ice dynamics at a particular ice-core site, the temperature reconstruction itself provides a useful constraint on the larger-scale climate dynamics. Many studies have applied such a strategy in order to interpret the climate-dynamics implications of ice-core data (Masson-Delmotte et al., 2006; Bradley et al., 2013; Otto-Bliesner et al., 2013; Steig et al., 2015). Chapter 4 describes an analysis of glacial-interglacial changes in a climate model as a way to further interpret the climate implications from the SPC14 reconstruction.

1.4 Recommendations for Future Work

The work presented here provides a foundation to interpreting the information contained within the South Pole ice core and establishes new methods for analyzing ice-core data. To improve analysis of high-resolution diffusion-length records, more work is necessary to further understand the detailed physics that drive water-isotope diffusion in the firn. For South Pole and other ice-core sites, comparison of diffusion-length records with other firn-related data sets, such as total air content, can improve understanding of how firn-densification processes change through time. Detailed firn-densification models can provide important comparisons

by producing synthetic diffusion-length records derived under particular climate conditions. Models that detail firn microphysics (Horlings, 2019) as well as model frameworks that combine multiple firn-densification models (Stevens et al., 2020; Gkinis et al., 2019) are important tools in this work.

This thesis focuses on the South Pole ice-core record, but in the future, the inverse approach in Chapter 3 can be modified to constrain reconstructions using data sets from new or previously-drilled ice-core records. Due to differences such as mean-annual temperature, accumulation rate, and specifics of ice dynamics, different ice-core sites may differ in which pieces of information are well-constrained. While SPC14 has high-quality diffusion-length and timescale data sets, other sites may have useful borehole thermometry or well-constrained models of vertical strain. An inverse approach using diffusion length to combine information from firn and ice-sheet processes could be modified to take advantage of different well-constrained information at a particular site.

Further work with climate models can improve the interpretation of climate dynamics from the SPC14. The work in this thesis focuses on highly idealized glacial-interglacial changes in an aquaplanet GCM. These results highlight that even in the absence of a surface temperature inversion, the stability of the atmosphere decreases with height and thus damps polar amplification of warming. Future model experiments are needed to evaluate the impact of the absence of a surface inversion on the stability of the atmosphere at different heights. Experiments with and without surface inversions can help determine the relative importance of an inversion in contributing to damping polar amplification over Antarctic topography.

BIBLIOGRAPHY

Barkan, E., and Luz, B. (2005). High precision measurements of 17O/16O and 18O/16O ratios in H2O. *Rapid Communications in Mass Spectrometry*, 19(24), 3737-3742.

Bradley, S. L., M. Siddall, G. A. Milne, V. Masson-Delmotte, and E. Wolff (2013), Combining ice core records and ice sheet models to explore the evolution of the East Antarctic Ice Sheet during the last interglacial period, *Global Planet. Change*, 100, 278290.

Buizert, C., Gkinis, V., Severinghaus, J. P., He, F., Lecavalier, B. S., Kindler, P., Brook, E. J., et al. (2014). Greenland temperature response to climate forcing during the last deglaciation. *Science*, 345(6201), 1177-1180.

Casey, K. A., Fudge, T. J., Neumann, T. A., Steig, E. J., Cavitte, M. G. P., and Blankenship, D. D. (2014). The 1500 m South Pole ice core: Recovering a 40 ka environmental record. *Annals of Glaciology*, 55(68), 137–146.

Craig, H. (1961). Isotopic variations in meteoric waters. *Science*, 133(3465), 1702-1703.

Crowley, T. J., and G. R. North (1981). *Paleoclimatology*. New York, NY: Oxford University Press.

Cuffey, K. M., Alley, R. B., Grootes, P. M., Bolzan, J. M., and Anandakrishnan, S. (1994). Calibration of the 18 O isotopic paleothermometer for central Greenland, using borehole temperatures. *Journal of Glaciology*, 40(135), 341-349.

Cuffey, K. M., Clow, G. D., Alley, R. B., Stuiver, M., Waddington, E. D., and Saltus, R. W. (1995). Large arctic temperature change at the Wisconsin-Holocene glacial transition. *Science*, 270(5235), 455-458.

Cuffey, K. M. and Steig, E. J. (1998). Isotopic diffusion in polar firn: Implications for interpretation of seasonal climate parameters in ice-core records, with emphasis on central Greenland. *Journal of Glaciology*, 44(147), 273–284.

Cuffey, K., and Patterson, W. (2010). The Physics of Glaciers. *Elsevier*. Burlington, MA.

Cuffey, K. M., Clow, G. D., Steig, E. J., Buizert, C., Fudge, T. J., Koutnik, M., Severinghaus, J. P. et al. (2016). Deglacial temperature history of West Antarctica. *Proceedings of the National Academy of Sciences*, 113(50), 14249-14254.

Dahl-Jensen, D., and Johnsen, S. J. (1986). Palaeotemperatures still exist in the Greenland ice sheet. *Nature*, 320(6059), 250.

Dahl-Jensen, D., Mosegaard, K., Gundestrup, N., Clow, G. D., Johnsen, S. J., Hansen, A. W., and Balling, N. (1998). Past temperatures directly from the Greenland ice sheet. *Science*, 282(5387), 268-271.

Dansgaard, W. (1954). The ^{18}O-abundance in fresh water. *Geochimica et Cosmochimica Acta*, 6(5-6), 241–260.

Dansgaard, W. (1964). Stable isotopes in precipitation. *Tellus B*, 16(4), 436–468.

Dansgaard, W., Johnsen, S. J., Clausen, H. B., Dahl-Jensen, D., Gundestrup, N. S., Hammer, C. U., Bond, G., et al. (1993). Evidence for general instability of past climate from a 250-kyr ice-core record. *Nature*, 364(6434), 218.

Epifanio et al. in prep. The SP19 chronology for the South Pole Ice Core Part 2: Gas age scale, Delta-age, and smoothing of atmospheric records. Unpublished manuscript.

Evans, M. N., Tolwinski-Ward, S. E., Thompson, D. M., and Anchukaitis, K. J. (2013). Applications of proxy system modeling in high resolution paleoclimatology. *Quaternary Science Reviews*, 76, 16-28.

Fudge, T.J., D.A. Lilien, M. Koutnik, H. Conway, C.M. Stevens, E.D. Waddington, E.J. Steig, and A.J. Schauer (2019). Advection (non-climate) impact on the South Pole Ice Core. *Climate of the Past Discussions* doi:10.5194/cp-2019-66.

Gkinis, V., Popp, T. J., Johnsen, S. J., and Blunier, T. (2010). A continuous stream flash evaporator for the calibration of an IR cavity ring-down spectrometer for the isotopic analysis of water. *Isotopes in environmental and health studies*, 46(4), 463-475.

Gkinis, V., Popp, T. J., Blunier, T., Bigler, M., Schpbach, S., Kettner, E., and Johnsen, S. J. (2011). Water isotopic ratios from a continuously melted ice core sample. *Atmospheric Measurement Techniques* 4, 25312542.

Gkinis, V., Simonsen, S. B., Buchardt, S. L., White, J. W. C. and Vinther, B. M. (2014). Water isotope diffusion rates from the NorthGRIP ice core for the last 16,000 years - glaciological and paleoclimatic implications. *Earth and Planetary Science Letters*, 405, 132–141.

Gkinis, V., Holme, C., Kahle, E.C., Stevens, C.M., Steig, E.J., and Vinther, B.M. (2019). Numerical experiments on firn isotope diffusion using the Community Firn Model. Manuscript submitted for publication.

Gonfiantini, R., and Picciotto, E. (1959). Oxygen isotope variations in Antarctic snow samples. *Nature*, 184(4698), 1557-1558.

Horlings, B.I. (2019). Modeling firn densification through viscosity and microstructures (Master's thesis). University of Washington, Seattle, USA.

Huber, C., and Leuenberger, M. (2005). On-line systems for continuous water and gas isotope ratio measurements. *Isotopes in environmental and health studies*, 41(3), 189-205.

Johnsen, S. J. (1977). Stable isotope homogenization of polar firn and ice. *Isotopes and Impurities in Snow and Ice*, 201–219.

Johnsen, S. J., Dansgaard, W., and White, J. W. C. (1989). The origin of Arctic precipitation under present and glacial conditions. *Tellus B: Chemical and Physical Meteorology*, 41(4), 452-468.

Johnsen, S. J., Dahl-Jensen, D., Dansgaard, W., and Gundestrup, N. (1995). Greenland palaeotemperatures derived from GRIP bore hole temperature and ice core isotope profiles. *Tellus B: Chemical and Physical Meteorology*, 47(5), 624-629.

Johnsen, S. J., Clausen, H. B., Jouzel, J., Schwander, J., Sveinbjornsdottir, A. E., and White, J. (1999). Stable isotope records from Greenland deep ice cores: the climate signal and the role of diffusion. *Ice Physics and the Natural Environment*, 89-107.

Johnsen, S. J., Clausen, H. B., Cuffey, K. M., Hoffmann, G., Schwander, J. and Creyts, T. (2000). Diffusion of stable isotopes in polar firn and ice: The isotope effect in firn diffusion. *Physics of Ice Core Records*, 121–140.

Jones, T. R., Cuffey, K. M., White, J. W. C., Steig, E. J., Buizert, C., Markle, B. R., McConnell, J. R. and Sigl, M. (2017a). Water isotope diffusion in the WAIS Divide ice core during the Holocene and last glacial. *Journal of Geophysical Research: Earth Surface*, 122, 290-309.

Jones, T. R., White, J. W. C., Steig, E. J., Vaughn, B. H., Morris, V., Gkinis, V., Markle, B. R. and Schoenemann, S. W. (2017b). Improved methodologies for continuous flow analysis of stable water isotopes in ice cores. *Atmospheric Measurement Techniques*, 10, 617-632.

Jouzel, J., Merlivat, L., and Lorius, C. (1982). Deuterium excess in an East Antarctic ice core suggests higher relative humidity at the oceanic surface during the last glacial maximum. *Nature*, 299(5885), 688.

Jouzel, J., and Merlivat, L. (1984). Deuterium and oxygen 18 in precipitation: Modeling of

the isotopic effects during snow formation. *Journal of Geophysical Research: Atmospheres*, 89(D7), 11749-11757.

Jouzel, J., Alley, R. B., Cuffey, K. M., Dansgaard, W., Grootes, P., Hoffmann, G., Stievenard, M. et al. (1997). Validity of the temperature reconstruction from water isotopes in ice cores. *Journal of Geophysical Research: Oceans*, 102(C12), 26471-26487.

Jouzel, J., Vimeux, F., Caillon, N., Delaygue, G., Hoffmann, G., MassonDelmotte, V., and Parrenin, F. (2003). Magnitude of isotope/temperature scaling for interpretation of central Antarctic ice cores. *Journal of Geophysical Research: Atmospheres*, 108(D12).

Kahle, E. C., Holme, C., Jones, T. R., Gkinis, V., and Steig, E. J. (2018). A Generalized Approach to Estimating Diffusion Length of Stable Water Isotopes From IceCore Data. *Journal of Geophysical Research: Earth Surface*, 123(10), 2377-2391.

Landais, A., Caillon, N., Goujon, C., Grachev, A. M., Barnola, J. M., Chappellaz, J., Leuenberger, M. et al. (2004). Quantification of rapid temperature change during DO event 12 and phasing with methane inferred from air isotopic measurements. *Earth and Planetary Science Letters*, 225(1-2), 221-232.

Landais, A., Masson-Delmotte, V., Jouzel, J., Raynaud, D., Johnsen, S., Huber, C., Minster, B. et al. (2006). The glacial inception as recorded in the NorthGRIP Greenland ice core: timing, structure and associated abrupt temperature changes. *Climate Dynamics*, 26(2-3), 273-284.

Landais, A., Barkan, E., and Luz, B. (2008). Record of δ18O and 17Oexcess in ice from Vostok Antarctica during the last 150,000 years. *Geophysical Research Letters*, 35(2).

Lang, C., Leuenberger, M., Schwander, J., and Johnsen, S. (1999). 16 C rapid temperature variation in central Greenland 70,000 years ago. *Science*, 286(5441), 934-937.

Langway, C. C. (1958). A 400 Meter Deep Ice Core in Greenland: Preliminary Report. *Journal of Glaciology*, 3(23), 217-217.

Langway, C. C. (1967). Stratigraphic analysis of a deep ice core from Greenland. US Cold Regions Research and Engineering Laboratory. Research Report, 77.

Lilien, D. A., Fudge, T. J., Koutnik, M. R., Conway, H., Osterberg, E. C., Ferris, D. G., and Stevens, C. M. et al. (2018). Holocene IceFlow Speedup in the Vicinity of the South Pole. *Geophysical Research Letters*, 45(13), 6557-6565.

Lorius, C., and Merlivat, L. (1977). Distribution of mean surface stable isotope values in East Antarctica, Isotopes and Impurities in Snow and Ice. *IAHS*, 118, 127-137.

Lorius, C., Jouzel, J., Raynaud, D., Hansen, J., and Le Treut, H. (1990). The ice-core record: climate sensitivity and future greenhouse warming. *Nature*, 347(6289), 139.

Masson-Delmotte, V., Stenni, B., and Jouzel, J. (2004). Common millennial-scale variability of Antarctic and Southern Ocean temperatures during the past 5000 years reconstructed from the EPICA Dome C ice core. *The Holocene*, 14(2), 145-151.

Masson-Delmotte, V., Kageyama, M., Braconnot, P., Charbit, S., Krinner, G., Ritz, C., and Gladstone, R. M. et al. (2006). Past and future polar amplification of climate change: climate model intercomparisons and ice-core constraints. *Climate Dynamics*, 26(5), 513-529.

Merlivat, L., and Jouzel, J. (1979). Global climatic interpretation of the deuteriumoxygen 18 relationship for precipitation. *Journal of Geophysical Research: Oceans*, 84(C8), 5029-5033.

Mosegaard, K., and Tarantola, A. (2002). Probabilistic approach to inverse problems. *International Geophysics Series*, 81(A), 237-268.

Mosegaard, K., and Sambridge, M. (2002). Monte Carlo analysis of inverse problems. *Inverse problems*, 18(3), R29.

Otto-Bliesner, B. L., N. Rosenbloom, E. J. Stone, N. P. McKay, D. J. Lunt, E. C. Brady, and J. T. Overpeck (2013), How warm was the last interglacial? New modeldata comparisons, *Philos. Trans. R. Soc. London*, Ser. A, 371, 120.

Parrenin, F., Masson-Delmotte, V., Kohler, P., Raynaud, D., Paillard, D., Schwander, J., Jouzel, J. et al. (2013). Synchronous change of atmospheric CO2 and Antarctic temperature during the last deglacial warming. *Science*, 339(6123), 1060-1063.

Schoenemann, S. W., Schauer, A. J., and Steig, E. J. (2013). Measurement of SLAP2 and GISP 17O and proposed VSMOWSLAP normalization for 17O and 17Oexcess. *Rapid Communications in Mass Spectrometry*, 27(5), 582-590.

Severinghaus, J. P., Sowers, T., Brook, E. J., Alley, R. B., and Bender, M. L. (1998). Timing of abrupt climate change at the end of the Younger Dryas interval from thermally fractionated gases in polar ice. *Nature*, 391(6663), 141.

Severinghaus, J. P., and Brook, E. J. (1999). Abrupt climate change at the end of the last glacial period inferred from trapped air in polar ice. *Science*, 286(5441), 930-934.

Sigg, A., Fuhrer, K., Anklin, M., Staffelbach, T., and Zurmuehle, D. (1994). A continuous analysis technique for trace species in ice cores. *Environmental Science and Technology*, 28(2), 204209.

Simonsen, S. B., Johnsen, S. J., Popp, T. J., Vinther, B. M., Gkinis, V., and Steen-Larsen, H. C. (2011). Past surface temperatures at the NorthGRIP drill site from the difference in firn diffusion of water isotopes. *Climate of the Past*, 7(4), 1327-1335.

Steen-Larsen, H. C., Waddington, E. D., and Koutnik, M. R. (2010). Formulating an inverse problem to infer the accumulation-rate pattern from deep internal layering in an ice sheet using a Monte Carlo approach. *Journal of Glaciology*, 56(196), 318-332.

Steig, E. J., Gkinis, V., Schauer, A. J., Schoenemann, S. W., Samek, K., Hoffnagle, J., Tan, S. M. et al. (2014). Calibrated high-precision 17O-excess measurements using cavity

ring-down spectroscopy with laser-current-tuned cavity resonance. *Atmos. Meas. Tech.*, 7, 2421-2435.

Steig, E. J., Huybers, K., Singh, H. A., Steiger, N. J., Ding, Q., Frierson, D. M., White, J. W. et al. (2015). Influence of West Antarctic ice sheet collapse on Antarctic surface climate. *Geophysical Research Letters*, 42(12), 4862-4868.

Steig, E.J., Kahle, E.C., Schauer, A.J., Jones, T.R., Morris, V.M., Vaughn, B.H., White, and J.W.C. Continuous-flow analyses of the complete water isotope composition of ice cores. *Rapid Communications in Mass Spectrometry*, Unpublished manuscript.

Stevens, C. M., Verjans, V., Lundin, J. M. D., Kahle, E. C., Horlings, A. N., Horlings, B. I., and Waddington, E. D.: The Community Firn Model (CFM) v1.0, Geosci. Model Dev. Discuss., https://doi.org/10.5194/gmd-2019-361, in review, 2020.

Whillans, I. M., and Grootes P. M. (1985). Isotopic diffusion in cold snow and firn. *Journal of Geophysical Research*, 90(D2), 3910–3918.

Winski, D. A., Fudge, T. J., Ferris, D. G., Osterberg, E. C., Fegyveresi, J. M., Cole-Dai, J., Buizert, C. et al. (2019). The SP19 chronology for the South Pole Ice CorePart 1: volcanic matching and annual layer counting. *Climate of the Past*, 15(5), 1793-1808.

Chapter 2

A GENERALIZED APPROACH TO ESTIMATING DIFFUSION LENGTH OF STABLE WATER ISOTOPES FROM ICE-CORE DATA

Emma C. Kahle, Christian Holme, Tyler R. Jones, Vasileios Gkinis,
and Eric J. Steig

Original Citation: Kahle, E. C., Holme, C., Jones, T. R., Gkinis, V., and Steig, E. J. (2018). A Generalized Approach to Estimating Diffusion Length of Stable Water Isotopes From Ice-Core Data. *Journal of Geophysical Research: Earth Surface*, 123(10), 2377-2391.

Diffusion of water vapor in the porous firn-layer of ice sheets damps high-frequency variations in water-isotope profiles. Through spectral analysis, the amount of diffusion can be quantified as the "diffusion length," the mean cumulative diffusive-displacement of water molecules relative to their original location at time of deposition. In this study, we use two types of ice-core data, obtained from either continuous-flow analysis or discrete sampling, to separate diffusional effects occurring in the ice sheet from those arising through analytical processes in the laboratory. In both Greenlandic and Antarctic ice cores, some characteristics of the power spectral density of a dataset depend on the water-isotope measurement process. Due to these spectral characteristics, currently established approaches for diffusion estimation do not work equally well for newer, continuously-measured datasets with lower instrument noise levels. We show how smoothing within the continuous-flow analysis system can explain these spectral differences. We propose two new diffusion-estimation techniques, which can be

applied to either continuously- or discretely-measured datasets. We evaluate these techniques and demonstrate their viability for future use. The results of this study have the potential to improve climate interpretation of ice-core records as well as models of firn densification and diffusion.

2.1 Introduction

Water-isotope data have long been used as a climate proxy, based on the temperature-dependent distillation of water isotopes in the atmosphere (Epstein et al., 1951; Dansgaard, 1954, 1964). Post-depositional processes occurring in an ice sheet alter the original climate signal recorded in the water-isotope ratios. The most dominant alteration to the signal occurs due to diffusion in the firn column, snowfall in the upper tens of meters of an ice sheet that has yet to be fully compressed into ice. Because firn is permeable, water molecules diffuse in the vapor phase along gradients of concentration and temperature (Johnsen, 1977; Whillans and Grootes, 1985). In ice-core research, using water-isotope data to analyze the diffusion process yields information about past firn conditions, including surface temperature, as well as ice-sheet thinning history (Gkinis et al., 2014). Further, if high-frequency climate information, as existed at the ice sheet surface, is to be reconstructed from water-isotope data, a diffusion correction must be applied (Jones et al., 2018).

The diffusion process damps the high-frequency climate variations recorded in a water-isotope profile. The amount of diffusion can be characterized as the "diffusion length," which represents the mean cumulative diffusive-displacement in the vertical direction of water molecules relative to their original location in the firn at the time of deposition. Through spectral analysis, the diffusion length can be estimated for a section of data based on the damping of its high frequencies. Estimates of diffusion length have been made for many ice cores in both Greenland and Antarctica (Simonsen et al., 2011; Gkinis et al., 2014; van der Wel et al., 2015; Jones et al., 2017a; Holme et al., 2018), typically yielding diffusion lengths on the order of $\sim$5 to 10 cm at the base of the firn column.

Existing methods for estimating diffusion length do not work equally well for all datasets. In particular, new data obtained using continuous-flow analysis systems with high-precision laser spectrometers have somewhat different spectral characteristics than those obtained by older measurement methods (Jones et al., 2017a). These differences affect the estimation

of diffusion lengths, and therefore can also affect climate reconstructions. In this paper, we discuss the spectral structure of continuously-measured data, including possible sources of additional noise that are not present in discretely-measured data and perhaps not perceptible in continuously-measured data with lower instrument precision. We then describe two new approaches for determining diffusion length that can be applied to any high-resolution water-isotope dataset. We use new and previously-published data from ice cores in Greenland and Antarctica to demonstrate the effectiveness of these approaches, and we discuss the broader implications of these improved methods.

2.2 Isotope Diffusion Theory

Water-isotope vapor diffusion occurs in the firn column, where interconnected air pathways allow water vapor to diffuse. At the base of the firn column, firn densification ultimately traps individual air bubbles in solid ice (i.e. the bubble close-off depth), causing vapor diffusion to cease. Solid-phase diffusion continues below the firn layer but is orders of magnitude slower than vapor diffusion in the firn. Vertical strain (compaction of the firn layer and ice thinning by extensional flow) acts to progressively reduce the diffusion length. The accumulated solid-ice diffusion begins to compete with the vertical strain only at depth within the ice sheet where the ice is warmer due to geothermal heating. For ice-core sites like NEEM and WAIS Divide, solid ice diffusion is not detected until ages greater than 50ka (Gkinis et al., 2014).

The effects of diffusion, firn compaction, and ice thinning on the isotope profile can be described by Fick's second law:

$$\frac{\partial \delta}{\partial t} = D\frac{\partial^2 \delta}{\partial z^2} - \dot{\epsilon} z \frac{\partial \delta}{\partial z}, \tag{2.1}$$

where δ is the isotope ratio, D is the diffusivity coefficient, z is the vertical coordinate assuming an origin fixed on a sinking layer of firn, and $\dot{\epsilon}$ is the vertical strain rate (Johnsen, 1977; Whillans and Grootes, 1985). The term $\dot{\epsilon} z$ can be thought of as the vertical velocity.

The diffusion length σ can be calculated from the diffusivity D and the vertical strain rate $\dot{\epsilon}$ by:

$$\frac{d\sigma^2}{dt} - 2\dot{\epsilon}(t)\sigma^2 = 2D(t). \tag{2.2}$$

Note that the diusivity $D(t)$ at a given depth in the firn is less than the diffusivity of water vapor in air and the instantaneous value of $D(t)$ is given as follows (following Johnsen et al. (2000)):

$$D = \frac{m\,p\,D_a}{R\,T\,\alpha\,\tau}\left(\frac{1}{\rho} - \frac{1}{\rho_{ice}}\right) \tag{2.3}$$

where m is the molar weight of water, p is the saturation pressure over ice at absolute temperature T, D_a is the diffusivity in air, R is the gas constant, α is the fractionation factor, τ is the tortuosity factor of the firn, ρ is density of the firn, and ρ_{ice} is the density of ice. The diffusivity is different for δ^{18}O and δD because D_a and α are different for each isotope ratio.

As shown by Johnsen (1977), and subsequently used in many studies (Whillans and Grootes, 1985; Cuffey and Steig, 1998; Johnsen et al., 2000; Simonsen et al., 2011; Gkinis et al., 2014; van der Wel et al., 2015; Jones et al., 2017a; Holme et al., 2018), the solution to Equation 2.1 has the same form as the well-known solution to the heat equation. This solution for the isotope profile at time t and depth z is given by:

$$\delta(z,t) = S(t)\frac{1}{\sigma\sqrt{2\pi}}\int_{-\infty}^{\infty}\delta(z,0)\exp\left(\frac{-(z-u)^2}{2\sigma^2}\right)du, \tag{2.4}$$

A complete derivation of this solution is available in textbooks (e.g. Lasaga (2014)). The factor $S(t)$ is the total thinning a layer has experienced due to ice flow from $t = 0$ to $t = t'$:

$$S(t') = \exp\left(\int_0^{t'}\dot{\epsilon}(t)dt\right), \tag{2.5}$$

Equation 2.4 is equivalent to the convolution of the initial isotope profile, $\delta(z, 0)$, with a Gaussian filter of standard deviation equal to the diffusion length σ (Johnsen et al., 2000):

$$\mathcal{G} = \frac{1}{\sigma\sqrt{2\pi}} \exp\left(\frac{-z^2}{2\sigma^2}\right). \tag{2.6}$$

2.3 Water-Isotope Data

Traditionally, water-isotope data are measured discretely by cutting small sections of the core ($\sim$1 to 50 cm) to produce a sample. The isotope ratio of each discrete sample is determined by mass spectrometry (Johnsen et al., 1972; Brand et al., 2009; Schoenemann et al., 2011) or with newer laser spectroscopy instruments (Kerstel et al., 1999; Lis et al., 2008; Gupta et al., 2009). In the past decade, it has also become common for ice-core water-isotope measurements to be made using continuous-flow analysis (CFA) systems. CFA systems allow for continuous injection of a stream of water-vapor sample from a continuously melted ice stick into the cavity of a laser spectrometer, yielding data of high resolution and precision (Gkinis et al., 2011a; Emanuelsson et al., 2015; Jones et al., 2017b). A typical nominal resolution for CFA datasets is 0.5 cm.

Various CFA systems exist; in this work we consider datasets measured with two different CFA systems (Gkinis et al., 2010, 2011a; Jones et al., 2017b). We use previously-published data from the WAIS Divide ice core (WDC) (Jones et al., 2017a) and sections of data from a new ice core at the South Pole (SPC), both measured with the CFA system at the Institute of Arctic and Alpine Research (INSTAAR) at the University of Colorado. Details of the SPC ice-core project are given in Casey et al. (2014). A Picarro L2130-i laser spectrometer was used for δ^{18}O and δD measurements; details are given in Jones et al. (2017b). We use the first 2800 m of WDC, corresponding to approximately the last 30,000 years. We use two sections of SPC, one from the Holocene and one from the last glacial period. For comparison, we use data from NEEM and Dome F (Gkinis et al., 2011a; Svensson et al., 2015) measured on a second CFA system at the University of Copenhagen. We also use discrete datasets from

Table 2.1: Summary of the datasets used in this paper and plotted in Figure 2.2. *Second section of SPC is plotted in Figure 2.4.

Core	Analysis Method	Depths (m)	Resolution (m)
Dome C	discrete	308-318	0.025
NEEM	discrete	174-194	0.025
EDML	discrete	123-173	0.05
WDC	discrete	260-290	0.05
GRIP	discrete	753-776	0.025
NGRIP	discrete	1300-1320	0.05
Dome F	continuous	302-307	0.005
NEEM	continuous	1382-1399	0.005
SPC	continuous	450-500	0.005
SPC	continuous	1060-1075*	0.005
WDC	continuous	450-500	0.005

Greenlandic and Antarctic ice cores, including GRIP, EDML, NEEM, WDC, NGRIP, and Dome C (Oerter et al., 2004; Gkinis et al., 2011a; Gkinis, 2011b; Steig et al., 2013; Gkinis et al., 2014; Holme et al., 2018). These datasets are summarized in Table 2.1.

2.4 Estimating Diffusion Length from Ice-Core Data

To estimate the extent of diffusion from ice-core data, we begin with the description of isotope diffusion outlined above. The computation of the convolution that yields Equation 2.4 can be performed in the frequency domain, using the convolution theorem:

$$\delta(z,t) = \delta(z,0) * \mathcal{G} \qquad \Rightarrow \qquad \hat{\delta}(z,t) = \hat{\delta}(z,0) \cdot \hat{\mathcal{G}}, \tag{2.7}$$

where $*$ represents convolution and $\hat{}$ represents the Fourier transform. The Fourier transform of a Gaussian is itself a Gaussian, and therefore the transfer function of the

diffusion process is given by:

$$\mathcal{F}(\mathcal{G}) = \hat{\mathcal{G}} = \exp\left(\frac{-k^2\sigma^2}{2}\right), \tag{2.8}$$

where $k = 2\pi f$ and f is the frequency of the signal.

Combining Equations 2.7 and 2.8, the expected loss in the amplitude of the signal at frequency f is given by:

$$\Gamma = \Gamma_0 \exp\left(\frac{-k^2\sigma^2}{2}\right), \tag{2.9}$$

where Γ_0 and Γ are the amplitudes of the signal at frequency f, before and after diffusion. Based on Equation 2.9, we can compute the expected power spectral density (PSD) of an ice-core section as:

$$P = P_0 \exp\left(-k^2\sigma^2\right), \tag{2.10}$$

where P_0 and P are the PSDs of the signal before and after diffusion. We assume that P_0 is constant (white noise) over short core sections, as discussed and justified in Johnsen et al. (2000) and Gkinis et al. (2014).

Spectral estimates of ice-core data sections will also be affected by noise generated during the laboratory measurement process. Taking this effect into account, the idealized model for the PSD of ice-core data is given by:

$$P = P_0 \exp\left(-k^2\sigma^2\right) + \left|\hat{\eta}\right|^2 \tag{2.11}$$

where $\left|\hat{\eta}\right|^2$ is the measurement noise.

The diffusion length σ can be calculated by optimizing the fit between Equation 2.11 and the PSD of a section of ice-core data. Repeating this method over consecutive, windowed sections of data yields diffusion-length estimates through the length of an ice-core record. Various spectral-estimation techniques can be used to produce the PSD of the data. In this work, we use Burg's spectral estimation algorithm (Burg, 1975), following the approach of Gkinis et al. (2014). Burgs method is preferable for this application because it is based

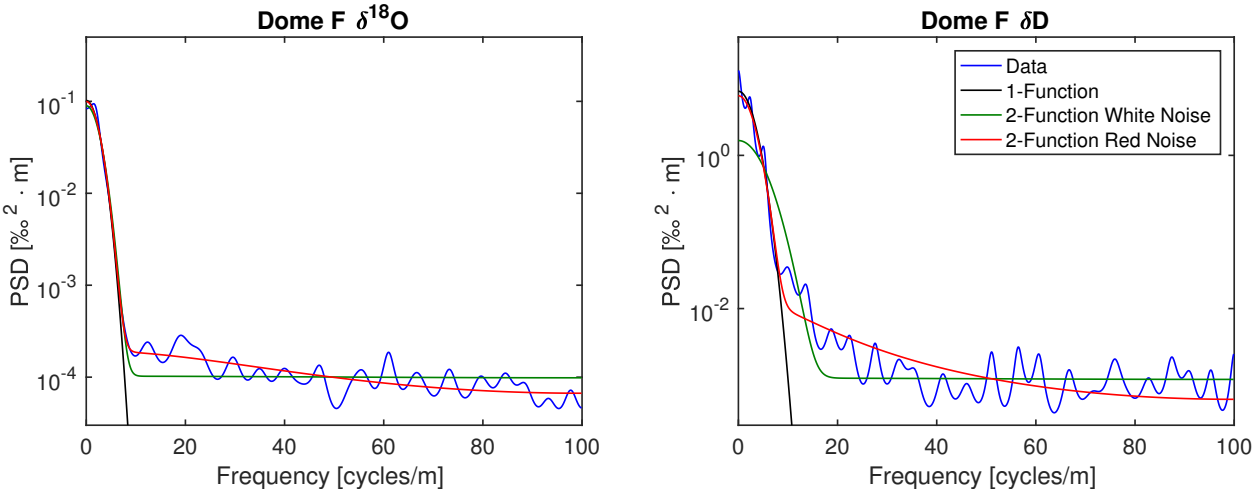

Figure 2.1: First-order (black curve) and 2-function models applied to the PSD of a section of Dome F data from 302-307 m depth. For the 2-function model we use both white noise (green curve) and red noise (red curve).

on a predictive autoregressive model and ice-core data are intrinsically autoregressive. In Figure 2.1 we give examples of estimated PSDs of a data section from the Dome F ice core for both δ^{18}O and δD (Svensson et al., 2015). The record was measured using the CFA approach presented in Gkinis et al. (2011a) with a nominal resolution of 0.5 cm. Note that the differences in the sloping of the spectra of δ^{18}O and δD are due to differences in how the CFA system affects each isotope ratio.

Based on Equation 2.11, two strategies emerge for estimating diffusion lengths from high-resolution ice-core data. A first-order approach is to use the first term of Equation 2.11 as the power spectral model P and tune σ to fit the power spectral estimate P' in a least squares sense in a range of low frequencies $[2, f_c]$ (Jones et al., 2017a). The value of f_c is manually chosen such that P' is dominated by the diffusion signal in this range of frequencies; as a result, measurement noise does not significantly affect the quality of the fit. A second approach is to include the noise signal $|\hat{\eta}|^2$ in the fit, using a 2-function model and thus fitting the model of P as described in Equation 2.11 to the spectral estimate P' across the full range

of frequencies. The advantage of the latter technique compared to the first-order approach is that it does not involve the subjective step of manually choosing the value of f_c. However, considering the full frequency range requires an accurate model for the measurement noise; otherwise, biases in the estimation of the diffusion length σ can emerge.

In Figure 2.1, both approaches are applied to the Dome F data section. For the first-order approach, we select $f_c = 20$ cycles/m (black line). For the 2-function model (green line), we first assume the measurement noise $|\hat{\eta}|^2$ is white. However, this approach results in a slight misfit in the range of frequencies 10-25 cycles/m. Next, assuming that the measurement noise is slightly red, as presented in Gkinis et al. (2011a, 2014) and Holme et al. (2018), we obtain a more satisfactory fit (red line). Red noise behavior is expected due to smoothing and memory effects in the measurement system. The spectral model used for the latter case is:

$$P = P_0 e^{-k^2\sigma^2} + \frac{\varsigma_\eta^2 \Delta}{\left|1 - a_1 \exp\left(-ik\Delta\right)\right|^2}, \tag{2.12}$$

where a_1, the AR-1 coefficient, and ς_η^2, the variance of the red noise, are variable parameters in the fit. The AR-1 coefficient determines the strength of correlation between two consecutive points in the series. For the δ^{18}O PSD in the left panel, the values for σ obtained with these different fitting approaches are 5.42, 5.11 and 5.34 cm, respectively. Although all three fits appear similar in the frequency range where the diffusive damping occurs, the anomalous value of 5.11 for the white-noise case illustrates how the misfit of the model can affect the estimation of diffusion length.

For some datasets, the problem of the misfit can lead to large errors in the estimation of diffusion length. Using the same section of ice from Dome F, but this time considering the δD signal, we observe a larger misfit (right panel). While the first-order approach using the cut-off frequency still produces a satisfactory fit to the part of the spectrum dominated by the diffusion signal, the 2-function model assuming white noise fails to yield an adequate fit. As seen in the spectrum, the power in the data in the range of frequencies 15-25 cycles/m deviates strongly from the expected model. Assuming red noise, the fit is significantly better

with an AR-1 coefficient $\alpha_1 = 0.64$, a value significantly higher than that used for the fit of the δ^{18}O signal. The resulting diffusion-length values for each fit on the δD PSD are 4.82, 2.79, and 4.62 cm, respectively. The 2-function model with the white noise assumption clearly does not effectively fit the data, while the red noise assumption and the first-order approach each fit the diffusion-damped frequencies well. Considering the inherent subjectivity of the cut-off frequency selection in the first-order approach and an evident misfit of the red-noise 2-function model (in the frequency range 15-25 cycles/m), it is not possible to judge which of the latter two diffusion-length estimates is more accurate.

2.5 Understanding PSDs of Different Ice-Core Datasets

In Figure 2.2 we present a collection of estimated PSDs from sections of various ice-core records and measurement techniques (discrete and CFA). The data have been normalized, showing the consistent effects of diffusive damping of high frequencies as well as measurement noise. Differences in measurement noise level can be explained by differences in the precision of the instrument used as well as by differences in data processing. In some cases, in the range of frequencies between $\sim$10 and 25 cycles/m (vertical dashed lines), the PSD deviates from the model of Equation 2.12, as in the δD section presented from Dome F. We plot δD for each dataset, except where only δ^{18}O is available (NGRIP, WDC discrete), since those data tend to exhibit the deviation more strongly than the δ^{18}O data.

In general, the PSDs of data from CFA systems tend to deviate from the theoretical spectrum (Equation 2.12) more strongly than those of discretely-measured data. This creates a problem for the estimation of diffusion length from CFA data. Figure 2.3 illustrates this problem on data sections from WDC and SPC, which exhibit greater deviation than the continuous Dome F and NEEM data. Even assuming $|\hat{\eta}|^2$ to be red noise, the misfit of the 2-function model on the WDC and SPC sections is greater than that on the Dome F δD data shown in Figure 2.1. This suggests that differences in the CFA systems used play a significant role in affecting the spectra. Various CFA systems may affect measured data slightly differently. For

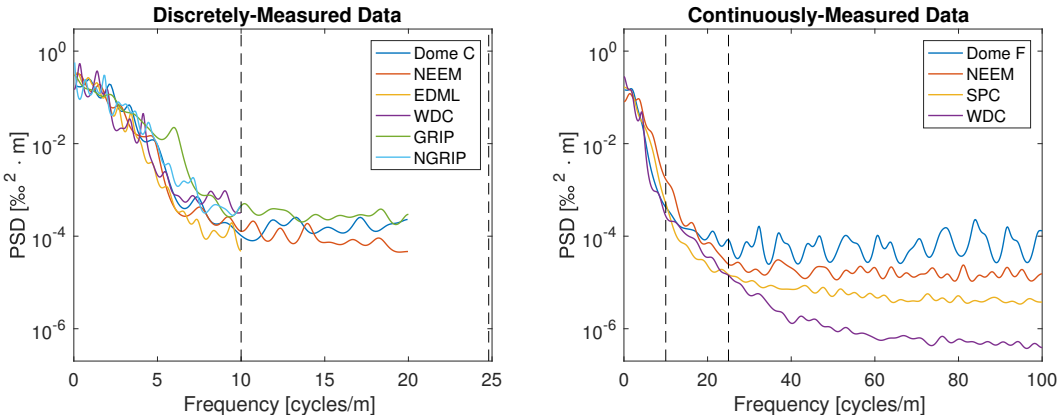

Figure 2.2: Estimated PSDs for discretely-measured (left panel) and continuously-measured (right panel) datasets. All data has been normalized by dividing by its standard deviation before making the spectral estimate. δD is plotted for all datasets, except where not available (NGRIP and WDC discrete). Discrete cores tend to follow the model of Equation 2.12, while continuous cores tend to deviate from that model between frequencies of 10 and 25 cycles/m and beyond (range highlighted by vertical dashed lines on each panel). Note the relatively constant value (i.e, white noise) of the PSDs for the discretely-measured data between 10 and 25 cycles/m.

example, the Copenhagen CFA system used for Dome F and NEEM uses a lower-precision (older-generation) Picarro instrument (Picarro L2120-i) than the INSTAAR system (L2130-i) used for WDC and SPC. Further, the Copenhagen CFA vaporizes the sample differently, which may result in a smaller smoothing effect on the data. Importantly, there is no evidence that the character of the deviation from Equation 2.12 changes with measurement time, for a given measurement system. We use replicate ice samples from the same section of ice core measured on the INSTAAR CFA system at different times. Figure 2.4 plots the PSDs from measurements of SPC from 1060 m to 1075 m depth. The blue and red curves show the original and replicate measurements, respectively. The PSDs do not differ significantly.

The influence of the CFA system on the spectral properties of the data may arise in a number of components of the system. Liquid-phase mixing takes place throughout the tubing of the CFA system. In particular, liquid water reservoirs, such as degassing and filtering units, may

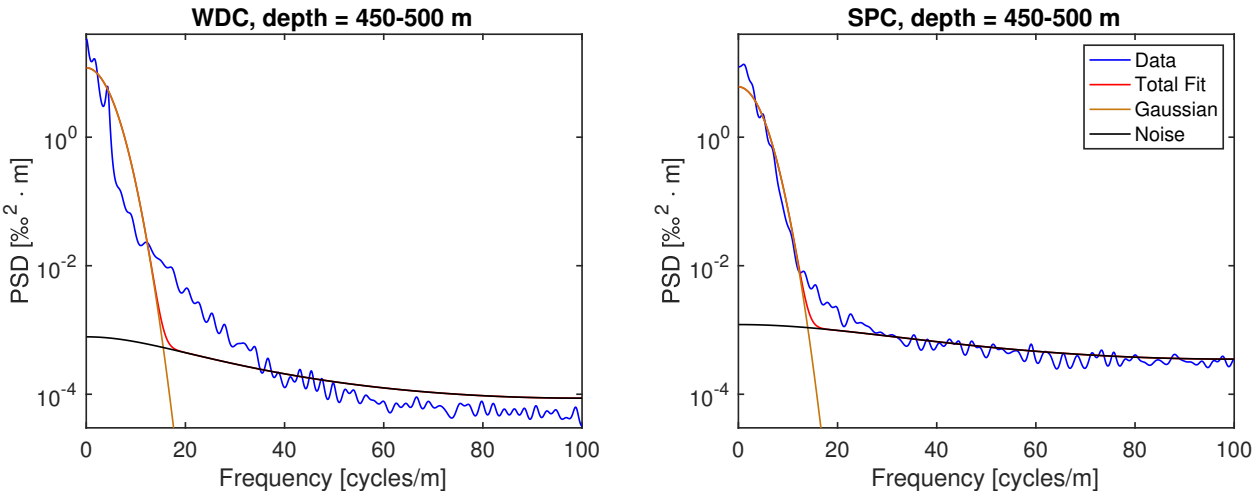

Figure 2.3: 2-function model (Equation 2.12) applied to WDC and SPC at 450-500 m depth. With only two functions, the model is unable to effectively fit the entire data spectrum.

enhance these effects. Attenuation of the signal due to mixing in the vapor phase can also be significant. Sample vaporization takes place at an operating pressure of ∼1 atm (Gkinis et al., 2011a; Jones et al., 2017b), while the operating pressure within the instrument cavity is only ∼65 mbar (Crosson, 2008). Under the higher pressure, significant smoothing occurs between the time of vaporization and the time of injection into the cavity. Additionally, memory effects arise from the particular nature of hydrogen bonding of the water molecule. Due to this intermolecular bonding, water molecules may adsorb to surfaces within the system downstream of the point of vaporization, potentially affecting subsequent measurements (Aemisegger et al., 2012). Some studies suggest the length, strength, and number of hydrogen bonds per molecule are different between H_2O and HDO (Soper et al., 2008), which helps explain the stronger memory effects observed in the δD signal in comparison to the δ^{18}O signal.

The influence of the CFA system on the spectral properties of the data may arise in a number of places, as meltwater from an ice sample is transferred through tubing and various reservoirs (Gkinis et al., 2011a). For example, when sample water is pumped into the debubbler (a 2

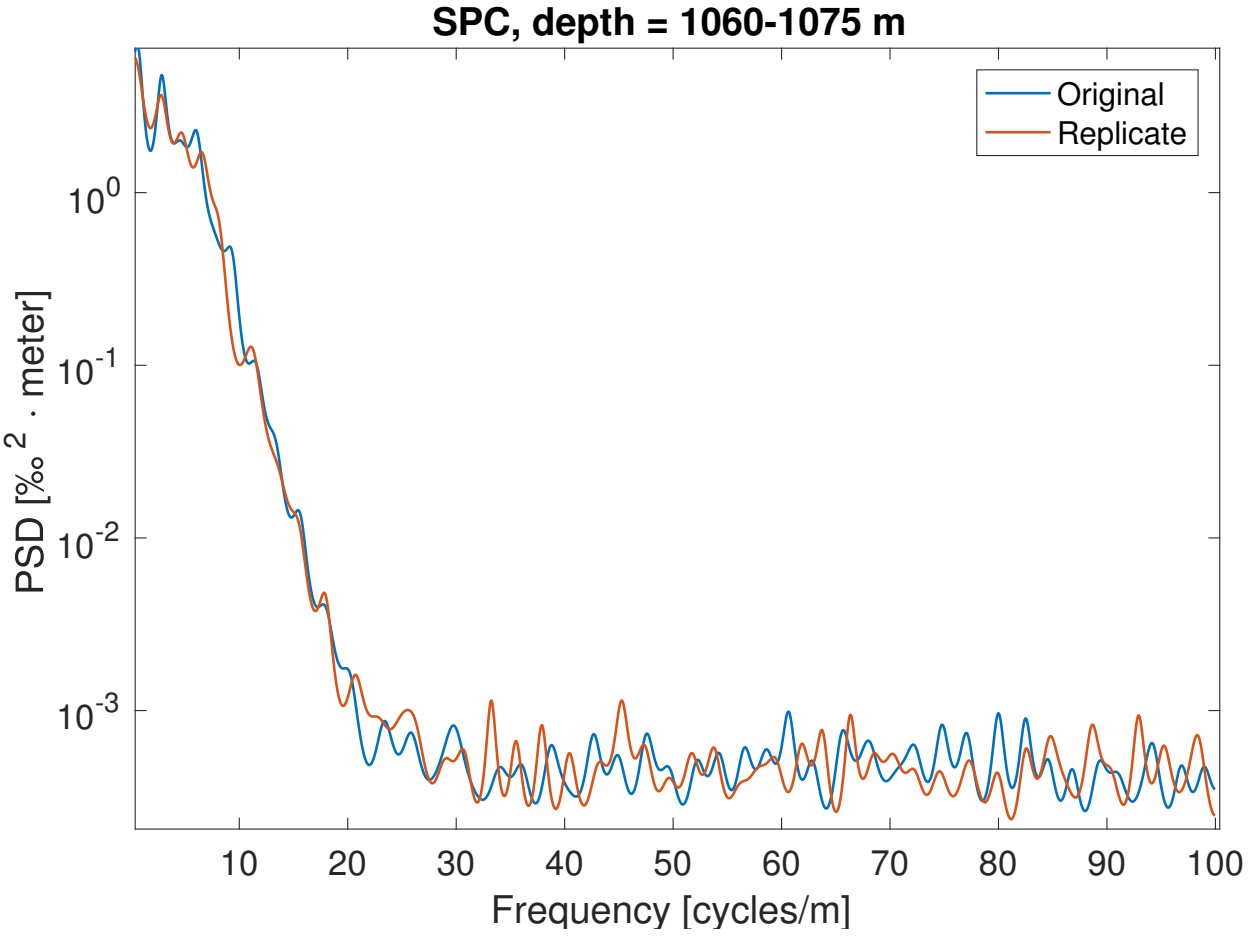

Figure 2.4: PSDs from replicate measurements of the same depths of SPC from 1060-1075 m. The blue curve shows the measurement from the original piece of ice. The red curve shows the measurement of a different sample from the same ice depth.

ml open-top vial that allows air bubbles to escape), some smoothing occurs. Also, smoothing occurs in the vapor phase when the sample is vaporized under relatively high pressure before it is injected into the Picarro instrument. The volumes of these reservoirs for the liquid and vapor phases affect how much smoothing occurs in a particular CFA system. Memory effects occur within the laser cavity of the Picarro instrument (Aemisegger et al., 2012). Because a stream of vapor is continuously pumped through the cavity, the isotopic memory from previous vapor, probably due to adsorption of water molecules to the cavity walls, will affect subsequent measurements.

We examine whether the effect of diffusive system smoothing can explain the spectral characteristics in continuous data PSDs by comparing real data to synthetic data with simulated smoothing. To characterize the smoothing of the system, we introduce an isotopic step-change into the INSTAAR CFA system, using ice that has been prepared in the laboratory from isotopically-distinct waters. The response of the system to the step change can be described as the product of two lognormal cumulative distribution functions (CDF):

$$\delta_{step}(t) = C_1 \cdot \left[1 + \mathrm{erf}\left(\frac{\ln(t) - \mu_1}{\sigma_1\sqrt{2}}\right)\right] \cdot \left[1 + \mathrm{erf}\left(\frac{\ln(t) - \mu_2}{\sigma_2\sqrt{2}}\right)\right] + C_2, \tag{2.13}$$

where t is time, μ_1 and μ_2 are the position of the distributions, σ_1, and σ_2 are the standard deviations of the CDFs and C_1 and C_2 are scaling factors.

To estimate the extent of system smoothing, we fit Equation 2.13 to the isotopic step-change, as shown in panels a) and b) of Figure 2.5. The resulting system-smoothing parameters are shown in Table 2.2. These are representative values and will vary slightly due to small changes in the system through time. The impulse response function calculated by the derivative of the step response is shown in panel c) of Figure 2.5 for both δ^{18}O and δD. The δD response is slightly wider, which suggests it is smoothed more within the system, confirming the result of Jones et al. (2017b). This difference may explain why the PSD of δD deviates more strongly from Equation 2.12 than the PSD of δ^{18}O. To simulate system smoothing, we apply the impulse response function as a filter on synthetic data.

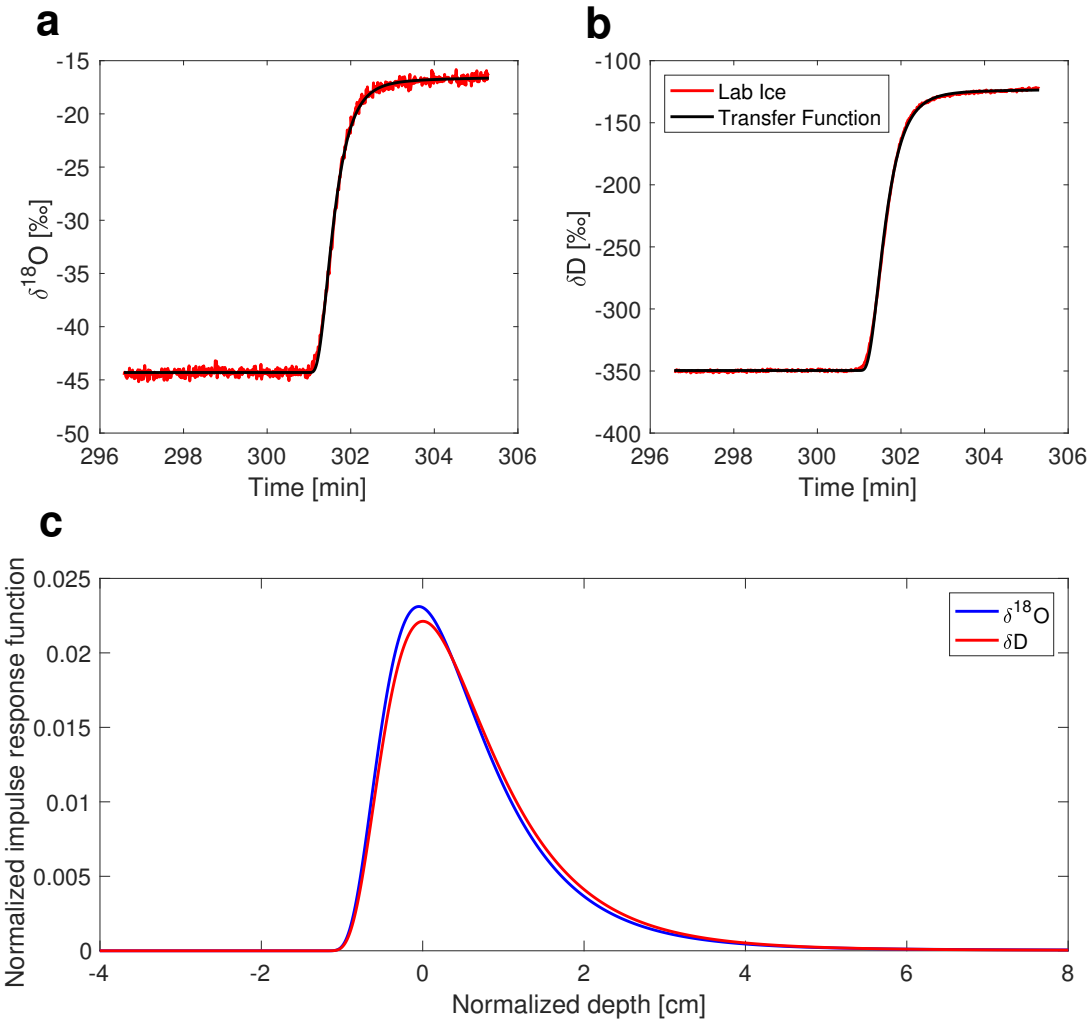

Figure 2.5: The characterization of the CFA system response to an isotopic step change. Panels a) and b) show the transfer function of Equation 2.13 fit to the isotopic step-change of the laboratory-prepared ice sample. The estimated parameters are listed in Table 2.2. Panel c) shows the normalized impulse response functions for δ^{18}O and δD plotted with respect to a normalized depth (assuming an average melt rate of 2.5 cm/min).

Table 2.2: The parameters characterizing the CFA system smoothing as estimated from the fit in Figure 2.5.

Isotope	C_1 [‰]	C_2 [‰]	μ_1 [sec]	μ_2 [sec]	σ_1 [sec]	σ_2 [sec]
δ^{18}O	59.76	-44.31	3.65	12.58	0.502	75.48
δD	626.67	-349.61	3.70	597.30	0.512	1647.79

We generate synthetic data by performing the following steps. First, to simulate data that represent the isotopic signal in surface snow, we generate an AR-1 process with a resolution of 0.1 cm and add white noise (ε_n) as:

$$\delta_n = a_1 \cdot \delta_{n-1} + \varepsilon_n. \tag{2.14}$$

The parameters involved in the generation of synthetic data are chosen such that the resulting δ_{final} time series visually resembles the WDC data (in this example from the depth interval $450 - 467$ m). Typical values for the autoregressive coefficient a_1 lie around $a_1 = 0.3$, while the standard deviation of ε_n is approximately 11 ‰ and 87.6 ‰ for δ^{18}O and δD, respectively.

Next, we introduce firn diffusion by convolving δ_n with a Gaussian filter ($\mathcal{G}$) with a standard deviation σ equal to 5.61 cm and 5.08 cm for δ^{18}O and δD, respectively:

$$\delta_{ice} = \delta_n * \mathcal{G}_{firn}. \tag{2.15}$$

Using the results of the step-response test we account for the smoothing imposed by the CFA system and perform one more convolution operation where the transfer function is the impulse response of the CFA system:

$$\delta_{cfa} = \delta_{ice} * \mathcal{G}_{cfa}. \tag{2.16}$$

where $\mathcal{G}_{cfa}$ is the derivative of Equation 2.13. Last, we sample the data at a 0.5 cm resolution and add white measurement noise:

$$\delta_{final} = \delta_{0.5} + \varepsilon_{meas}, \tag{2.17}$$

where $\varepsilon_{meas} = 0.05\,‰$ and $0.15\,‰$ for δ^{18}O and δD, respectively.

The sequence of steps described in equations 2.14-2.17 yields a PSD presented as the light grey curve in Figure 2.6. This curve can be described to a very good approximation by the model of Equation 2.12, but does not match the PSD of the WDC data (blue and red curves). We find that one way to approximate the WDC behavior is to slightly modify equation 2.15 by adding a white noise component ϵ as:

$$\delta_{ice} = \delta_n * \mathcal{G}_{firn} + \epsilon \tag{2.18}$$

Figure 2.6 shows the results of adding increasing levels of white noise ϵ (dark grey and black curves). With this noise addition, the PSDs of the synthetic data begin to resemble that of the WDC data, suggesting that there is a source of noise between the process of diffusion in the ice sheet and the process of smoothing within the CFA system. This source of noise may include the varying rate of sample flow through the system as well as temperature-dependent instrument noise. Nonetheless, Figure 2.6 gives a visual confirmation that, with the addition of white noise, the convolution of synthetic data with the system impulse response results in a time series that is similar to the measured WDC data. Later, we use this approach to generating synthetic data to evaluate new methods of estimating diffusion length.

2.6 Generalizing the Diffusion Estimation Technique

As discussed in Section 4, neither of the existing techniques for estimating diffusion lengths fully capture the spectral properties of continuous data. We consider two new techniques to address this problem. First, we add white noise to the data to mask the deviation in the mid-frequency range where the influence of the CFA appears to be most significant. Second, we add a third function to Equation 2.12, intended to capture the influence of the CFA-system smoothing on the spectrum. We illustrate these methods with δD data, which are more strongly affected than δ^{18}O by the CFA system. As we will show, both the noise-adding and 3-function techniques are effective.

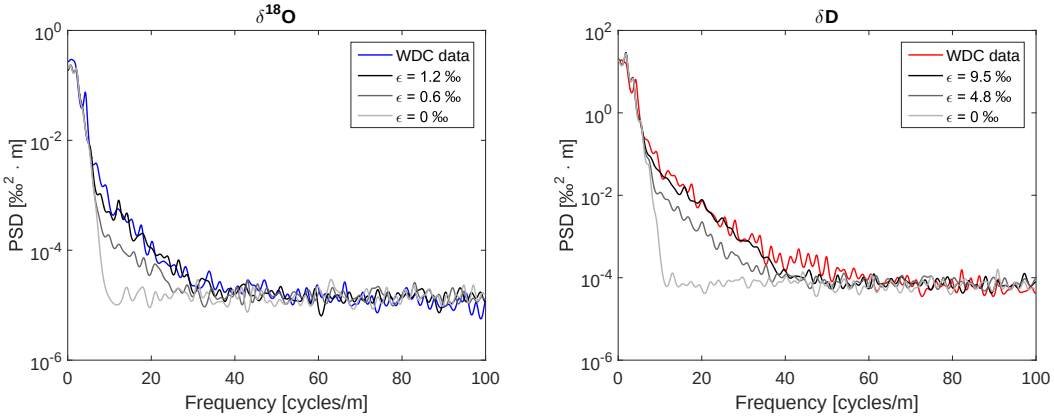

Figure 2.6: A comparison of PSDs from actual WDC data and from synthetic data with progressive levels of white noise added during the system smoothing process for both δ^{18}O and δD.

2.6.1 Technique 1: Adding White Noise

For this technique, we add normally-distributed noise to the data in the depth domain, which increases the high-frequency noise level in the frequency domain. This approach is equivalent to adding white noise as a constant to the data in the frequency domain and yields identical results. The resulting PSD masks the deviation, and the model of Equation 2.12 can effectively fit the altered PSD. Panel a) of Figure 2.7 illustrates this technique applied to a WDC data section.

We used a sensitivity test to evaluate the optimal magnitude of noise (standard deviation) to be added to the data. Adding too little noise does not effectively mask the deviation, but adding too much noise risks obscuring information. The test used a 500-year moving window throughout the WDC record. For each windowed section, 100 diffusion lengths were estimated by adding an increasing white noise level to the data in each window. A diffusion length was estimated for each tested noise level on each 500-year window. We define the optimal noise level as that at which the diffusion-length estimates stop changing with increasing noise. This level can be found when the gradient of diffusion length with

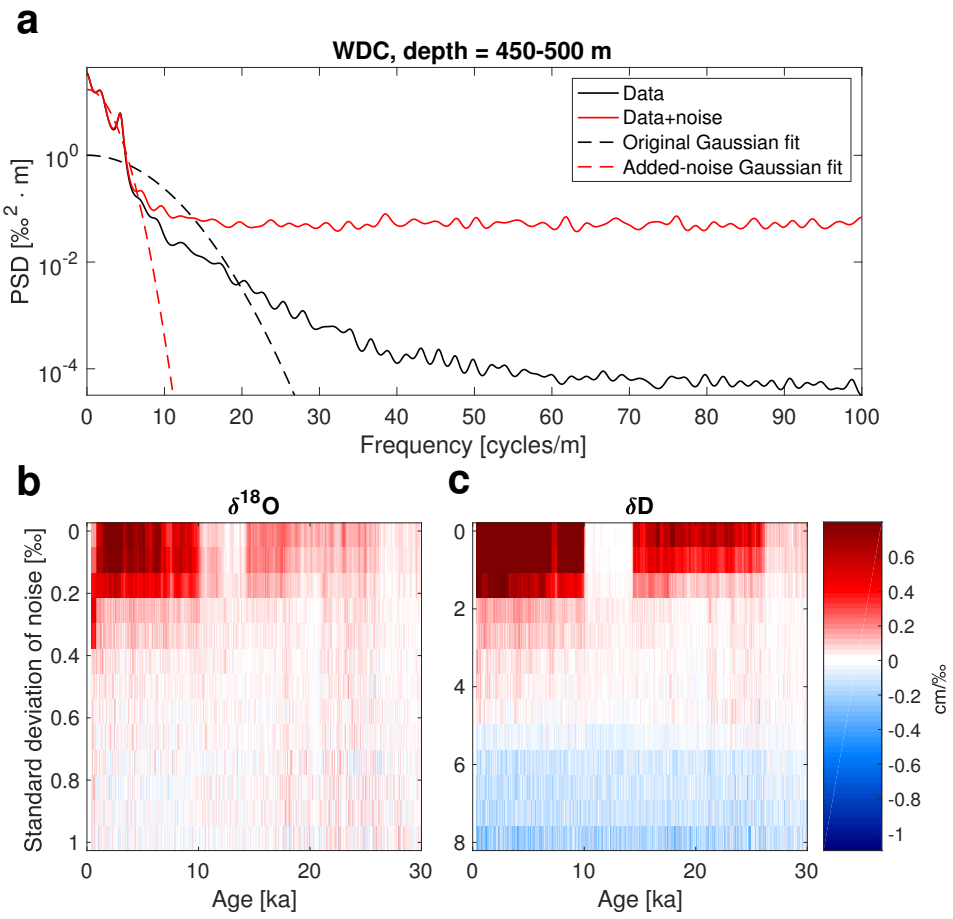

Figure 2.7: The noise-adding technique applied to a δD section from WDC. Panel a) shows the unmodified data (solid blue curve) and the data with noise added (solid black curve). The dashed lines represent the Gaussian functions fit using the 2-function fitting technique before and after adding noise to the data. With the added noise, the dashed black curve is able to effectively fit the data spectrum. Panels b) and c) demonstrate the sensitivity test for determining the optimal added noise level. For WDC, the gradient of estimated diffusion lengths with respect to noise level plotted as a function of age. At each age, the lowest noise level with a gradient of approximately zero is chosen as the optimal noise level to be added. Note that the strength of the colors is not symmetric, but the color bar is linear.

respect to the added noise level approaches zero. Panels b) and c) of Figure 2.7 show how this gradient changes for both δ^{18}O and δD throughout the WDC core. The optimal noise level is selected for each age as the lowest noise level that results in a gradient within 0.1 cm/‰ of 0 cm/‰. For WDC, we found that the optimal added noise is Gaussian-distributed noise with a standard deviation of 0.4 ‰ for δ^{18}O and 3.0 ‰ for δD.

2.6.2 Technique 2: 3-Function Model

This technique adds a third function to the model in Equation 2.12 to improve the fit to the data PSD. We tested the additions of three different functions, and determined which addition results in the most effective model. The three functions we tested were 1) a second autoregressive noise function, 2) a second Gaussian function, and 3) a folded normal distribution (FND) (Tsagris et al., 2014). The primary motivation for adding any of these functions is to better fit the mid-frequency range (10-25 cycles/meter) of the PSD. Additionally, there is a physical justification for using the FND model. As the absolute value of a Gaussian distribution, a FND is a function that smooths in only one direction. Since water is continuously flowing in one direction through the CFA system, the application of a FND is intended to mimic this one-sided effect. These models and those described earlier are summarized in Table 2.3. For each model, the parameter space is constrained such that the model can vary but remains within reasonable limits.

Table 2.3: Summary of models for the PSD of ice-core data. *Variable is manually selected and is not subject to fitting through optimization.

Model Name	**Description**	**Variable Parameters**
First-Order	$P = P_0 \exp(-k^2\sigma^2)$	P_0, σ
2-Function	$P = P_0 \exp(-k^2\sigma^2) + \lvert\hat{\eta}\rvert^2$ where $\lvert\hat{\eta}\rvert^2 = \frac{\varsigma_\eta^2 \Delta}{\lvert 1 - a_1 \exp(-ik\Delta)\rvert^2}$	P_0, σ, ς_η, a_1
Noise-Adding	$P = P_0 \exp(-k^2\sigma^2) + \lvert\hat{\eta}\rvert^2$ where data PSD has been altered	P_0, σ, ς_η, a_1 *noise added to data**
3-Function Double-Noise	$P = P_0 \exp(-k^2\sigma^2) + \lvert\hat{\eta}\rvert^2 + \lvert\hat{\eta}'\rvert^2$	P_0, σ, ς_η, a_1, ς_η', a_1'
3-Function Double-Gaussian	$P = P_0 \exp(-k^2\sigma^2) + P_0' \exp(-k^2\sigma'^2) + \lvert\hat{\eta}\rvert^2$	P_0, σ, P_0', σ', ς_η, a_1
3-Function FND	$P = P_0 \exp(-k^2\sigma^2) + \phi_0 e^{-(k\psi)^2} \lvert\, [1 - \Phi(-ik\psi)]\, \rvert^2 + \lvert\hat{\eta}\rvert^2$ where $\Phi(\psi) = \frac{1}{2}\mathrm{erfc}(-\frac{\psi}{2})$	P_0, σ, ϕ_0, ψ, ς_η, a_1

The results of applying the 3-function models are shown in Figure 2.8 for WDC and SPC. Panels a) and b) show the model that sums a Gaussian function and two autoregressive noise functions, henceforth the "double-noise model". With the addition of an autoregressive noise function, the total fit is visually improved for SPC, as compared to the 2-function model in Figure 2.3, but is still unable to effectively match the spectrum for WDC. Panels c) and d) show the model that sums two Gaussian functions and one autoregressive noise function, henceforth the "double-Gaussian model". Again, there is a visual improvement in the total fit as compared to the 2-function model fit, now in both SPC and WDC. Finally, panels e) and f) show the model that sums one Gaussian, one autoregressive noise function, and one FND function, henceforth the "FND model". Due to the close relationship between a Gaussian and a FND function, the fits are very similar in panels c) and e) and in panels d) and f).

2.6.3 Uncertainty of Diffusion-Length Estimation

To describe the uncertainty of the diffusion length estimated by each of these techniques, we use the 95th percent confidence bounds from the PSD estimate. To create a conservative estimate of uncertainty, we find the most extreme diffusion lengths possible given these PSD bounds, an approach similar to that of Jones et al. (2017a). The upper bound on diffusion length is found from the Gaussian function fit over a combination of the lowest frequencies of the upper PSD estimate bound with the highest frequencies of the lower PSD estimate bound. This combination yields the narrowest Gaussian function possible, and thus the greatest diffusion length. Conversely, the lower bound on diffusion length is found from combining the lowest frequencies of the lower PSD estimate bound with the high frequencies of the upper PSD estimate bound, resulting in the broadest Gaussian function possible and thus the smallest diffusion length. The frequency that separates the fit from the lower to upper PSD estimate bound is chosen at the lower-frequency side of the diffusion Gaussian, which maximizes the difference in the uncertainty bounds and thus creates a conservative

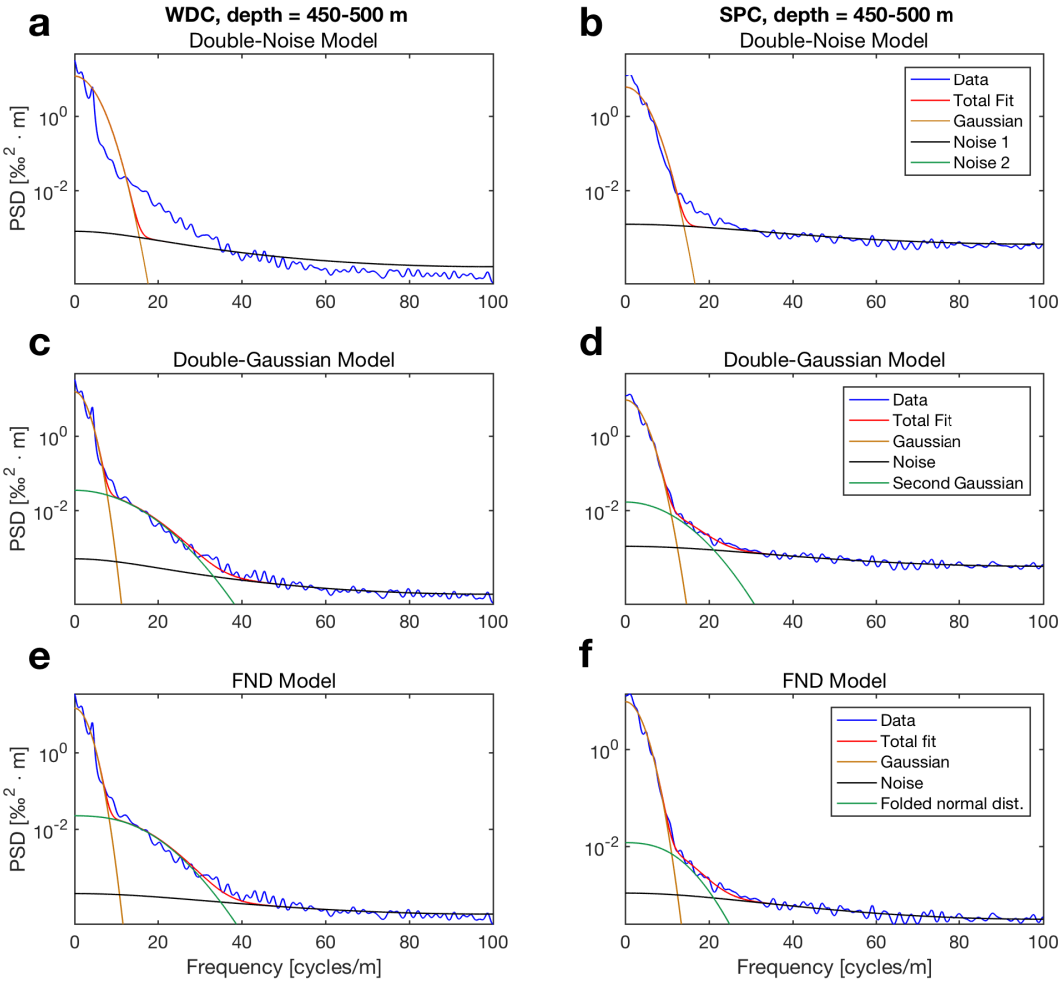

Figure 2.8: Each of the 3-function models applied to data sections from WDC and SPC PSDs. The double-noise model does not fit the full spectrum well, while both the double-Gaussian and FND models capture the full shape of the PSDs.

Table 2.4: Summary of performance of diffusion-estimate techniques on WDC δD data using 500-year windows.

Age of window [ka]	Noise-Adding $\sigma \pm 1$ Standard Deviation [cm]	Double-Gaussian $\sigma \pm 1$ Standard Deviation [cm]
1	5.59 ± 0.41	5.53 ± 0.43
5	3.91 ± 0.17	3.76 ± 0.19
10	2.95 ± 0.19	2.87 ± 0.20
15	3.13 ± 0.20	3.11 ± 0.21
20	2.00 ± 0.13	2.10 ± 0.15

estimate. Because the shape of the spectrum changes with depth, the separation frequency varies. Figure 2.9 demonstrates this approach with the double-Gaussian model, with dashed lines representing the upper and lower bounds on the fits of each function of the model. Table 2.4 lists diffusion-length estimates plus or minus one standard deviation for five windows throughout the WDC core.

2.7 Evaluating Fitting Techniques

To evaluate each fitting technique, we evaluate how reliably the techniques can be used to determine the known diffusion length of synthetic data. We construct synthetic data as described in Section 5. Qualitatively, both techniques result in effective fits on the synthetic data. To quantify the performance of each technique, we use a Monte-Carlo-like procedure. Each Monte Carlo iteration builds a unique time series having the same diffusion length, but a different noise realization. We then use both techniques to estimate diffusion lengths for 100 iterations of synthetic data. Table 2.5 gives the mean, standard deviation, and root mean square error of the diffusion-length estimates for both δD and δ^{18}O. Both techniques accurately estimate the input diffusion length, the noise-adding technique with a RMSE of

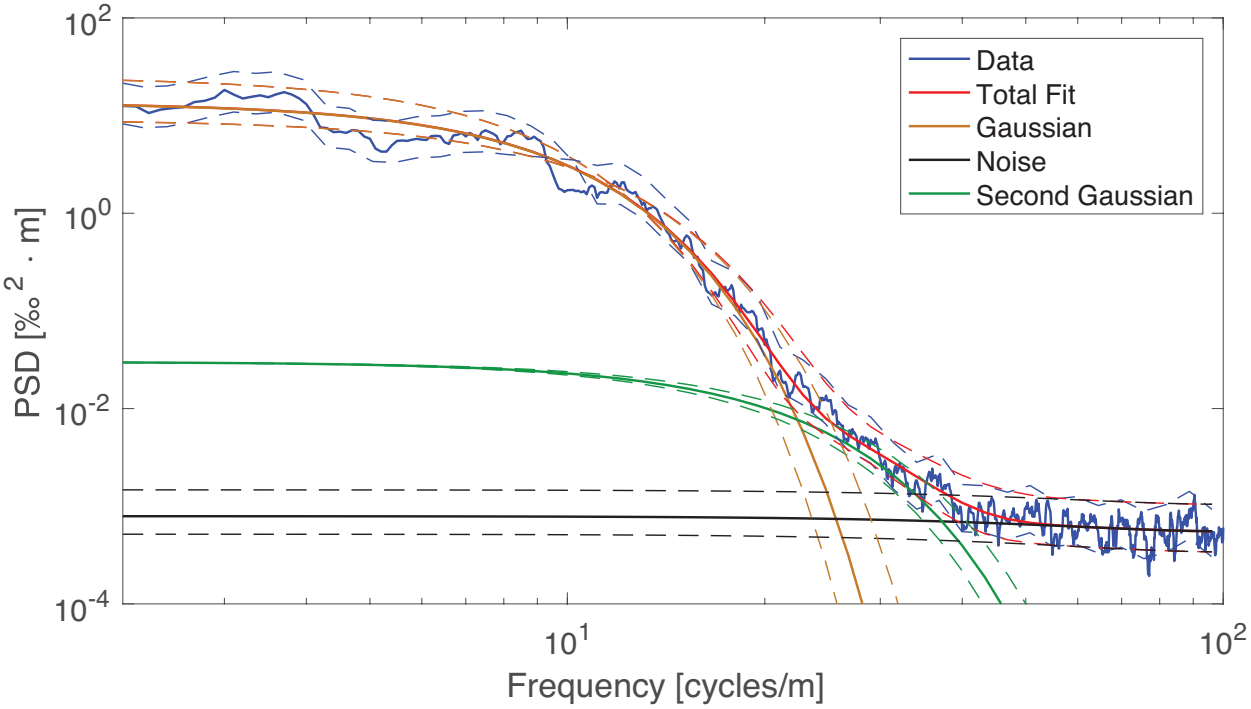

Figure 2.9: Illustration of uncertainty estimation for diffusion-length estimate for WDC δD data from 2505-2521 m depth. Solid lines show the data and the fit of each function. Dashed lines show the 95% confidence bounds for the spectral estimate of the data and the corresponding fits of the parameterization for upper and lower bounds. To estimate uncertainty for the diffusion-length estimate, the solid yellow curve yields the value and the dashed yellow curves yield the upper and lower bounds of 95% confidence. Axes are plotted in log-log space to expand the view of the lower frequencies and emphasize the fits of the diffusion length and its bounds (yellow curves).

0.25 cm for both δ^{18}O and δD, and the double-Gaussian model with a RMSE of 0.22 cm for δ^{18}O and 0.18 cm for δD. Thus, these values compare well with our estimates of uncertainty from Section 6.3.

As a second means of evaluation, we compared the effectiveness of each resulting fit over the entire WDC record. We calculated the adjusted coefficient of determination ($\bar{r}^2$) as a metric of goodness-of-fit with the data. The coefficient of determination (r^2) is calculated by comparing the variability of the estimation errors with the variability of the original values.

Table 2.5: Summary of performance of diffusion-estimate techniques on synthetic data of known input diffusion length.

Isotope	Input σ	Mean $\pm$ 1 Standard Deviation [cm]		RMSE [cm]	
	[cm]	Noise-Adding	Double-Gaussian	Noise-Adding	Double-Gaussian
δ^{18}O	5.61	5.60 ± 0.25	5.68 ± 0.20	0.25	0.22
δD	5.08	5.16 ± 0.23	5.09 ± 0.18	0.25	0.18

The adjusted coefficient of determination ($\bar{r}^2$) takes into account the number of variable parameters (p) as follows (Theil, 1961):

$$\bar{r}^2 = 1 - (1 - r^2)\frac{n-1}{n-p-1}, \tag{2.19}$$

where n is the sample size. For the noise-adding technique, $p = 5$; for the 3-function models, $p = 6$. Figure 2.10 plots the $\bar{r}^2$ values as a function of age for WDC. The $\bar{r}^2$ values of the double-Gaussian and FND models are indistinguishable, so we show only the double-Gaussian result in the figure. All four techniques provide good fits ($\bar{r}^2 > 0.9$) to the data, but the best fits are obtained with the double-Gaussian and FND models. For simplicity and computational efficiency, we prefer the double-Gaussian over the FND model.

Third, we compared the resulting diffusion-length estimates from the double-Gaussian model and the noise-adding technique. The left panel of Figure 2.11 shows the diffusion-length estimates from both techniques plotted with respect to age along with confidence bounds showing two standard deviations. The diffusion-length estimates were calculated over a moving 500-year window, shifting 100 years for each consecutive estimate. Both techniques reconstruct similar diffusion lengths throughout the record.

A fourth way of validating the techniques is by comparison with the technique using the first-order model, as discussed in Section 4, above. The right panel of Figure 2.11 shows this comparison for the WDC record, using the same data windows as in Jones et al. (2017a). The estimated diffusion lengths for all three techniques match within uncertainty bounds.

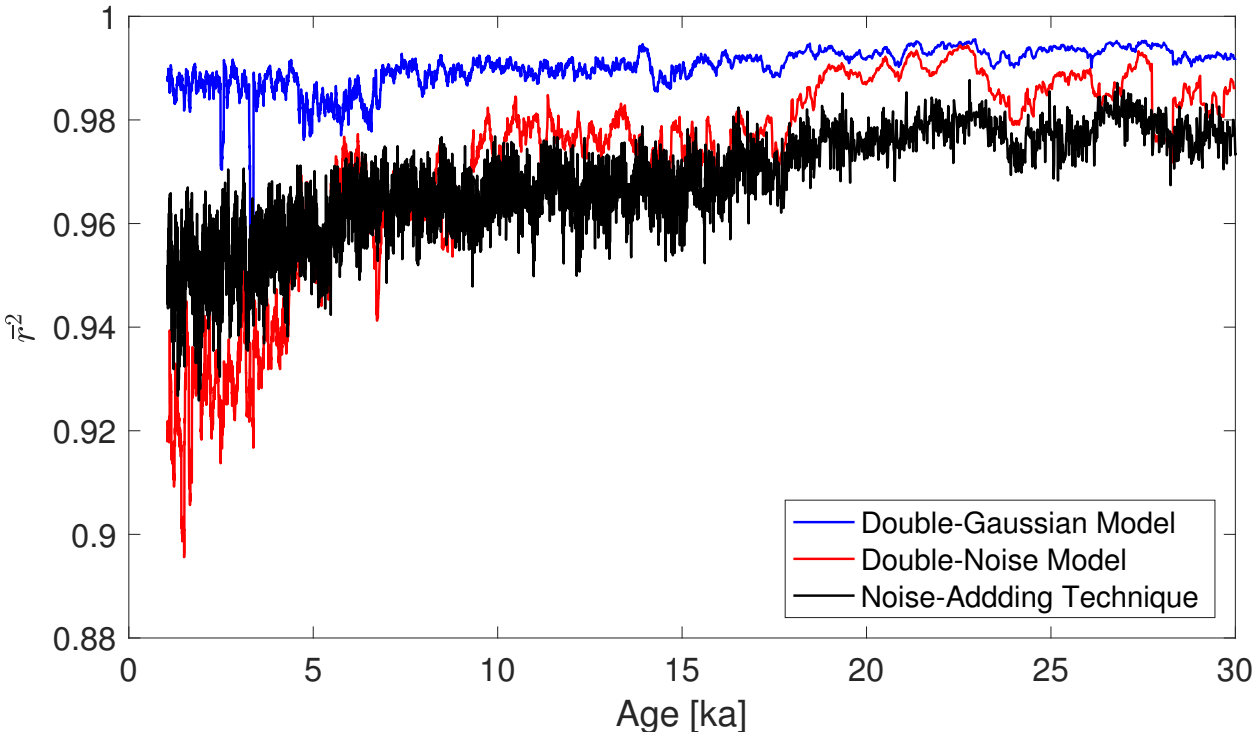

Figure 2.10: For WDC, the adjusted coefficient of determination ($\bar{r}^2$) plotted against age for each fitting technique. FND results are identical to the double-Gaussian results and are not shown.

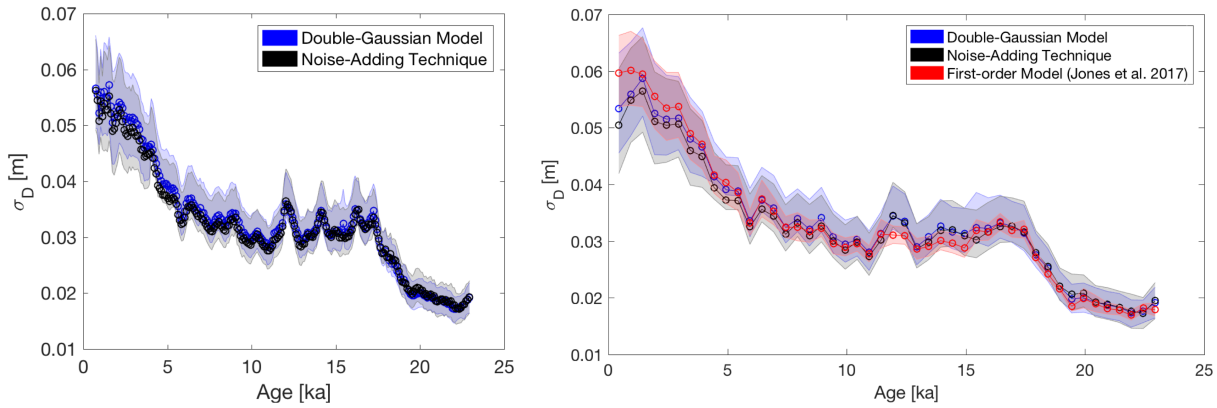

Figure 2.11: The left panel shows a comparison of diffusion-length estimates for the double-Gaussian model and noise-adding technique shown for δD for WDC. Confidence bounds show two standard deviations. The right panel shows a comparison of WDC δD diffusion-length estimates from the double-Gaussian model and noise-adding technique with those from Jones et al. (2017a). All diffusion lengths have been estimated on the same windows defined by Jones et al. (2017a). Confidence bounds show two standard deviations.

As each of these techniques is independent of one another, the confidence bounds together provide insight into how well diffusion lengths can currently be estimated from ice-core data.

We conclude that the best technique for estimating diffusion length is the double-Gaussian parameterization of the 3-function model. Although the FND model is better justified theoretically than the double-Gaussian model, it is effectively equivalent, though less computationally straightforward. The noise-adding technique produces similar results to the double-Gaussian model, but risks masking information in the signal, while the double-noise model does not fit the data as well as any of the other methods.

2.8 Discussion

The double-Gaussian technique provides a more efficient approach to estimating diffusion length than the manual cut-off method (Jones et al., 2017a), but yields essentially identical

results, and generalizes the application of previously-developed methods (Gkinis et al., 2014) to data from CFA systems. While our approach is nominally automated, in practice, we find that small alterations to the bounds of the fit parameters may be required to ensure that an accurate fit is obtained for each data window analyzed. For a given ice-core record, the general shape and magnitude of the PSDs will shift with increasing depth. Choice of different parameter bounds for distinct regimes within a dataset (e.g., Holocene and Glacial) may be necessary, as we have found with our results from the WAIS Divide ice core (Figure 2.11). Fine tuning of the upper bound on the P_0 parameter of the second Gaussian is particularly important as it separates the region of the PSD affected by diffusion from that affected by system smoothing.

With an approach that takes the above considerations into account, the double-Gaussian model can be used to produce diffusion-length estimates at sufficiently high resolution to recover relatively small features within the isotope-diffusion signal. For example, the high-resolution diffusion-length record in the left panel of Figure 2.11 resolves small peaks during the transition out of the glacial period (at ∼12, 14, and 17.5 ka) in the WAIS Divide ice core, while these features are subtle or altogether absent in the lower-resolution record in the right panel. Further investigation is required to determine whether these features reflect meaningful variations in climate or firn processes. In this context, a comparison with total air content from WDC would be helpful. This record is currently in development (Jon Edwards, pers. comm., 2017). If the comparison shows that total air content is also elevated where water-isotope diffusion lengths are anomalously high, this would suggest that anomalously low density firn could account for the exceptionally high diffusion lengths obtained at ∼12, 14, and 17.5 ka in the WAIS Divide ice core (as was previously suggested in Jones et al., 2017a).

In addition to providing informative comparisons with other proxy records, high-resolution diffusion-length records can also be used to improve current firn densification and diffusion models. With input temperature and accumulation-rate histories, firn models produce

synthetic, high-resolution water-isotope data. Comparison of diffusion lengths of these synthetic data with those from ice-core data can be used to evaluate what mechanisms within the model impact the resulting diffusion-length record. Current generation firn models do not reproduce the variability observed in the WDC diffusion-length record of Jones et al. (2017a). A model-data comparison approach could be used to examine what variables and boundary conditions are required to reproduce specific features in an ice-core diffusion-length record. This approach has the potential to both improve understanding of the climate signal as well as to improve firn models.

2.9 Conclusions

In this study we examine the diffusion signal in water-isotope data from a collection of ice-core records. We observe that the power spectral density of sections of water-isotope data can differ based on how the data are measured. In some cases, mostly with data measured on continuous-flow analysis systems, the PSD deviates from a simple model of diffusion plus instrument noise. We show that this deviation can be explained through modeling of the CFA system smoothing. Previous diffusion-length estimation techniques cannot effectively model these PSDs. We propose four new estimation techniques and find that the most effective method is the double-Gaussian parameterization of the 3-function model. These automated methods are efficient and effective in fitting all frequencies of the PSD. We validate the methods against one another, against synthetic data with known diffusion length, and against results estimated independently by Jones et al. (2017a). These methods can be used to determine diffusion lengths on water-isotope data from any ice-core record of sufficiently high resolution regardless of measurement technique. Diffusion-length records resulting from these automated methods have the potential to improve interpretation of ice-core and climate records as well as models of firn densification and isotope diffusion.

2.10 Acknowledgments

The research leading to these results was funded by the National Science Foundation grant numbers 1443105 and 1443328 as well as by the European Research Council under the European Union's Seventh Framework Programme (FP7/2007-2013) grant agreement #610055 as part of the ice2ice project. The authors would like to thank Christo Buizert for initial insights into the spectral characteristics of continuous-flow ice-core data as well as Gerard Roe for useful discussions on the evaluations of fitting techniques. By the time of publication, the data used in this paper from the South Pole ice core will be accessible at the NSF Antarctic database (http://www.usap-data.org). All other data used in this study have been previously published (Oerter et al., 2004; Gkinis et al., 2011a; Gkinis, 2011b; Steig et al., 2013; Gkinis et al., 2014; Svensson et al., 2015; Jones et al., 2017a; Holme et al., 2018). The MATLAB code used for the diffusion analysis techniques is accessible at https://github.com/emmakahle/diffusion_length_estimate.git.

BIBLIOGRAPHY

Aemisegger, F., Sturm, P., Graf, P., Sodemann, H., Pfahl, S., Knohl, A., and Wernli, H. (2012). Measuring variations of δ^{18}O and δ^{2}H in atmospheric water vapour using two commercial laser-based spectrometers: An instrument characterisation study. *Atmospheric Measurement Techniques*, *5*(7), 1491.

Brand, W. A., Geilmann, H., Crosson, E. R., and Rella, C. W. (2009). Cavity ringdown spectroscopy versus hightemperature conversion isotope ratio mass spectrometry; a case study on δ^{2}H and δ^{18}O of pure water samples and alcohol/water mixture. *Rapid Communications in Mass Spectrometry*, *23*(12), 1879–1884.

Burg, J. P. (1975). Maximum entropy spectral analysis (Doctoral dissertation). Stanford, CA: Stanford University.

Casey, K. A., Fudge, T. J., Neumann, T. A., Steig, E. J., Cavitte, M. G. P., and Blankenship, D. D. (2014). The 1500 m South Pole ice core: Recovering a 40 ka environmental record. *Annals of Glaciology*, *55*(68), 137–146.

Crosson, E. (2008). A cavity ring-down analyzer for measuring atmospheric levels of methane, carbon dioxide, and water vapor. *Applied Physics B*, *92*(3), 403–408.

Cuffey, K. M. and Steig, E. J. (1998). Isotopic diffusion in polar firn: Implications for interpretation of seasonal climate parameters in ice-core records, with emphasis on central Greenland. *Journal of Glaciology*, *44*(147), 273–284.

Dansgaard, W. (1954). The ^{18}O-abundance in fresh water. *Geochimica et Cosmochimica Acta*, *6*(5-6), 241–260.

Dansgaard, W. (1964). Stable isotopes in precipitation. *Tellus B*, *16*(4), 436–468.

Emanuelsson, B. D., Baisden, W. T., Bertler, N. A. N., Keller, E. D. and Gkinis V. (2015).High-resolution continuous-flow analysis setup for water isotopic measurement from ice cores using laser spectroscopy. *Atmospheric Measurement Techniques*, *8*(7), 2869–2883.

Epstein, S., Buchsbaum, R., Lowenstam, H. and Urey, H. C. (1951). Carbonate-water isotopic temperature scale. *Geological Society of America Bulletin*, *62*(4), 417–426.

Gkinis, V., Popp, T. J., Johnsen, S. J., and Blunier, T. (2010). A continuous stream flash evaporator for the calibration of an ir cavity ring-down spectrometer for the isotopic analysis of water. *Isotopes in Environmental and Health Studies*, *46*(4), 463–475.

Gkinis, V., Popp, T. J., Blunier, T., Bigler, M., Schupbach, S., Kettner, E. and Johnsen, S. J. (2011a). Water isotopic ratios from a continuously melted ice core sample. *Atmospheric Measurement Techniques*, *4*(11), 2531–2542.

Gkinis, V. (2011b). High resolution water isotope data from ice cores (Doctoral dissertation). Copenhagen, Denmark: University of Copenhagen.

Gkinis, V., Simonsen, S. B., Buchardt, S. L., White, J. W. C. and Vinther, B. M. (2014). Water isotope diffusion rates from the NorthGRIP ice core for the last 16,000 years - glaciological and paleoclimatic implications. *Earth and Planetary Science Letters*, *405*, 132–141.

Gupta, P., Noone, D., Galewsky, J., Sweeney, C., and Vaughn, B. H. (2009). Demonstration of highprecision continuous measurements of water vapor isotopologues in laboratory and remote field deployments using wavelengthscanned cavity ringdown spectroscopy (WSCRDS) technology. *Rapid Communications in Mass Spectrometry*, *23*(16), 2534–2542.

Holme, C., Gkinis, V., and Vinther, B. M. (2018). Molecular diffusion of stable water isotopes in polar firn as a proxy for past temperatures. *Geochimica et Cosmochimica Acta*, *225*, 128–145.

Johnsen, S. J., Clausen, H. B., Dansgaard, W., Langway, C. C. (1972). Oxygen isotope profiles through Antarctic and Greenland ice sheets. *Nature*, *235*(5339), 429–434.

Johnsen, S. J. (1977). Stable isotope homogenization of polar firn and ice. *Isotopes and Impurities in Snow and Ice*, 201–219.

Johnsen, S. J., Clausen, H. B., Cuffey, K. M., Hoffmann, G., Schwander, J. and Creyts, T. (2000). Diffusion of stable isotopes in polar firn and ice: The isotope effect in firn diffusion. *Physics of Ice Core Records*, 121–140.

Jones, T. R., Cuffey, K. M., White, J. W. C., Steig, E. J., Buizert, C., Markle, B. R., McConnell, J. R. and Sigl, M. (2017a). Water isotope diffusion in the WAIS Divide ice core during the Holocene and last glacial. *Journal of Geophysical Research: Earth Surface*, *122*, 290-309.

Jones, T. R., White, J. W. C., Steig, E. J., Vaughn, B. H., Morris, V., Gkinis, V., Markle, B. R. and Schoenemann, S. W. (2017b). Improved methodologies for continuous flow analysis of stable water isotopes in ice cores. *Atmospheric Measurement Techniques*, *10*, 617-632.

Jones, T. R., Roberts, W. H., Steig, E. J., Cuffey, K. M., Markle, B. R., and White, J. W. C. (2018). Southern Hemisphere climate variability forced by Northern Hemisphere ice-sheet topography. *Nature*, *554*(7692), 351.

Kerstel, E. T., Van Trigt, R., Reuss, J., and Meijer, H. A. J. (1999). Simultaneous determination of the $^{2}H/^{1}H$, $^{17}O/^{16}O$, and $^{18}O/^{16}O$ isotope abundance ratios in water by means of laser spectrometry. *Analytical Chemistry*, *71*(23), 5297–5303.

Lasaga, A. C. (2014). *Kinetic theory in the earth sciences*. Princeton, NJ: Princeton University Press.

Lis, G., Wassenaar, L. I., and Hendry, M. J. (2008). High-precision laser spectroscopy D/H and $^{18}O/^{16}O$ measurements of microliter natural water samples. *Analytical Chemistry*, *80*(1), 287–293.

Oerter, H., Graf, W., Meyer, H. and Wilhelms, F. (2004). The EPICA ice core Droning Maud Land: First results from stable-isotope measurements. *Annals of Glaciology*, *39*, 307–312.

Schoenemann, S. W., Schauer, A. J., and Steig, E. J. (2013). Measurement of SLAP2 and GISP $\delta^{17}O$ and proposed VSMOWSLAP normalization for $\delta^{17}O$ and $^{17}O_{excess}$. *Rapid Communications in Mass Spectrometry*, *27*(5), 582–590.

Simonsen, S. B., Johnsen, S. J., Popp, T. J., Vinther, B. M., Gkinis, V. and Steen-Larsen, H. C. (2011). Past surface temperatures at the NorthGRIP drill site from the difference in firn diffusion of water isotopes. *Climate of the Past*, *7*, 1327–1335.

Soper, A. K. and Benmore, C. J. (2008). Quantum differences between heavy and light water. *Physical Review Letters*, *101*(6), 065502.

Steig, E. J., Ding, Q., White, J. W. C., Küttel, M., Rupper, S. B., Neumann, T. A., Neff, P. D., Gallant, A. J. E., Mayewski, P. A., Taylor, K. C., Hoffmann, G., Dixon, D. A., Schoenemann, S., Markle B. M., Schneider, D. P., Fudge, T. J., Schauer, A. J., Teel, R. P., Vaughn, B., Burgener, L., Williams, J. and Korotkikh, E. (2013). Recent climate and ice-sheet change in West Antarctica compared to the past 2000 years. *Nature Geoscience*, *6*(5), 372.

Svensson, A., Fujita, S., Bigler, M., Braun, M., Dallmayr, R., Gkinis, V., Goto-Azuma, K., Hirabayashi, M., Kawamura, K., Kipfstuhl, S., Kjær, H. A., Popp, T., Simonsen, M., Steffensen, J. P., Vallelonga, P. and Vinther, B. M. (2015). On the occurrence of annual layers in Dome Fuji ice core early Holocene Ice. *Climate of the Past*, *11*, 1127–1137.

Theil, H. (1961). *Economic forecast and policy, vol. XV of Contributions to Economic Analysis*. Amsterdam, Netherlands: North-Holland Publishing Company.

Tsagris, M., Beneki, C. and Hassani, H. (2014). On the Folded Normal Distribution. *Mathematics*, *2*, 12–28.

van der Wel, G., Fischer, H., Oerter, H., Meyer, H. and Meijer, H. A. J. (2015). Estimation and calibration of the water isotope differential diffusion length in ice core records. *The Cryosphere*, *9*(4), 1601–1616.

Whillans, I. M., and Grootes P. M. (1985). Isotopic diffusion in cold snow and firn. *Journal of Geophysical Research*, *90*(D2), 3910–3918.

Chapter 3

A STATISTICAL INVERSE APPROACH TO RECONSTRUCT TEMPERATURE, ACCUMULATION RATE, AND LAYER THINNING FROM MEASURED PROPERTIES OF THE SOUTH POLE ICE CORE

Emma C. Kahle, Eric J. Steig, Michelle R. Koutnik, T.J. Fudge, Christo Buizert, Tyler R. Jones, Edwin D. Waddington

We use data from the South Pole ice core to constrain climate and ice conditions at the ice-sheet surface through the last 54,000 years. These constraints are produced from measurements of water isotopes, annual-layer thickness, and independent ice and gas timescales. The water-isotope diffusion length, based on spectral analysis of high-resolution water-isotope measurements, and Δage, the difference between the ice and gas timescales, both depend on firn properties and therefore on temperature and snow-accumulation rate. We use a Monte Carlo inverse approach to determine an ensemble of temperature and snow-accumulation rate histories from the South Pole ice core. The diffusion lengths and annual-layer thicknesses are used to constrain the thinning of annual layers in the ice sheet. The results provide a novel calibration of the traditional water-isotope paleothermometer. In contrast to previous paleotemperature studies in East Antarctica, after correction for sea water δ^{18}O variations, the isotope-temperature relationship varies between glacial and interglacial conditions at South Pole, and the temperature reconstruction gives a glacial-interglacial change of 6.2°C.

3.1 Introduction

Ice cores from polar ice sheets provide important records of past changes in climate and ice dynamics. Advances in analytical techniques have improved our ability to extract information from ice-core records. Water stable-isotope measurements provide information about temperature changes (Dansgaard, 1954, 1964; Jouzel et al., 1997). High-resolution measurements of seasonally-varying ion concentrations provide a means to count annual layers (Alley et al., 1997; Vinther et al., 2006; Sigl et al., 2016), and hence obtain information on past variations in accumulation rate Cuffey and Clow (1997); Veres et al. (2003); Fudge et al. (2016). The use of nitrogen and argon isotope ratios in trapped air bubbles also provides important constraints on past temperature and accumulation rate, because of the dependence of ice densification on climatic conditions (Severinghaus et al., 1998; Severinghaus and Brook, 1999).

Temperature and accumulation rate have long been targets of reconstruction from ice-core data (Lorius et al., 1990), but reconstructing these climate variables is not straightforward. For temperature, different reconstruction approaches use different ice-core measurements. The common approach calibrates water isotopes to temperature using an empirical spatial relationship on the ice sheet alongside atmospheric Rayleigh distillation models (Dansgaard, 1964; Jouzel et al., 1993). However, the spatial relationship is somewhat unreliable, particularly through time, due to atmospheric transport mechanisms (*e.g.* widely varying storm track pathways and isotopic recharge events (Jouzel et al., 1997), as well as the seasonality of accumulation that affects firn diffusion processes (Cuffey and Steig, 1998; Jones et al., in prep). A second approach uses measurements of δ^{15}N of N_2 in trapped air bubbles to provide information about past thermal gradients in the firn column and about the densification of snow in the firn layer of the ice sheet (Severinghaus et al., 1998). δ^{15}N measurements can be combined with models of firn densification to estimate past temperature changes; however, these firn models also require other constraints, such as accumulation rate through time.

Third, borehole thermometry provides a direct measurement of the modern temperature profile of the ice sheet, which can be related to temperature history through a heat diffusion model (Cuffey et al., 1995; Dahl-Jensen et al., 1998). However, borehole temperature provides a robust constraint on the temperature record only at ideal core sites with thick ice, relatively high accumulation rates, and simple ice-flow histories. Even under ideal glaciological conditions, borehole thermometry only preserves low-frequency information. Studies at different ice-core sites have used different combinations of these approaches, but challenges remain in fully constraining the proxy information to reconstruct temperature as well as other climate conditions.

In this work we overcome some of these challenges by combining information from multiple measurements in the same ice core from the South Pole. To constrain temperature and accumulation rate, we use two measures of firn properties, water-isotope diffusion length and Δage. To constrain the vertical strain of the ice sheet, we use the annual-layer thicknesses. We use a statistical inverse approach to optimize reconstructions of temperature, accumulation rate, and thinning function, producing a novel calibration of the traditional isotope paleothermometer.

3.2 The South Pole Ice Core

We apply our approach to new measurements made on the South Pole Ice Core (SPC14). Located near the geographic South Pole, SPC14 was drilled to a depth of 1751 meters, equivalent to an age of approximately 54 ka (Winski et al., 2019). Compared to other East Antarctic ice-core sites, the SPC14 site has a relatively high annual accumulation rate (8 cm w.e. yr^{-1}) (Casey et al., 2014) given its low mean-annual air temperature of -49°C (Lazzara et al., 2012) and surface firn temperature of -51°C (Severinghaus et al., 2001). This combination of conditions leads to a well-preserved, high-temporal-resolution record.

Due to its location far from an ice divide, SPC14 lacks complete constraints on certain

glaciological characteristics. First, the site lacks robust constraints on the thinning of annual layers at depth. While many ice-core sites are located at or near ice divides where horizontal ice flow is minimal, SPC14 is located about 200 km away from the ice divide, and the modern surface velocity is 10 m yr^{-1} (Casey et al., 2014). Furthermore, the subglacial topography is poorly known beyond 70 km along flow upstream from the site. This lack of information presents a challenge for modeling ice flow, particularly at greater depths, and therefore also for determining the strain history, which is required for the conversion of layer thickness to accumulation rate. Second, SPC14 lacks the favorable glaciological conditions for borehole temperature reconstructions, which have been used at other ice-core sites to provide an independent constraint on temperature history (Dahl-Jensen et al., 1998; Cuffey et al., 1995, 2016). Though the accumulation rate at South Pole is relatively high given the site temperature, it is low enough that heat diffusion has wiped out the most useful borehole temperature information. In the absence of reliable ice-flow modeling and borehole thermometry, this work provides necessary constraints on temperature and snow-accumulation rate.

3.3 South Pole Ice Core Information

To create the final data sets used in this analysis, we use the independent ice and gas timescales alongside the water-isotope measurements. Here we describe the information derived directly from ice-core measurements as well as the secondary data sets derived from that information.

3.3.1 Ice Timescale and Annual-Layer Thickness

Winski et al. (2019) developed the SPC14 ice timescale using a combination of annual layer-counting and stratigraphic ties (primarily volcanic events recorded in sulfate concentrations) to the timescale from the WAIS Divide ice core (WDC) (Buizert et al., 2015; Sigl et al.,

2016). Due to its high accumulation rate and high temporal resolution, WDC provides a good benchmark for SPC14 ice and gas timescales. The ice timescale was constructed by stratigraphic matching of 251 volcanic tie points between SPC14 and WDC. Between tie points in SPC14, identification of individual layers from seasonal cycles in sodium and magnesium ions produced annual resolution of the timescale in the Holocene (through 11.3ka). At older ages, despite lack of annual resolution, the uncertainty of the timescale remains within 124 years relative to WD2014.

Below the firn layer, the solid ice maintains a constant density but continues to thin vertically due to extensional flow of the ice sheet. Due to this process, the thickness of annual layers of snow that fell on the surface progressively decreases through depth in the ice sheet. The SPC14 record of annual-layer thickness λ is determined based on the depth between successive years in the SP19 timescale (Winski et al., 2019), as defined by:

$$\lambda = \frac{diff(depth)}{diff(age)}, \tag{3.1}$$

where $diff(depth)$ and $diff(age)$ are the differences between successive depth and age points in the timescale.

Figure 3.1 shows the layer thickness data set for SPC14. The uncertainty on the layer thickness is determined by the relative age difference between the top and bottom of the interval, and not by the absolute age. We use an uncertainty of 10% based on the uncertainty associated with interpolation between sparse tie points (Fudge et al., 2014). We average layer-thickness values over bins of 250 years to produce a resolution equivalent to that of diffusion length, our lowest-resolution data set.

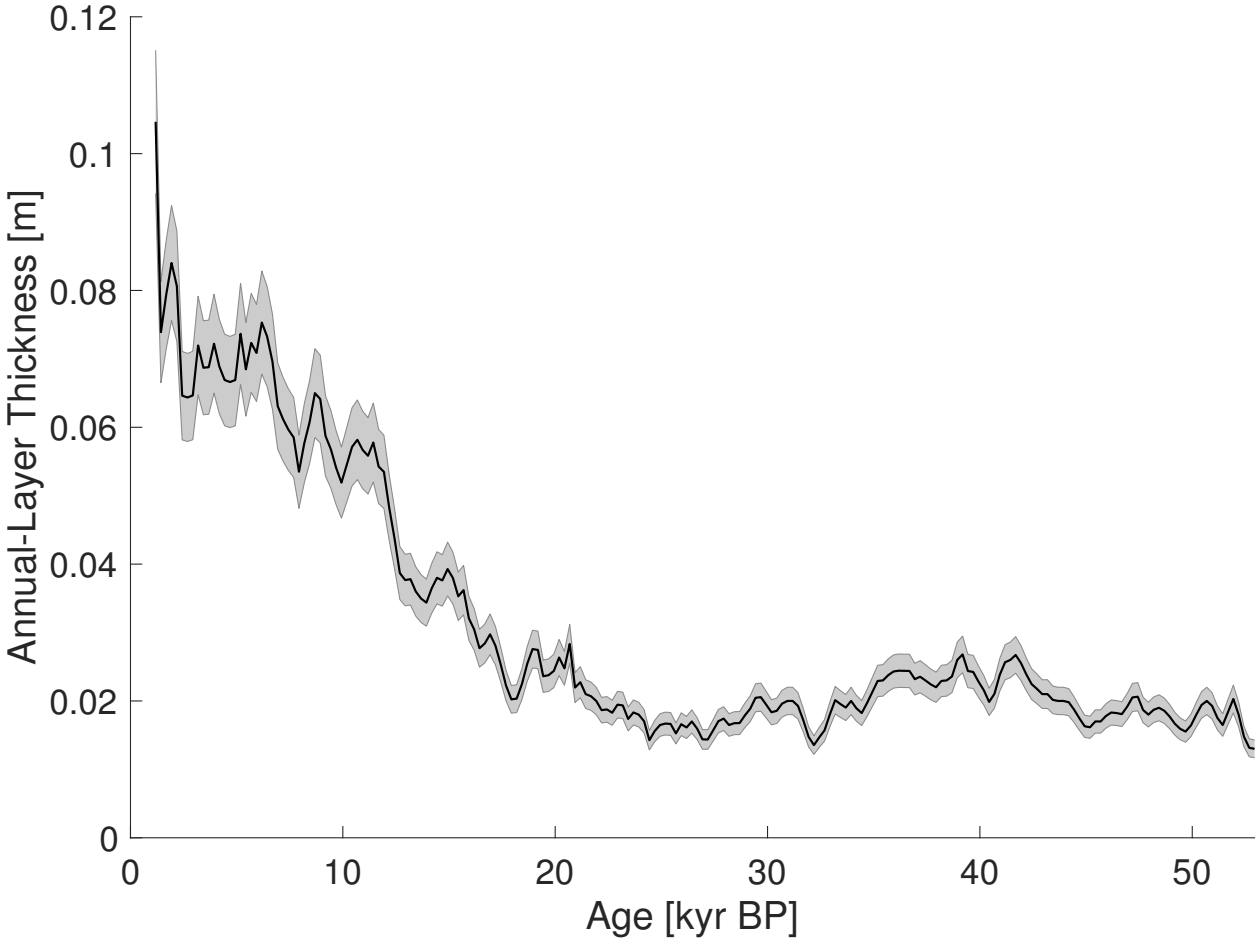

Figure 3.1: SPC14 annual-layer thickness data averaged over bins of 250 years.

3.3.2 Gas Timescale and Δage

Because the firn is permeable, air can move through interconnected pathways in the ice lattice. Distinct bubbles close off at the bottom of the firn layer, and younger air is trapped within older ice (Schwander et al., 1988; Blunier and Schwander, 2000). Gas diffusion stops and bubbles are trapped at the lock-in depth, defined as the depth at which the effective molecular diffusivity of the gas is reduced to one thousandth of the free air diffusivity (Buizert et al., 2013). The difference in age between the ice and trapped air bubbles at the same depth in the ice core is the Δage. The magnitude of this age difference depends on the rate of firn

densification.

The Δage data set for SPC14 is calculated as the difference between the SPC14 ice and gas timescales (Epifanio et al., in prep). Unlike past methods, this empirical calculation of Δage does not use a firn model (*e.g.* Buizert et al. (2012)), but is determined completely by matching the high-resolution records of CH_4 between the SPC14 and WDC gas timescales. At each of the CH_4 tie points, the SPC14 Δage was calculated empirically, after which a cubic spline fit was used to derive a continuous Δage curve for all depths. Because the WDC Δage has relatively low absolute uncertainty (better than 100 years), the SPC14 Δage relative uncertainty is small. For uncertainty, we use 15% of the value (Buizert et al., 2015). As a fraction of Δage, the SPC14 Δage uncertainty is relatively small. Due to the empirical nature of the gas timescale, the SPC14 Δage record is the first to be determined without a forward model driven by temperature and accumulation rate. Moreover, SPC14 Δage was obtained without relying on the additional constraint of δ^{15}N to determine close-off depth. Figure 3.2 shows the Δage record for SPC14. As with layer thickness, we have averaged values into bins with a resolution of 250 years.

3.3.3 Water-Isotope Measurements and Diffusion Length

We measured water-isotope ratios at an effective resolution of two measurements per cm for the entirety of SPC14 using the continuous flow analysis (CFA) system at the Institute for Alpine and Arctic Research at the University of Colorado Boulder (Jones et al., 2017a; Steig et al., in prep). Measurements were made using Picarro Inc. cavity ring-down laser spectroscopy (CRDS) instruments, models L2130-i and L2140-i. All three isotopic ratios were measured (δ^{18}O, δ^{17}O, and δD). We use the standard notation for δ^{18}O defined as:

$$\delta^{18}O_{sample} = \frac{^{18}O}{^{16}O_{sample}} / \frac{^{18}O}{^{16}O_{VSMOW}} - 1,$$

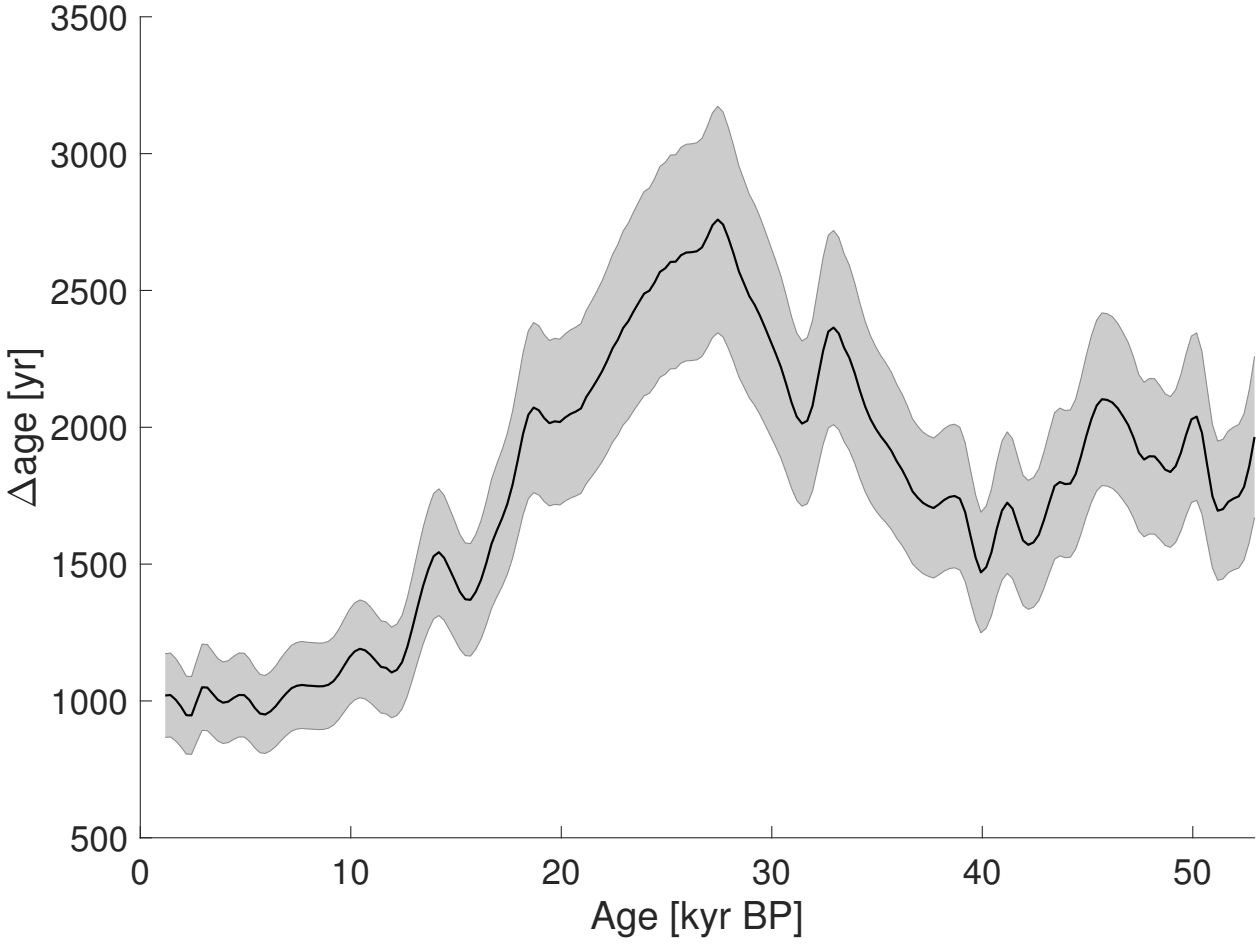

Figure 3.2: SPC14 Δage data averaged over bins of 250 years.

where VSMOW is Vienna Standard Mean Ocean Water. δ^{17}O and δD are defined similarly. Figure 3.3 shows the δ^{18}O measurements plotted against depth and against age. These measurements were used to calculate the water-isotope diffusion length.

After original deposition as snow on the ice sheet surface, variations in the water-isotope profile are affected by diffusion in the firn. In the firn layer, the interconnected air-pathways among ice grains allow water isotopes to diffuse in the vapor phase along gradients of concentration (Johnsen, 1977; Whillans and Grootes, 1985; Cuffey and Steig, 1998). At the base of the firn column, this diffusion process ceases when individual air bubbles are closed off in

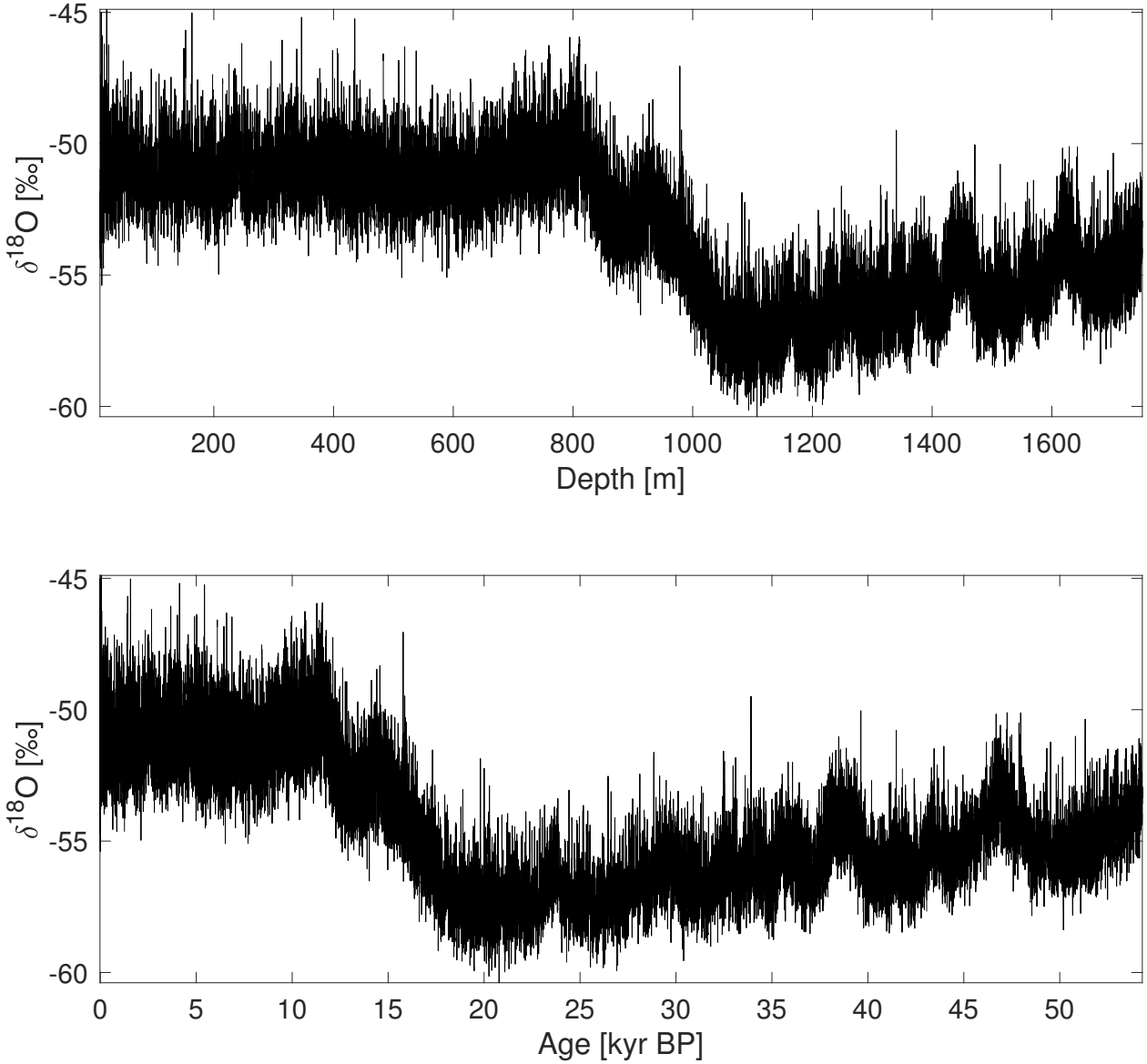

Figure 3.3: The SPC14 high-resolution water-isotope record plotted against depth (top panel) and age (bottom panel).

the solid ice.

Diffusion of water isotopes through the solid ice continues below this depth, but this process is orders of magnitude slower than the vapor diffusion in the firn (Johnsen et al., 2000).

Solid-ice diffusion will have a larger effect where ice is older and warmer, closer to the bed. SPC14 reaches an age of only 54ka at 1750 m depth, where the ice is still younger and much colder than basal ice.

The extent of diffusion is quantified as the diffusion length, the mean cumulative diffusive-displacement in the vertical direction of water molecules relative to their original location in the firn at the time of deposition. While ice is in the firn, this parameter is affected by both the density profile of the firn, as well as the firn temperature. In the solid ice below the firn, the diffusion length is further altered by vertical thinning of layers. While firn diffusion causes water molecules to spread out, thinning in deeper ice pulls the water molecules back towards their original positions. This process effectively counteracts the effect of firn diffusion and thus decreases the diffusion length. Because of this dual-dependence on both firn and solid-ice properties, diffusion length is an important piece of information within our overall strategy of combining firn and layer-thinning processes.

Calculation of diffusion length relies on the high-resolution water-isotope record to resolve the diffusive smoothing of the highest-frequency variations in the water-isotope profile. Through spectral analysis of the ice-core water-isotope record, the diffusion length can be estimated based on the extent of damping of the high frequencies (Gkinis et al., 2014; Jones et al., 2017b). We follow the method of Kahle et al. (2018) to estimate diffusion length through the SPC14 record for each water-isotope ratio. We use data sections of 250 years and calculate the power spectrum for each section in terms of cycles meter^{-1}. For each power spectrum, we estimate a diffusion length σ by fitting the data with a model of a diffused power spectrum and a model of two components of the measurement-system noise, described as (Kahle et al., 2018):

$$P = P_0 \exp(-k^2\sigma^2) + P_0' \exp(-k^2\sigma'^2) + |\hat{\eta}|^2, \tag{3.2}$$

where k is the wavenumber, $|\hat{\eta}|^2$ is the measurement noise, and P_0, P_0', and σ' are variable

fitting parameters.

We calculate the diffusion length for each of the three water-isotope ratios measured on the core. To combine the information from each isotope, we use the different diffusivities of each isotope to convert the δ^{17}O and δD diffusion lengths to equivalent values for δ^{18}O. For the diffusion-length record in our analysis, we use the mean of these three estimates. Figure 3.4 shows the δ^{18}O-equivalent diffusion-length values as estimated from δ^{18}O (blue), δ^{17}O (green), and δD (red) measurements. The uncertainty is estimated directly from the method in (Kahle et al., 2018) and varies from 2-33% of the value throughout the core.

To produce a record that reflects only firn conditions and vertical strain of the ice, we correct the diffusion-length estimates to account for diffusion in the CFA measurement system, following Jones et al. (2017a), and for diffusion in the solid ice, following Gkinis et al. (2014). These effects are both small, each accounting for only 4% of the total diffusion length at the bottom of the core.

3.4 Forward Model

We relate these data sets to the climate variables of interest through a forward model. We refer to this as a "forward model" because it estimates what we can observe as a function of the climate forcing we want to understand, the same direction that these processes occur in nature. The forward model simulates processes that occur through all depths of the ice sheet, separating processes the occur in the firn from those that occur in the solid ice below. Figure 3.5 illustrates the structure of the model, including a firn-densification model, a water-isotope diffusion model, and a simple function for vertical strain. The following section describes how each model input is used in the various forward-model components to produce each model output.

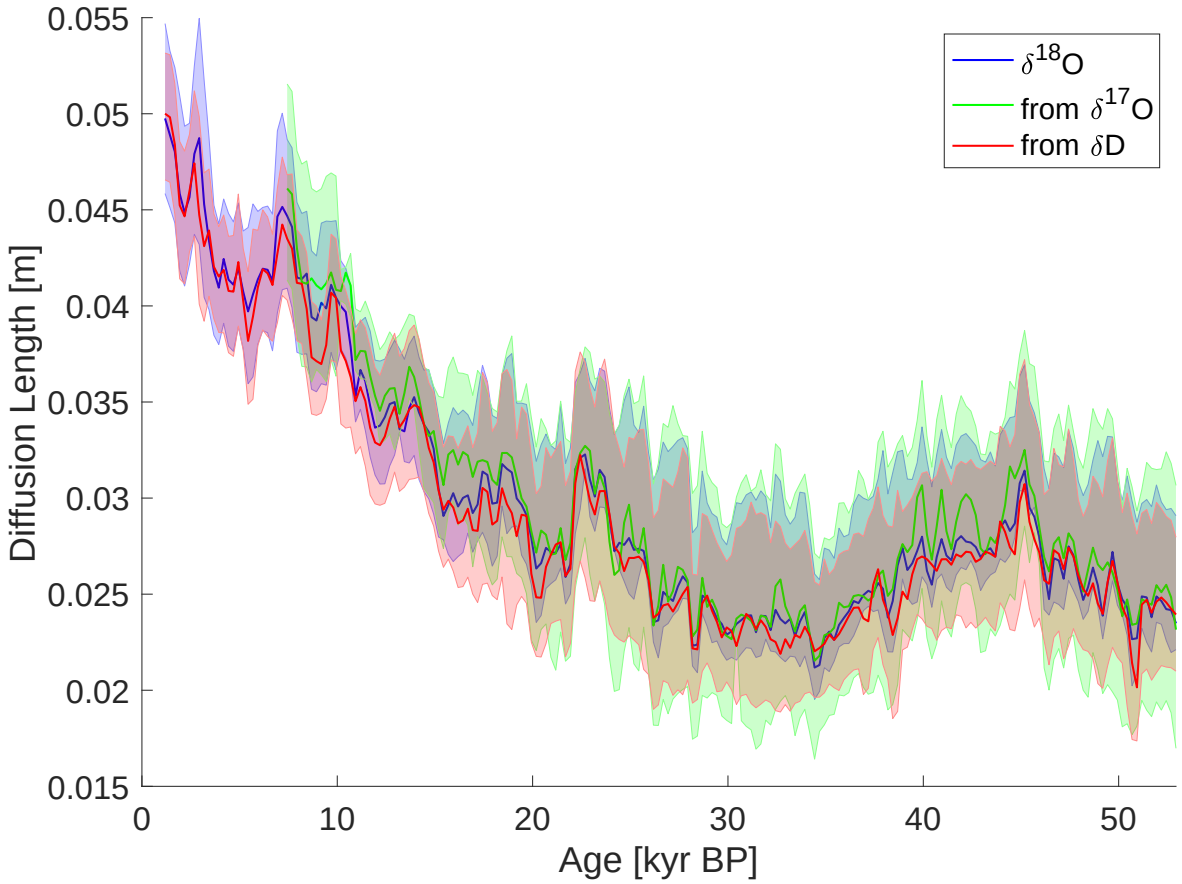

Figure 3.4: SPC14 diffusion lengths plotted versus age. Diffusion lengths from δ^{17}O (green) and δD (red) have been converted to δ^{18}O-equivalent values.

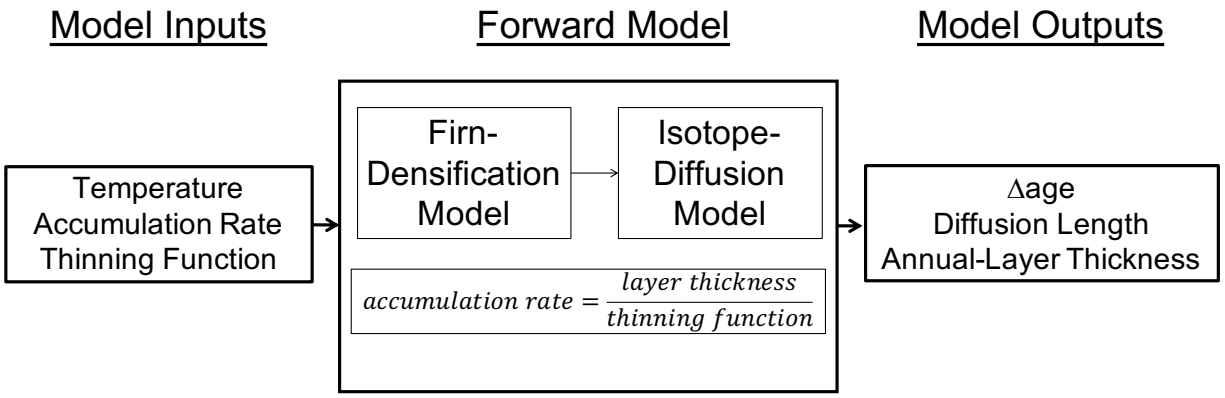

Figure 3.5: The forward model includes firn processes through a firn-densification model and isotope-diffusion model as well as solid-ice processes through the equation for vertical strain. Together, these components relate the data sets to the climate variables of interest.

3.4.1 Firn Densification

The firn layer comprises the upper tens of meters of the ice sheet where snow is progressively densifying into solid ice. As successive layers of snow fall on the surface of the ice sheet, the increase in overburden pressure causes the underlying ice crystals to pack closer together. The rate of this densification is set primarily by temperature and accumulation rate. To describe this densification process, many models have been developed, some based only on empirical data and others incorporating parameterizations of physical properties (e.g. Barnola et al. (1991); Goujon et al. (2003); Arthern et al. (2010); Morris and Wingham (2014)).

The Herron and Langway (1980) (HL) firn-densification model is the benchmark empirical model, based on depth-density data from Greenland and Antarctic ice cores. We model the depth-density profile of the firn using the HL framework due to its simplicity and its good match with measurements of the modern South Pole firn density. The HL model includes two depth zones to account for differences in densification processes in the upper and lower firn. Densification happens quickly in the upper firn by grain settling and then more slowly deeper in the firn as grain sintering becomes the dominant densification mechanism. The

density at depth h is calculated by:

$$\rho_h = \frac{\rho_i Z_x}{1 + Z_x}, \tag{3.3}$$

where Z_x is given by the following for the upper and lower firn zones, respectively:

$$Z_{upper} = \exp\left(\rho_i k_0 h + \ln \frac{\rho_0}{\rho_i - \rho_0}\right) \tag{3.4}$$

$$Z_{lower} = \exp\left(\frac{\rho_i k_1 (h - h_{crit})}{A^{0.5}} + \ln \frac{0.55}{\rho_i - 0.55}\right), \tag{3.5}$$

where ρ_i is the density of ice, ρ_0 is the surface density, k_0 and k_1 are temperature-dependent constants, h_{crit} is the depth that separates the upper and lower zones, and A is the accumulation rate in units of mass/area/time.

We use a surface density $\rho_0 = 350$ kg/m^3, which we assume to be constant through time. This value is based on the modern surface density at the SPC14 site (Max Stevens, pers. comm. July 2019). The bottom of the firn is constrained by a close-off density ρ_{co}, which we define as a function of temperature (Martinerie et al., 1992, 1994):

$$\rho_{co} = \left(\frac{1}{\rho_{ice}} + 6.95 \times 10^{-7} T - 4.3 \times 10^{-5}\right)^{-1}, \tag{3.6}$$

where ρ_{co} and ρ_{ice} are in units of kg/m^3 and T is in units of K. As temperature varies between -50 and -60°C, Equation 3.6 yields a small range of close-off densities between 831.5 and 836.4 kg/m^3.

We use the steady-state formulation of the HL model, which does not allow for variation with depth in temperature or accumulation rate. If either of these climate variables changes on short timescales, a transient formulation of the model would be required to reflect propagation through the firn column. Although our temperature and accumulation-rate inputs vary

through time, the timescale of those variations (*e.g.* 10 ka for an approximately 6°C change in temperature) is large enough that the steady-state formulation is acceptable. To test this, we ran our model with a transient formulation of the HL model and found no difference in the results of the forward model. Since the transient model is more computationally-expensive, we use the steady-state formulation.

3.4.2 Modeling Δage

We calculate the modeled Δage as the difference in the modeled age of the ice and the gas at the lock-in depth. We define the lock-in depth at a density of 10 kg m^{-3} less than the close-off density (Blunier and Schwander, 2000). The age of the ice at this depth is estimated directly from the depth-density profile. Within the HL framework, the age of the ice at the lock-in depth ρ_{LID} is calculated by:

$$\text{ice age}(\rho_{LID}) = \frac{1}{k_1 A^{0.5}} \ln\left(\frac{\rho_i - 0.55}{\rho_i - \rho_{LID}}\right) + \text{ice age}_{\text{upper firn}}(0.55), \tag{3.7}$$

with

$$\text{ice age}_{\text{upper firn}}(0.55) = \frac{1}{k_0 A} \ln\frac{\rho_i - \rho_0}{\rho_i - 0.55}.$$

We estimate the age of the gas at the lock-in depth using the parameterization in Buizert et al. (2013):

$$\text{gas age}(\rho_{LID}) = \frac{1}{1.367}\left(0.934 \times \frac{DCH^2}{D^0_{CO_2}} + 4.05\right), \tag{3.8}$$

where DCH is the diffusive column height, defined as the lock-in depth minus a 3 m convective zone. $D^0_{CO_2}$ is the free air diffusivity of CO_2 defined as (Schwander et al., 1988; Buizert et al., 2012):

$$D^0_{CO_2} = \frac{1013.25}{P} \times 1.81 \times 10^{-2} T^{1.81}, \tag{3.9}$$

with site atmospheric pressure P in hPa and absolute temperature T in Kelvin.

3.4.3 Modeling Firn Diffusion Length

We model diffusion length in the firn using the densification and isotope-diffusion model components. The combined effects on the isotope profile due to diffusion and firn densification can be described by Fick's second law:

$$\frac{\partial \delta}{\partial t} = D \frac{\partial^2 \delta}{\partial z^2} - \dot{\epsilon} z \frac{\partial \delta}{\partial z}, \tag{3.10}$$

where δ is the isotope ratio, D is the diffusivity coefficient, $\dot{\epsilon}$ is the vertical strain rate, and z is the vertical coordinate assuming an origin fixed on an arbitrary sinking layer of firn (Johnsen, 1977; Whillans and Grootes, 1985).

The diffusivity coefficient D_x of each isotope x depends on the temperature and density profile of the firn column, as shown in Johnsen et al. (2000):

$$D_x = \frac{m\, p\, D_x^{air}}{RT\, \alpha_x\, \tau} \left(\frac{1}{\rho} - \frac{1}{\rho_{ice}} \right), \tag{3.11}$$

where m is the molar weight of water, p is the saturation pressure over ice at temperature T and with gas constant R, D_x^{air} is the diffusivity of each isotope through air, α_x is the fractionation factor for each isotopic ratio in water vapor over ice, τ is the tortuosity of the firn, ρ is density of the firn, and ρ_{ice} is the density of ice. (Full derivation in Appendix A). We use the following values:

$$
\begin{aligned}
D^{air} &= 0.211 \times 10^{-4} \times \left(\frac{T}{273.15}\right)^{1.94} \times \frac{P_0}{P} \quad \text{(Johnsen et al., 2000)} \\
D^{air}_{\delta^{18}O} &= \frac{D^{air}}{1.0285} \qquad \text{(Johnsen et al., 2000)} \\
D^{air}_{\delta^{17}O} &= \frac{D^{air}}{1.01466} \qquad \text{(Luz and Barkan, 2010)} \\
D^{air}_{\delta D} &= \frac{D^{air}}{1.0251} \qquad \text{(Johnsen et al., 2000)} \\
\frac{1}{\tau} &= 1 - b \times \left(\frac{\rho}{\rho_{ice}}\right)^2 \quad \text{(Schwander et al., 1988; Johnsen et al., 2000)}
\end{aligned}
\tag{3.12}
$$

where T is temperature given in Kelvin, P is the atmospheric pressure given in atm compared to a reference pressure of $P_0 = 1$ atm, and the tortuosity parameter $b = 1.3$.

Solving Equation 3.10 for the isotope profile at a given depth z and time t, we can write (Gkinis et al., 2014):

$$\delta(z,t) = S(t)\frac{1}{\sigma\sqrt{2\pi}}\int_{-\infty}^{\infty}\delta(z,0)\exp\left(\frac{-(z-u)^2}{2\sigma^2}\right)du. \tag{3.13}$$

(Full derivation in Appendix A). The variable σ is the diffusion length and the factor $S(t)$ is the total thinning a layer has experienced due to ice flow from $t = 0$ to $t = t'$:

$$S(t') = \exp\left(\int_0^{t'}\dot{\epsilon}(t)dt\right). \tag{3.14}$$

Using the output from the firn-densification model, we calculate water-isotope diffusion through the estimated depth-density profile. First, the density profile is used to calculate the diffusivity of each isotope based on Equation 3.11. We then solve for the diffusion length σ_{firn} of a particular isotopologue in terms of its diffusivity D and the firn density ρ (Gkinis et al., 2014):

$$\sigma^2_{firn}(\rho) = \frac{1}{\rho^2}\int_{\rho_0}^{\rho} 2\rho^2\left(\frac{d\rho}{dt}\right)^{-1} D(\rho)d\rho, \tag{3.15}$$

where ρ_0 is the surface density and $\frac{d\rho}{dt}$ is the material derivative of the density. To calculate the diffusivity D, we use an atmospheric pressure of 0.7 atm (Severinghaus et al., 2001), which we assume to be constant through time (Fausto et al., 2018).

3.4.4 Modeling Vertical-Strain Effect on Diffusion Length

Cumulative vertical strain significantly thins layers in the ice, such that individual annual layers are often undetectable towards the bottom of an ice sheet. The thinning function is defined as the fractional amount of thinning that has occurred at a given depth in the ice sheet. We account for the effects of vertical strain on our modeled firn diffusion length σ_{firn} using a thinning function Γ. We model the diffusion length measured in the ice core as $\sigma_{icecore}$:

$$\sigma_{icecore} = \sigma_{firn} \times \Gamma. \tag{3.16}$$

3.4.5 Modeling Annual-Layer Thickness

Annual-layer thickness λ is modeled by the input accumulation rate A and the input thinning function Γ as:

$$\lambda = A \times \Gamma. \tag{3.17}$$

3.5 Inverse Approach

As in many geophysical problems, we have an inverse situation where the forward model G calculates the data parameters d as a function of unknown input parameters m:

$$G(m) = d. \tag{3.18}$$

Our forward model G is nonlinear and cannot be solved analytically to infer m. Instead, we use a Monte Carlo approach to test many instances of m through the forward model G to find the output d that best matches our observations d_{obs}.

We define the model space as a vector space with a dimension for each of the unknown input parameters; a particular point in the model space represents a specific set of input parameters m. The data space is defined similarly, where each data parameter in d represents a dimension, and our observations d_{obs} exist at a particular point in the data space. Because the data have measurement uncertainties, the "true" values in the data space may differ from d_{obs}.

Because we have three model parameters across 208 depth points (624 total unknown parameters), our problem spans a high dimensional model space, and an exhaustive search of all possible solutions m is not practical. We limit the number of instances of m to evaluate by using an importance-sampling algorithm. We use a Markov Chain Monte Carlo algorithm to combine *a priori* information about which solutions m are plausible for realistic ice-sheet conditions and information from our data sets. This algorithm efficiently explores the parameter space by favoring instances of m that are similar to those that have already produced good fits with the observations d_{obs}.

In this section we describe the theoretical framework and the practical implementation of the inverse approach we use. In general, the solution of this type of inverse problem depends on the formulation of the problem, including what information is included in the constraints and how the output is analyzed. We detail below each of the choices that we made in our approach.

3.5.1 Bayesian Framework

We use a statistical Bayesian framework to solve this inverse problem. Rather than seek a single best-fit solution, we consider the likelihood of different solutions based on probabil-

ity distributions within the parameter spaces of the data and the model. This framework combines *a priori* model parameter information with data measurement uncertainties. Unlike a regularization approach, such as Tikhonov regularization, a Bayesian approach does not require a subjective choice about how well the final set of solutions should fit the data (Tarantola, 1987; Steen-Larsen et al., 2010).

We characterize the *a priori* information describing the model inputs m as a probability distribution in the model space. This distribution, denoted as $\rho_m(m)$, represents the likelihood of solutions m based on data-independent prior knowledge about what values are realistic for that particular parameter (Mosegaard and Tarantola, 1995; Mosegaard and Sambridge, 2002). To produce the complete solution to the problem, the *a priori* information is combined with the likelihood function, which describes how well the output d from a given solution $G(m)$ matches our observations d_{obs}. The likelihood function $L(m)$ is defined as (Mosegaard and Tarantola, 1995):

$$L(m) = C_L \exp(-M(m)), \tag{3.19}$$

where C_L is a normalization constant and $M(m)$ is a misfit function that measures the deviation between d and d_{obs}.

The likelihood function $L(m)$ is combined with the *a priori* distribution $\rho_m(m)$ to define the *a posteriori* distribution $f(m)$ (Tarantola, 1987):

$$f(m) = C_f L(m)\rho_m(m). \tag{3.20}$$

The *a posteriori* distribution $f(m)$ contains all the information we have to constrain the inverse problem and thus represents its complete solution. The region of maximum values of $f(m)$ denote the most likely solutions to the problem. This distribution may be Gaussian-like

and simple to interpret, or may be multi-modal and require a more complex interpretation. We cannot produce this *a posteriori* distribution analytically, but we can sample its values at discrete points. For each solution m that we test in our forward model G, we calculate a discrete value of $f(m)$.

3.5.2 Sampling Strategy

Our sampling strategy uses an algorithm to determine which solutions m to test, with the goal of producing $f(m)$ after sufficient iterations through the model space (Mosegaard and Tarantola, 1995). The algorithm explores the model space by randomly stepping from one solution m_i to a neighbor m_j. In each iteration, the algorithm follows two stages, designed such that it asymptotically produces $f(m)$ (Mosegaard, 1998; Mosegaard and Sambridge, 2002).

First, an exploration stage defines how the algorithm selects a proposal for m_j given its starting place at m_i. The selection depends on how far in model space the algorithm is allowed to step in a single iteration. While the magnitude and direction of the step are determined randomly, the magnitude is scaled by a base step-size. The choice of base step-size balances the exploration of more of the model space (larger steps) with the exploration of regions that result in high values of $f(m)$ (smaller steps). In practice, we must tune the step size in order to strike this balance (*e.g.* Steen-Larsen et al. (2010)).

Second, an exploitation stage defines the transition probability that the random walk will accept the proposed step. If the proposed step is rejected, the random walk remains at the current solution m_i for an additional iteration. The simplest choice for the transition probability, which results in the highest acceptance probability for a given proposed step, is the Metropolis acceptance probability (Metropolis et al., 1953; Mosegaard, 1998; Mosegaard and Sambridge, 2002):

$$p_{accept} = min\left(1, \frac{f(m_j)}{f(m_i)}\right). \tag{3.21}$$

This formulation will always accept the proposed step to m_j if the *a posteriori* distribution is greater at that point ($f(m_j) > f(m_i)$), but may still accept the proposed step even if the *a posteriori* distribution is smaller at that point ($f(m_j) < f(m_i)$) by a probability proportional to $\frac{f(m_j)}{f(m_i)}$. This design prevents the algorithm from getting stuck at a local maximum of $f(m)$, while still favoring samples from regions of the model space with a relatively high value of $f(m)$.

After sufficient iterations, the sampling of this algorithm will converge on $f(m)$. The number of iterations required for convergence, the convergence time, depends on the base step-size chosen. Step size is tuned to minimize the number of iterations required. Related to the convergence time is the burn-in time, which refers to the number of iterations completed before the sampled values of $f(m)$ become relatively stationary. After this point, the algorithm continues to sample only highly likely solutions m. Prior work has found that after the burn-in time, the acceptance rate of the algorithm should be 25-50% (Gelman et al., 1996) in order to strike a balance between exploration (bigger steps) and efficiency (smaller steps).

3.5.3 Implementing our a priori information

Incorporating *a priori* information is important for limiting the scope of the problem. Disregarding prior knowledge often results in a solution that conflicts with what is known to be true about the system (Mosegaard, 1998). We incorporate *a priori* information about model parameters based on their modern values and our naive expectations of how they have varied through time. We include this *a priori* information by creating bounds on the allowable model space to explore. If the algorithm proposes a solution m_x that falls outside of our allowed model space, m_x is disregarded and another solution is proposed.

We also determine initial guesses m_1 based on *a priori* knowledge of a naive expectation for each parameter. Initiating the problem at what is judged to be a reasonable solution m_1 avoids unsatisfactory solutions (MacAyeal, 1993; Gudmundsson and Raymond, 2008).

The initial guess of temperature is derived from a step-function version of the water-isotope record. The initial guess for thinning function is the output of a Dansgaard and Johnsen (1969) (DJ) model. The DJ model is a 1-D analytical model that makes a simple assumption about the profile of horizontal ice-velocity through the depth of the ice sheet. The model assumes that above a kink height h, ice is flowing at a constant horizontal velocity, while below h, the horizontal velocity linearly decreases to zero at the base of the ice sheet. This simple model produces an approximation of the dynamics acceptable at many sites (Hammer et al., 1978). We use a kink height of $h = 0.1$ to simulate the flank flow at the SPC14 site. To produce an initial guess for accumulation rate, we divide the layer-thickness data by this thinning function and create a simplified step-function.

Each parameter is bounded based on naive expectations for its variability. For temperature, we bound the model space with an upper and lower scaling of the step-function version of the water-isotope record. We create an envelope for possible temperature histories from a conservative range of past temperature changes. Based on previous estimates of glacial-interglacial temperature change in Antarctica, we define allowable temperature histories as those that fall within a glacial-interglacial change of 5 to 15°C (Crowley and North, 1981; Jouzel et al., 2007). For accumulation rate, the allowed model-parameter range is an envelope about our initial guess defined as ± 0.02 meters year^{-1}. Based on the accumulation fluctuations in Lilien et al. (2018), this range is a reasonable limit on accumulation rate, while still allowing variation in the accumulation-rate parameter values tested in each m. For the thinning function, we do not provide further constraints on the allowed model space. Because the thinning function is directly related to accumulation rate and layer thickness, the constraints on those parameters effectively limit the allowed values for thinning function.

3.5.4 Sampling the a posteriori distribution

To sample and estimate the *a posteriori* distribution, we implement the theory described above. We initiate the problem with our initial guess m_1 for each parameter and begin

evaluating successive solutions from that point. Our sampling strategy uses Equation 3.21 and the associated ideas about sampling efficiency.

In the exploration stage of the algorithm, a perturbation is created to move from the current solution m_i to a proposed solution m_j. Rather than perturb only one parameter within m_i at a time, all 624 parameters (i.e. values at each depth point for temperature, accumulation rate, and thinning function) are perturbed in each iteration. This design improves the efficiency of the algorithm. Each perturbation is constructed with the same low-frequency, red-noise slope in its power spectral density as that of a comparison data set. The comparison data set for temperature is the water-isotope record, for accumulation rate is a destrained version of the annual-layer thicknesses, and for thinning function is a DJ-model output. Because in reality we expect temperature, accumulation rate, and thinning function to vary smoothly through time, each proposed perturbation must vary smoothly as well. To prevent spurious high-frequency noise from being introduced into the proposed solution m, we apply a low-pass filter to the perturbation. The Δage and diffusion-length data sets are inherently smooth because they integrate information over the depth of the firn column. To the temperature and accumulation-rate perturbations, we apply a lowpass filter at a 3000-year period, which corresponds to the maximum value of Δage. We apply a lowpass filter at a 10,000-year period to the thinning-function perturbations because we expect the thinning function to be even smoother.

In the exploitation stage, the algorithm determines whether to accept the proposal m_{i+1} by calculating and comparing the values of the *a posteriori* distribution at m_i and m_{i+1}. Equation 3.20 describes how the *a posteriori* distribution is calculated from the likelihood function $L(m)$ and the *a priori* distribution $\rho(m)$. Because we have already incorporated our prior knowledge directly into the model space bounds, we simply compare the value of the likelihood function evaluated at m_i and m_{i+1} (Mosegaard, 1998):

$$p_{accept} = min\left(1, \frac{L(m_{i+1})}{L(m_i)}\right). \tag{3.22}$$

We define the likelihood function, as in Equation 3.19, with a misfit function $M(m)$ defined as (Khan et al., 2000; Mosegaard and Sambridge, 2002):

$$M(m) = \sum_n \frac{\left| d^{(n)}(m) - d_{obs}^{(n)} \right|}{\sigma_n}, \tag{3.23}$$

where $d^{(n)}(m)$ denotes the modeled output, $d_{obs}^{(n)}$ the observation, and σ_n the standard deviation of the observation for the nth datum. This misfit function minimizes the importance of outliers, compared to a root-mean-square formulation.

We run the algorithm until we have 100,000 accepted samples of the *a posteriori* distribution. With an acceptance rate of 60-70%, this requires approximately 150,000 iterations in total. We find we need a higher acceptance rate than that recommended by the literature to optimize efficiency for this particular problem. The burn-in time is reached after approximately 10,000 iterations, and we consider solutions m only after this point. We repeat this process five times to account for any lasting impacts from early perturbations, combining all accepted solutions after the burn-in time to create the final set of results. Because only a small perturbation is made between iterations, successive iterations are correlated. Analysis of the *a posteriori* distribution requires a collection of statistically independent models, so we consider only a subset of all accepted models (Mosegaard, 1998; Dahl-Jensen et al., 1998). Through an autocorrelation analysis of the accepted models, we conclude that saving every 300th solution produces a statistically independent set. In total from 500,000 accepted solutions, 1500 solutions are included in our analysis of the *a posteriori* distribution.

3.6 A posteriori Results

Techniques for interpreting the *a posteriori* distribution depend on its shape. For the ideal inverse problem, the *a posteriori* distribution is often Gaussian. A Gaussian, or near-Gaussian, distribution can be interpreted through the mean and standard deviation of the suite of solutions m (Mosegaard and Tarantola, 2002).

3.6.1 Probability Distributions

To visualize the high-dimensional *a posteriori* distribution and determine whether a Gaussian approximation is appropriate, we plot probability distributions of each parameter. Rather than create separate probability distributions for each of the 624 parameters in our model space, we plot each probability distribution successively in a single figure to visualize the entire model space at once. The gray shading in the left three panels of Figure 3.6 shows successive probability distributions. A vertical slice through the grey shading in each plot represents the probability distribution for a particular parameter. How often a particular value is accepted for each parameter, for example an accumulation rate of 0.04 m yr^{-1} at 25ka, is represented by the shading, where darker shading denotes values that were accepted more often. The shape of the shading gives a sense of how the collection of solutions varies through the record, while the darkness of the shading gives a sense of the uncertainty. The solid magenta curves describe the initial guess for each parameter, and the dashed magenta curves describe the allowed model space (for temperature and accumulation rate). The model space bounds do not significantly limit the results.

The right three panels of Figure 3.6 illustrate how well the calculated data $d(m)$ matched with the observations d_{obs} throughout the collection of solutions. Since the uncertainty of the data is taken into account in the misfit (Equation 3.23), the probability distributions tend to lie within those bounds. This good match shows that the inverse approach is effectively incorporating the information from the data observations.

3.6.2 Sensitivity of Results

We evaluated the sensitivity of our results to different choices made throughout the formulation of the problem. Since we opted to keep the surface density ρ_0 in the firn-densification model constant through time, we tested the sensitivity of a change. We tested two alternate values of surface density $\rho_{surface}$ (450 kg/m^3 and 550 kg/m^3), and found no significant change

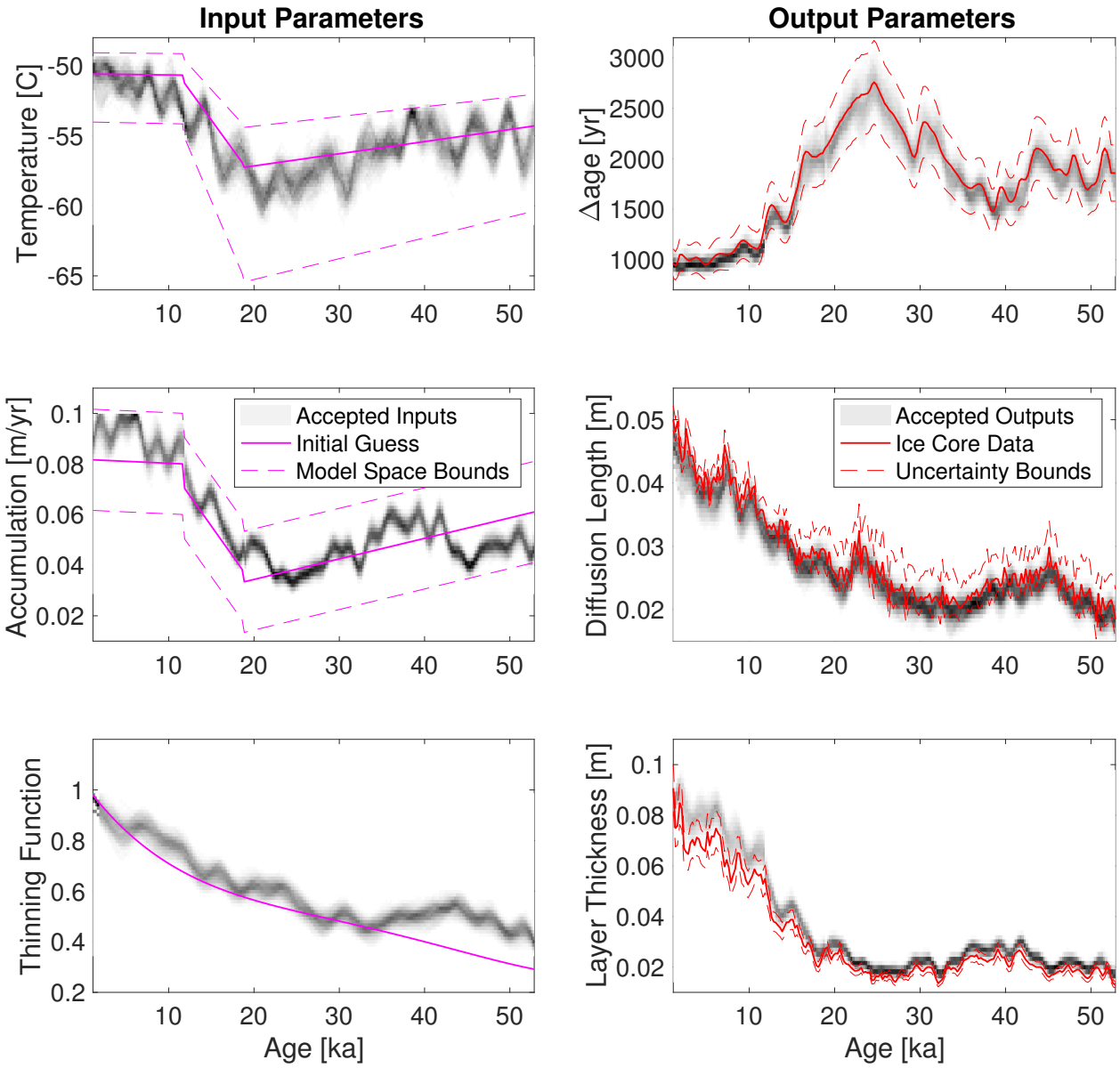

Figure 3.6: The *a posteriori* distribution result compared with *a priori* information. Vertical slices through the grey shading in each panel represent probability distributions for each parameter, where darker shading signifies greater likelihood. In the left three panels, solid magenta lines indicate the initial guess for each parameter and dashed lines mark the *a priori* bounds on the model space. In the right three panels, solid and dashed red lines show the ice-core data and its uncertainties.

in the results.

We also tested the sensitivity to different initial guesses for each parameter. We found that altering the initial guesses within the model space bounds did not significantly affect the final results. Additionally, including higher-frequency *a priori* information in our initial guesses did not significantly impact the results. We tested initial guesses of constant values for each of temperature, accumulation rate, and thinning function. These extremely simplified initial guesses produced a similar result as that from initial guesses that included the high-frequency variability of each comparison data set. However, the constant initial guesses required many more iterations to reach an equilibrium solution. As recommended in Gudmundsson and Raymond (2008), we opted for a middle ground that saves time by starting the initial guess close to the expected answer, but relies on the optimization to produce any high-frequency information.

To determine the extent to which each of our three data sets affects the results, we tested our approach by excluding different combinations of the data sets. We used the same inverse framework as before, but took into account only how well the output d matches the data observations d_{obs} for the data sets included in that test. Excluding all data sets evaluates the effect of the perturbation construction by resampling the *a priori* distribution (Mosegaard and Tarantola, 2002). Figure 3.7 illustrates that this null-test successfully recovers the prior, showing that no spurious information is produced by the sampling procedure. In each of the left three panels, the solution mean (blue curve) recovers the prior information and the standard deviation of the solutions (blue shading) fill the model space bounds.

Building up from this null-test, we tested two suites of three runs each to evaluate the sensitivity of results to each of the data sets. The first suite includes only one data set at a time, and the second suite includes two data sets at a time. The results from both suites are similar, and we show only the results from the second. Figure 3.8 shows the mean solution from each run of the second suite: excluding Δage (purple), excluding diffusion length (blue), and excluding layer thickness (green), compared alongside the full results

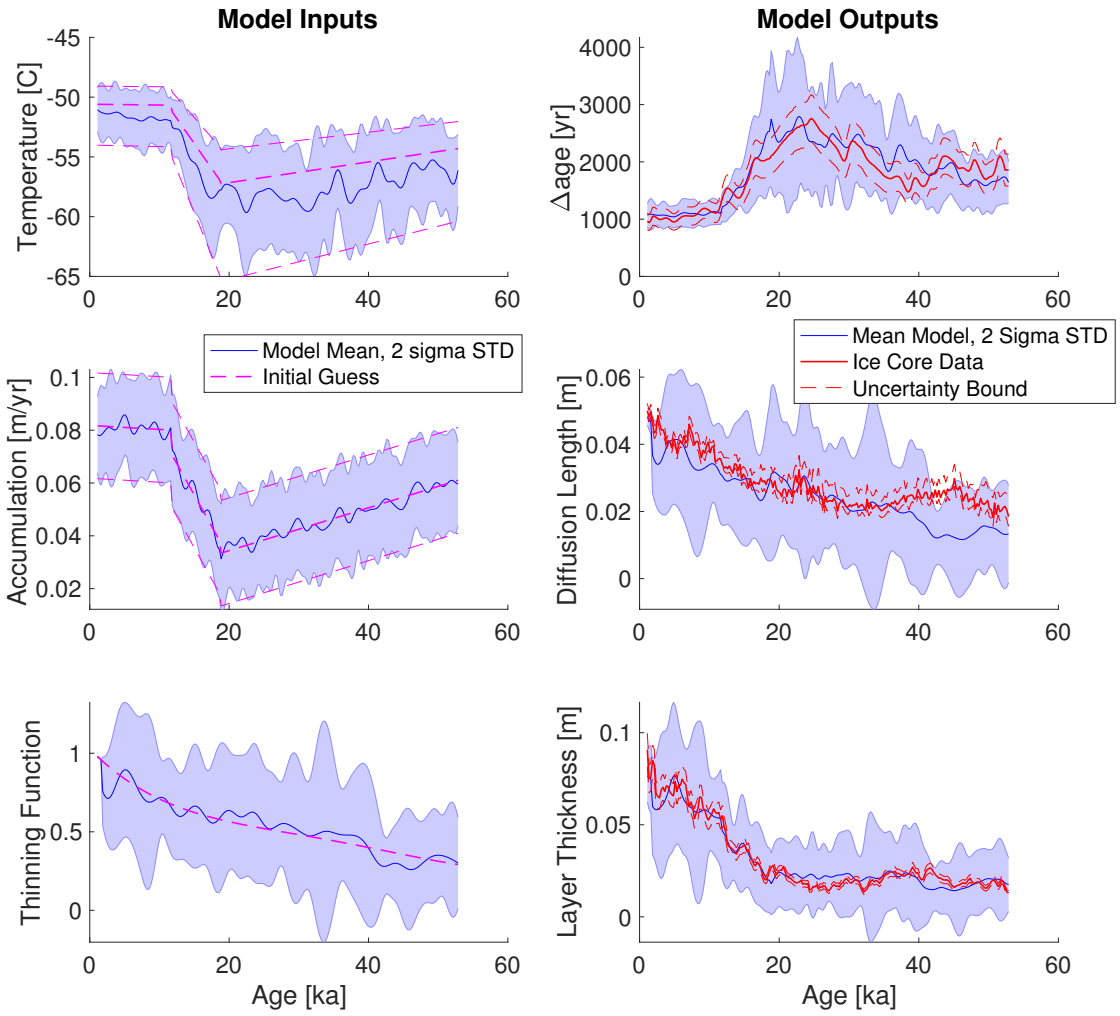

Figure 3.7: The results of the null-test to recover the *a priori* distribution are shown as the mean and standard deviation for each model and data parameter (blue curve and shading). For comparison the *a priori* information is shown in magenta and the ice-core data is shown in red.

including all parameters (black). The right three panels show the effect on the fit of the data parameters, producing, as expected, the worst fit to each data set when that information is excluded from the problem. The left three panels of Figure 3.8 show how the exclusion of

each data set impacts the mean of each set of solutions. The result for the thinning function suggests that, from 40 - 54 ka, the diffusion-length record pulls the thinning function to greater values (less thinning), while the layer thickness pulls the thinning function to smaller values (more thinning). Surprisingly, for accumulation rate, excluding layer thickness from the problem does not change the result significantly. The temperature reconstruction is not sensitive to any particular parameter from 0 - 20 ka, but beyond 20 ka, the temperature reconstruction is sensitive to all three datasets.

3.7 Discussion

We interpret the results of each reconstructed model-parameter individually. Because the probability distributions in Figure 3.6 are near-Gaussian, the mean and standard deviations of the solution set for each parameter are appropriate metrics in describing the total result. Our purpose in this section is to provide an example of how results from our method may be interpreted alongside comparison data sets. Comparing with other data sets illustrates what information has been gained from this reconstruction. In each case, we make recommendations for future work.

3.7.1 Accumulation-Rate and Thinning-Function Reconstructions

Because the results for accumulation rate and thinning function are fundamentally linked through Equation 3.17, we discuss them together. Figure 3.9 shows the mean and standard deviation of the reconstructed accumulation rate in the solid black curve and grey shading. The comparison data set plotted in dashed red is the destrained annual-layer thickness data, adjusted using the DJ-model output. While similarities in the high-frequency variability directly reflect the information in the annual-layer thickness data set, differences in the lower-frequency variability reflect new information gained from the optimization.

High-frequency variability in the accumulation-rate reconstruction is limited by our enforc-

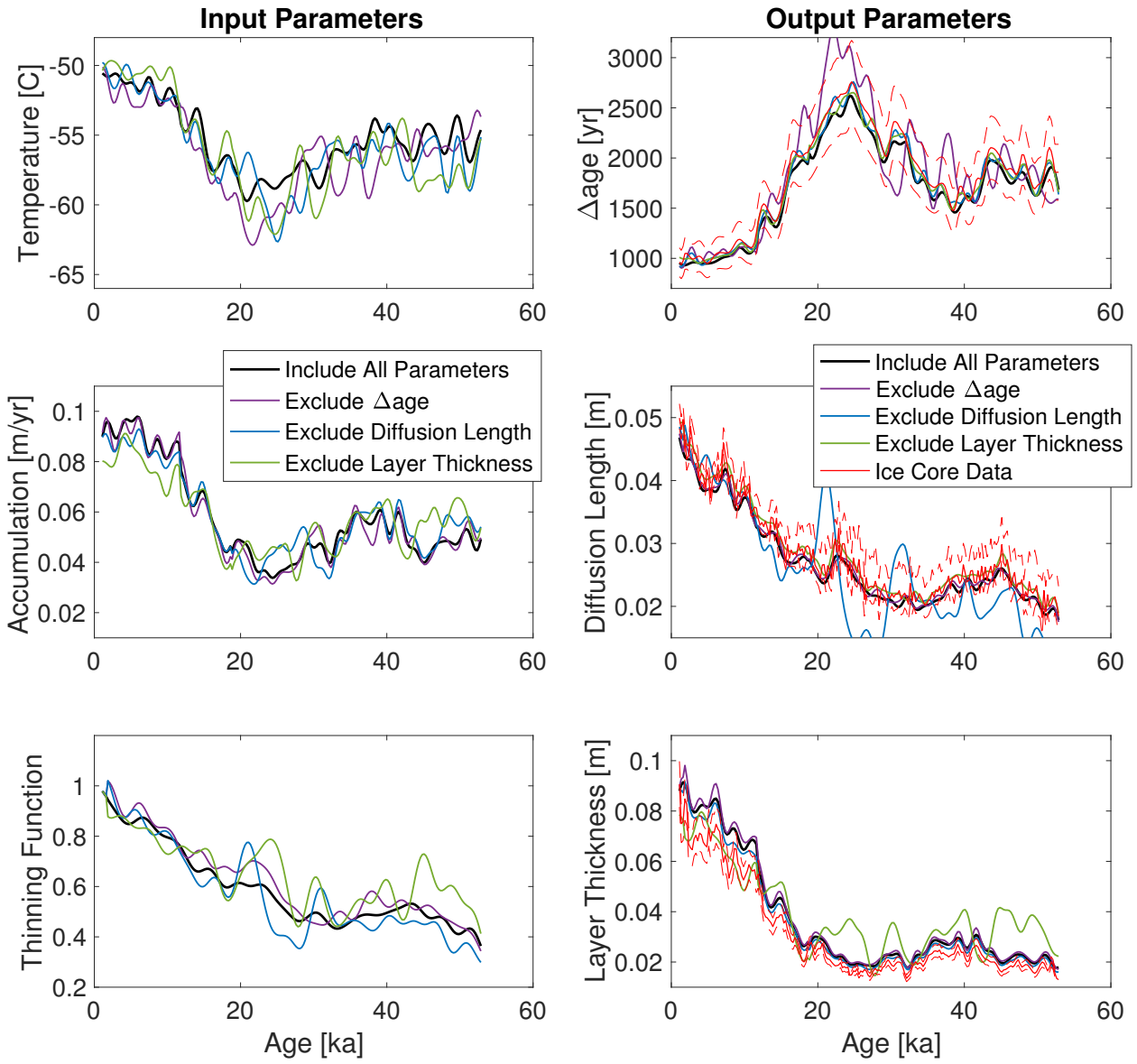

Figure 3.8: Analysis of the sensitivity of the *a posteriori* distribution to information in each data set. Each color shows the *a posteriori* distribution mean for a different sensitivity test. We compare the results when Δage is excluded (purple), when diffusion length is excluded (blue), when layer thickness is excluded (green), and when all data sets are included (black). Red curves in the right panel show ice-core data and uncertainties.

ing smooth perturbations at each iteration. Higher-frequency information can be obtained by destraining the high-resolution layer-thickness data set with the thinning-function recon-

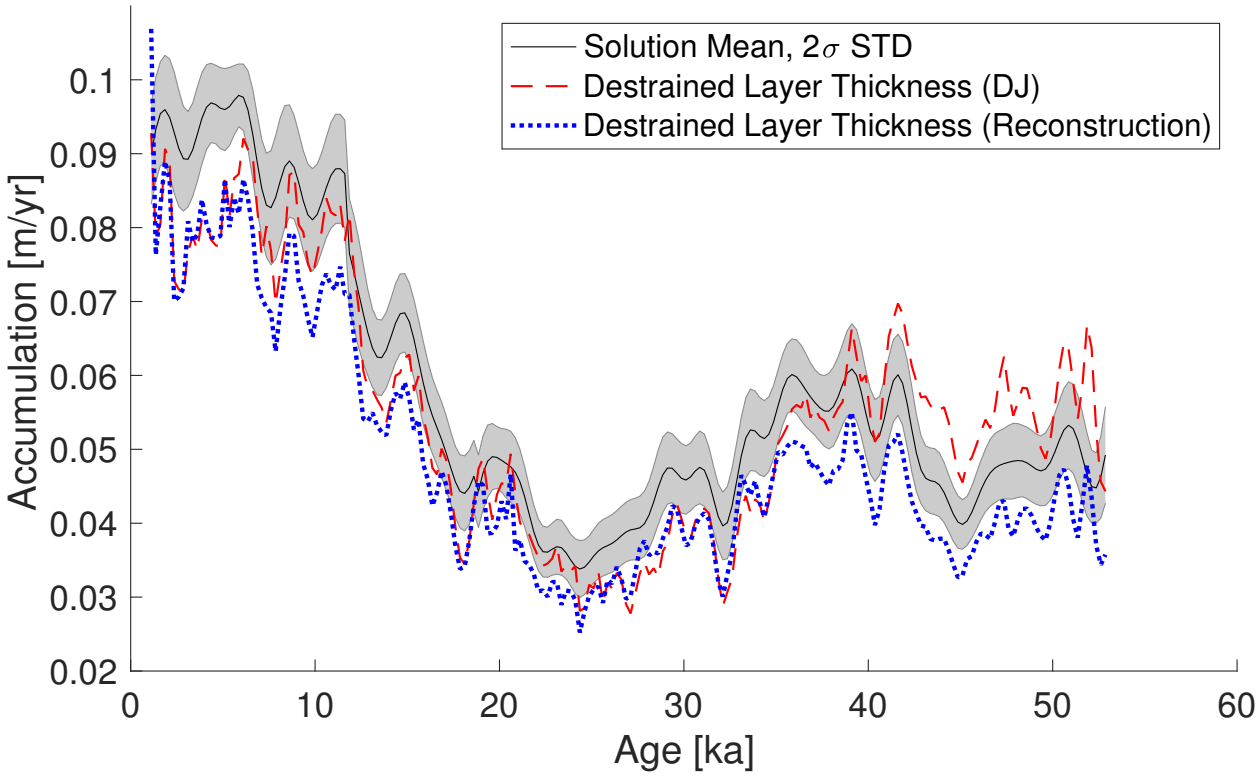

Figure 3.9: Accumulation-rate reconstruction and comparisons. The solid black curve and grey shading show the mean and standard deviation of the accumulation-rate parameters from the *a posteriori* distribution. For comparison, the dashed red curve shows the layer-thickness data destrained by a DJ-model output. Additionally, the dotted blue curve shows the layer-thickness data detrained by our reconstructed thinning function, providing an alternative, higher-frequency accumulation-rate reconstruction.

struction (dotted blue in Figure 3.9).

In Figure 3.10, we compare the thinning-function reconstruction with three independent thinning-function estimations. The solid black curve and grey shading show the mean and standard deviation for the reconstructed thinning function, the dashed red shows the 1-D DJ-model output, the dash-dot green shows the thinning output from a 2.5-D flow-band model, and the dotted blue shows an empirical calculations based on independent data from δ^{15}N measurements.

A 2.5-D flowband model (Koutnik et al., 2016) is used to calculate the thinning function based on geophysical measurements of bedrock topography, ice velocity, and internal layering upstream of the South Pole ice core (Lilien et al., 2018). The thinning is computed only for the Holocene (to 12 ka) because this is the duration for which the modern spatial pattern of accumulation could be correlated with the layer-thickness variations in the ice core (Lilien et al., 2018). The past flow direction is not well constrained for ages older than 12 ka (ice that originated beyond 65 km upstream). The flowband model is forced with the modern accumulation pattern and ice thickness and tuned using variations in the flowband width to approximately match the surface velocity. The key result is that undulations in the bedrock topography cause a reversal in the thinning function (at 7 ka in Figure 3.10), where deeper ice has thinned less than shallower ice. These reversals cannot be generated in a 1-D model. The reversal supports the magnitude of variations in our the reconstruction. Ongoing modeling is exploring the differences in total thinning (*e.g.* differences in the thinning-function value around 7 ka).

We also obtain an independent thinning function using measurements of the δ^{15}N of N_2 gas (Winski et al., 2019), following the methods described in Parrenin et al. (2012). The enrichment of δ^{15}N is a linear function of the original diffusive column height (DCH) of the firn due to the signal of gravitational fractionation recorded at the lock-in depth (Sowers et al., 1989; Buizert et al., 2013). To account for firn densification, the ice-equivalent DCH is estimated by an adjustment factor of 0.69 (Parrenin et al., 2012). To determine the thinning that has occurred in the ice sheet, the ice-equivalent DCH is compared to the Δdepth of the ice core, which reflects the thickness of ice in the ice core that originally comprised the firn column at the ice-sheet surface. The Δdepth is simply Δage multiplied by the depth-age relationship given by the ice timescale. The thinning function Γ is then given by (Parrenin et al., 2012):

$$\Gamma = \frac{\Delta\text{depth}}{0.69 \times \text{ice-equivalent DCH}} \tag{3.24}$$

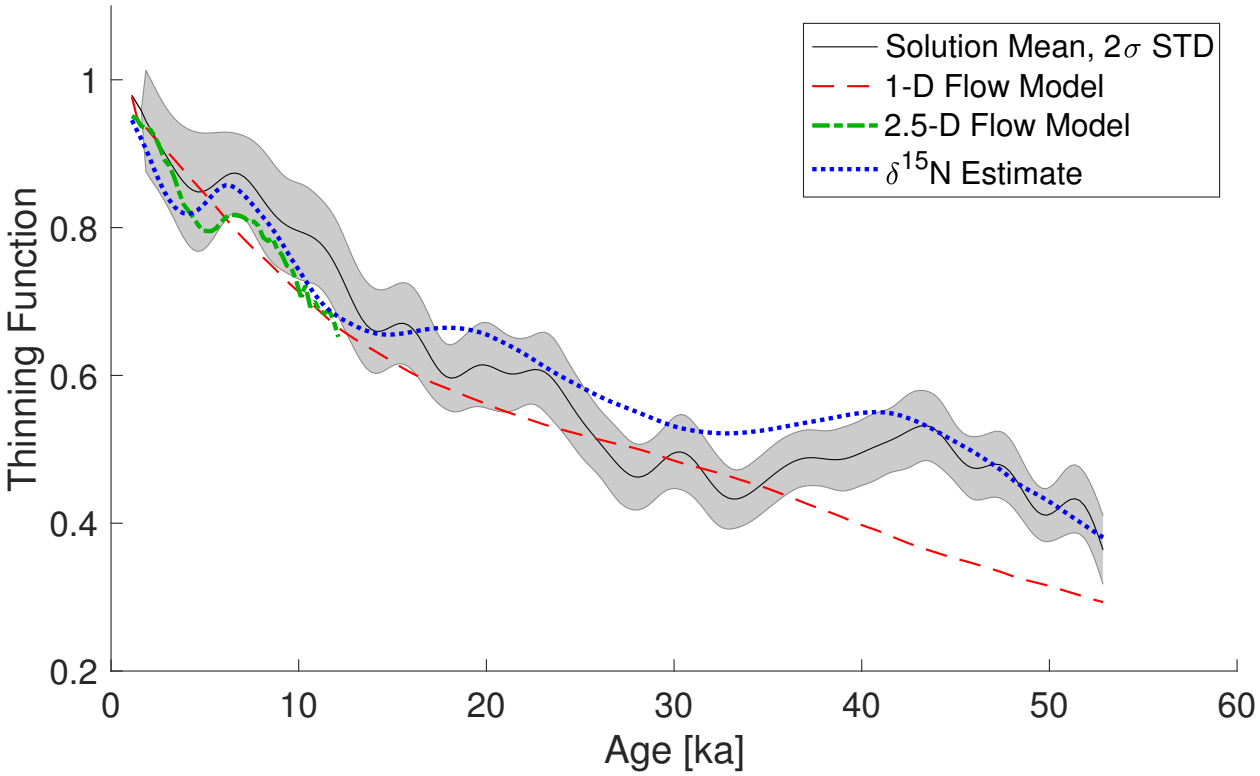

Figure 3.10: Thinning function reconstruction and comparisons. The solid black curve and grey shading show the mean and standard deviation of the thinning-function parameters from the *a posteriori* distribution. For comparison, the dashed red curve shows a DJ-model output, the dash-dot green shows the output from a 2.5-D flow-band model, and the dotted blue shows an independent estimate from δ^{15}N.

Our thinning function reconstruction and the independent δ^{15}N-based thinning function show significantly less thinning between 35 and 55 ka as compared to the 1-D DJ-model output. This decreased thinning at the bottom of the core can be explained by ice flowing up and over rises in the bedrock topography, suggesting topography plays an important role in shaping the thinning function.

In general, thinning functions lack small-scale variability because they integrate the total thinning experienced at a given depth. Since our reconstruction is allowed to find any best-fitting solutions, significant variability, large- and small-scale, appears in this result. Comparing the reconstruction with both an empirical thinning function and 2.5-D flow-band

model output gives two additional independent-estimates of the variability expected in the thinning function. The empirical estimate provides validation of some of the small-scale structure in the reconstruction, such as the sharp peak around 7 ka and the soft peak around 40 ka. The preliminary result from the 2.5-D flow-band model also suggests that this type of structure, particularly the peak at 7 ka, is possible given bedrock variations upstream of the SPC14 site. However, information about the bedrock topography farther upstream is required to extend that comparison through the entire depth of the core. This result is significant because it establishes the possibility of structure in the thinning function, particularly in the upper half of the core, which impacts the accumulation-rate reconstruction. Further work is needed to fully interpret upstream ice-flow at SPC14 and its impact on the thinning function.

3.7.2 Temperature Reconstruction

We plot the mean (solid black) and standard deviation (grey) of the temperature result in Figure 3.11. For comparison, we plot a scaled version of the sea-water-corrected water-isotope record (Bintaja and van de Wal, 2008). The dashed red curve uses a scaling of $0.8‰°C^{-1}$, the modern surface isotope-temperature relationship at the site (Fudge et al., 2019). We do not necessarily expect this slope to be valid through time, but use it here as an illustrative comparison with the reconstruction.

The temperature reconstruction and the water isotopes are well-correlated through the record. Each show a gradually-cooling glacial period with variability of roughly 2 - 4°C, a steep glacial-interglacial transition, and a warmer Holocene. Prominent events in other Antarctic ice cores are present in both records, including the ACR around 14 ka and the AIM2 event around 23.5 ka (Stenni et al., 2010, 2011; Buizert et al., 2015). The timing of the LGM around 20 ka also matches well with other Antarctic water-isotope records.

The correlation between the temperature reconstruction and the water isotopes decreases

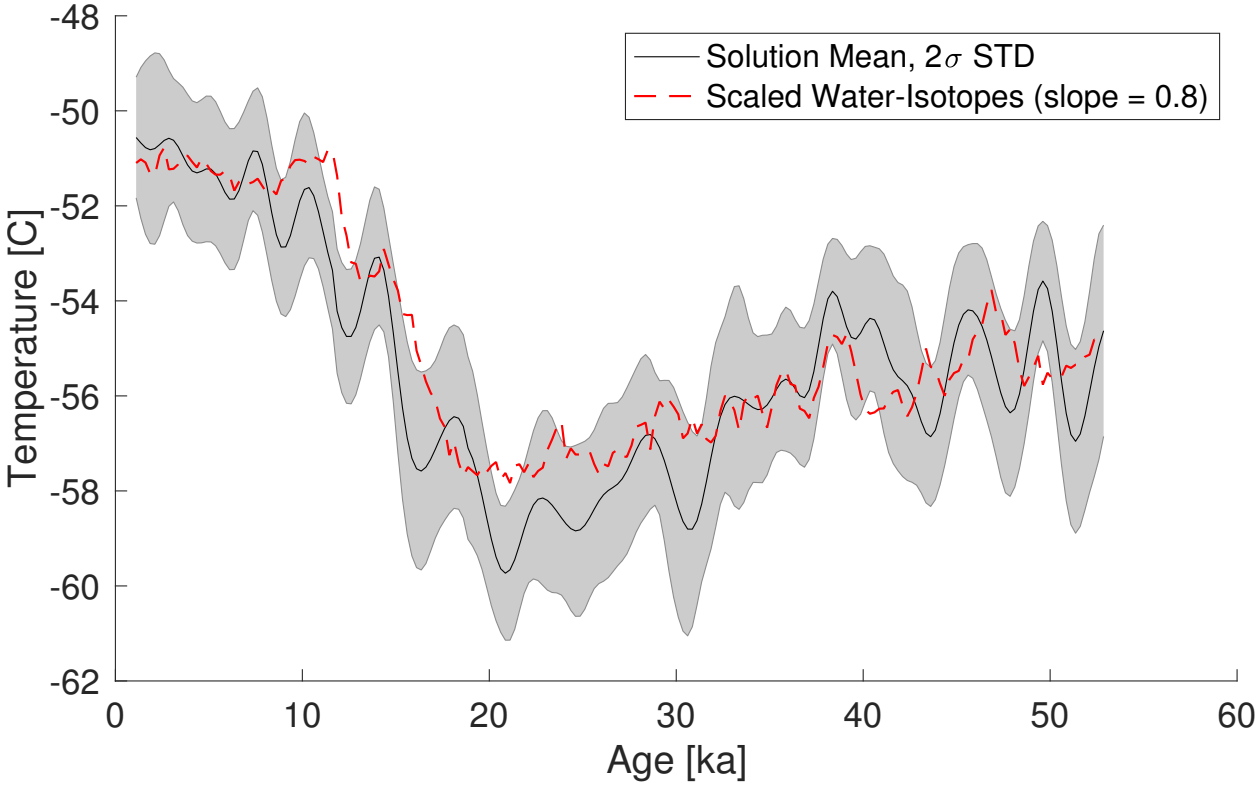

Figure 3.11: Temperature reconstruction and comparisons. The solid black curve and grey shading show the mean and standard deviation of the temperature parameters from the *a posteriori* distribution. For comparison, the dashed-red curve shows the water-isotope record scaled by the modern surface-slope at the site, 0.8 ‰°C^{-1}. This reconstruction follows the conventional approach to isotope-temperature reconstructions for East Antarctic ice cores.

significantly prior to 40 ka. We suspect this is due to how uncertainty in the ice-core timescale has different effects the water isotopes and the derived data sets used in the reconstruction. A small shift in the timescale of either record would match up similar variability in the records. Future work is exploring the impacts on the reconstruction of varying the timescale within its uncertainty bounds.

3.7.3 South-Pole-Site Temperature Reconstruction

Because SPC14 was drilled far from the divide, deeper ice in the core originated at the surface increasingly farther upstream. Since any information recorded in the core contains information about conditions upstream, appropriate corrections are required to determine a history for the South Pole site itself (Dahl-Jensen et al., 1997; Huybrechts et al., 2007; Neumann et al., 2008). In the temperature reconstruction, we corrected for this advection of ice by making an adjustment for the assumed elevation change upstream (Fudge et al., 2019). The ice flows down slope from higher and colder elevations. Assuming relatively stable ice-sheet surface-topography through time, we use a lapse rate of 10°C km^{-1} to calculate a correction to the temperature reconstruction for the core. The magnitude of this correction grows with depth in the core and results in a roughly 1°C warming correction in the glacial period. The solid black curve and grey shading in Figure 3.12 shows the advection-corrected temperature reconstruction.

We use our temperature reconstruction to examine the isotope-temperature relationship by calibrating the relationship at each depth point in the reconstruction. To compare the water-isotope measurements with the advection-corrected temperature reconstruction, we correct the $\delta^{18}O$ record for variations in sea water based on Bintaja and van de Wal (2008) and for advection based on upstream surface water-isotope measurements (Fudge et al., 2019). We calibrate the isotope-temperature relationship first with a constant slope through time (dashed-red curve in Figure 3.12). Unlike the red curve in Figure 3.11, this scaling makes use of the independent temperature information gained from our reconstruction to calibrate the relationship back in time. The single-slope calibration yields a relationship of 0.99 ‰°C^{-1}, which provides a better fit to the reconstruction than the modern surface relationship of 0.8 ‰°C^{-1} used in Figure 3.11.

The match between isotopes and the temperature reconstruction can be further improved by allowing the relationship to vary. We allow the relationship to vary across two different

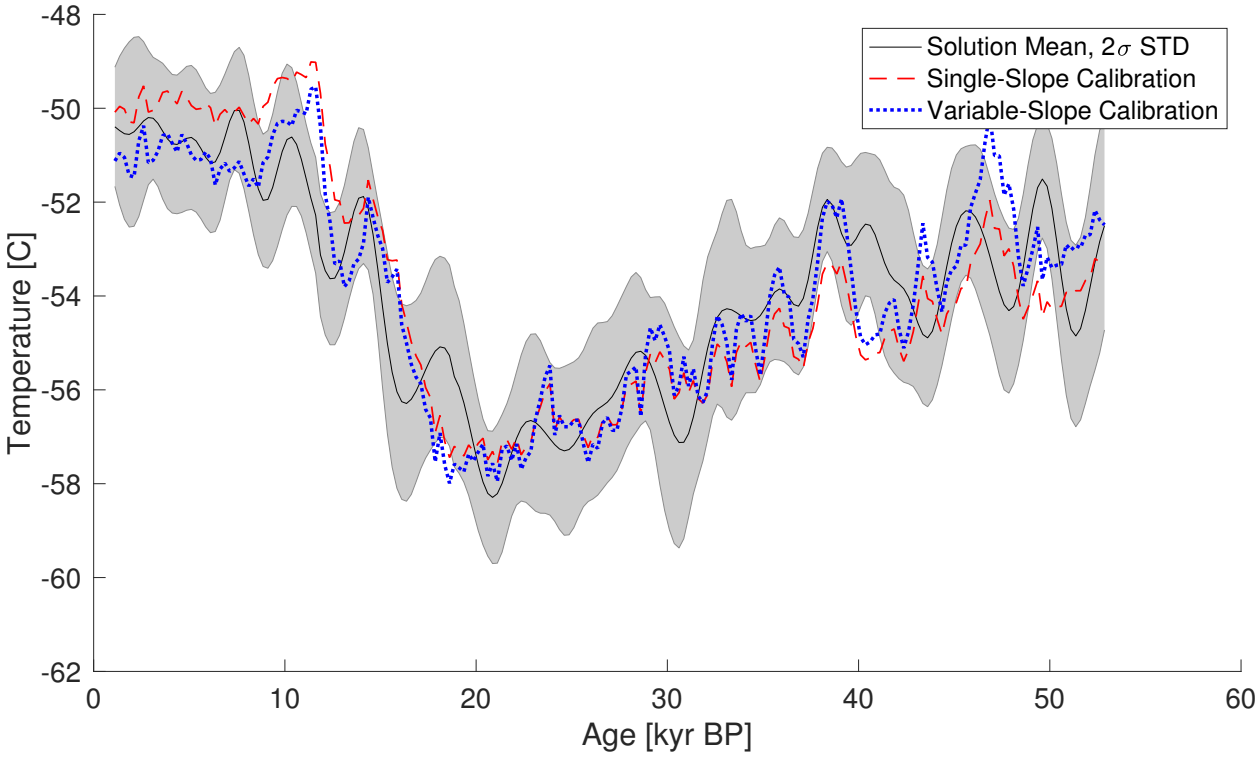

Figure 3.12: Reconstructions of the South Pole site temperature. The solid black curve and grey shading show our temperature reconstruction. Dashed-red curve shows the scaled water-isotope record as calibrated against the reconstruction with a constant relationship. Dotted-blue curve shows the scaled water-isotope record calibrated with a relationship allowed to vary across different time domains and across different frequencies of variability. All three reconstructions are corrected for advection of ice from a colder and isotopically-depleted origin upstream.

time periods and across different frequencies of variability. We separate the temperature and isotope records into glacial (20 - 54 ka) and post-glacial (0 - 20 ka) time periods and use a Butterworth filter to separate the signal into frequency ranges above and below a period of 10 ka, yielding the four different relationships listed in Table 3.1. The combination of each of these slopes is shown in the dotted-blue curve in Figure 3.12, producing a better fit to the temperature reconstruction compared to the single-slope calibration in red. While previous work in central Antarctica has assumed that the isotope-temperature relationship remains constant through time (Jouzel et al., 2003), these results suggest that it can vary significantly

Table 3.1: Slopes calculated by calibration of water isotopes with the temperature reconstruction. Four different slopes were calibrated by separating the records into two different time periods (glacial and post-glacial) and by separating the high- and low-frequency variations of the signal. The time periods are separated before and after 20 ka. The high- and low-frequency ranges are separated above and below a period of 10 ka.

Time Period	**Frequency Range**	**Calibrated Slope**
Glacial	High	0.67 ‰°C^{-1}
Glacial	Low	0.73 ‰°C^{-1}
Post-Glacial	High	0.70 ‰°C^{-1}
Post-Glacial	Low	1.13 ‰°C^{-1}

through time at a site such as the South Pole. A variable isotope-temperature relationship has significant implications for estimating past temperature from ice-core water-isotope data.

The importance of a variable isotope-temperature relationship is apparent when examining the magnitude of glacial-interglacial temperature change, a common target for determining climate sensitivity from the paleoclimate record. Our reconstruction finds a temperature change of approximately 6.2°C, as defined by the difference in the mean temperatures at intervals of 0.5 - 2.5 ka and 18 - 21.4 ka, in good agreement with recent work using δ^{15}N (Buizert et al., in prep.). This result suggests less cooling than has been found from linear-scaling of water-isotope records elsewhere in East Antarctica (Genthon et al., 1987; Jouzel et al., 2003; Stenni et al., 2003, 2010). These other estimates assume that the isotope-temperature relationship stays constant through time, which results in a colder LGM. This analysis shows that a variable isotope-temperature relationship results in a smaller temperature change. This smaller glacial-interglacial change is consistent with GCM results (Masson-Delmotte et al., 2013), resolving a longstanding discrepancy between temperature estimates from climate models and ice-core data (Crowley and North, 1991; Masson-Delmotte et al., 2006).

In future work, both our reconstruction and the scaled water-isotopes can be used as tem-

perature estimates for SPC14. Although we point out that water isotopes do not perfectly reflect changes in temperature, they contain higher-frequency information than our reconstruction, which is fundamentally limited by the lower-resolution Δage and diffusion-length data sets. In future studies, the choice to use one of these reconstructions over the other will depend on the purpose and goals of that work.

3.8 Conclusion

We have used a Monte Carlo inverse approach to combine information from three different data sets from the South Pole ice core. Any single data set from an ice core provides only a limited amount of information for interpretation. Using multiple data sets together creates stronger constraints on the climate and glaciological records inferred from the ice core. We have shown that combining Δage, diffusion length, and annual-layer thickness data sets can robustly constrain reconstructions of temperature, accumulation rate, and thinning function. The temperature reconstruction suggests a variable isotope-temperature relationship through time, as well as a smaller glacial-interglacial temperature change than previously estimated elsewhere in East Antarctica. The reconstructions of accumulation rate and thinning function imply some small-scale variation in thinning as well as less total thinning at depth as compared to the output of a 1-D ice-flow model. In the future, this Monte Carlo approach could be modified to constrain reconstructions using data sets from new or existing ice-core records.

3.9 Acknowledgments

The work in this chapter was made possible by access to multiple data sets from the South Pole ice core. In addition to those already published and cited within, we would like to thank Jenna Epifanio and Ed Brook for their work creating the SPC14 gas timescale, soon to be published. We would like to thank Jeff Severinghaus for the complete δ^{15}N data set,

only part of which was published in Winski et al. (2019). Finally, we would like to thank Jim White and the entire INSTAAR lab for helping to create the SPC14 water-isotope measurements. In addition to access to SPC14 data, we would like to thank Max Stevens for discussions about firn modeling and Daniel Shapero for discussions about inverse theory and methodology.

BIBLIOGRAPHY

Alley, R. B., Shuman, C. A., Meese, D. A., Gow, A. J., Taylor, K. C., Cuffey, K. M., Spinelli, G. et al. (1997). Visualstratigraphic dating of the GISP2 ice core: Basis, reproducibility, and application. *Journal of Geophysical Research: Oceans*, 102(C12), 26367-26381.

Arthern, R. J., Vaughan, D. G., Rankin, A. M., Mulvaney, R., and Thomas, E. R. (2010). In situ measurements of Antarctic snow compaction compared with predictions of models. *Journal of Geophysical Research: Earth Surface*, 115(F3).

Barnola, J. M., Pimienta, P., Raynaud, D., and Korotkevich, Y. S. (1991). CO2climate relationship as deduced from the Vostok ice core: A reexamination based on new measurements and on a reevaluation of the air dating. *Tellus B*, 43(2), 83-90.

Bintanja, R., and Van de Wal, R. S. W. (2008). North American ice-sheet dynamics and the onset of 100,000-year glacial cycles. *Nature*, 454(7206), 869.

Blunier, T., and Schwander, J. (2000). Gas enclosure in ice: age difference and fractionation. *Physics of Ice Core Records* 307-326. Hokkaido University Press.

Buizert, C., Martinerie, P., Petrenko, V. V., Severinghaus, J. P., Trudinger, C. M., Witrant, E., Steele, L. P. et al. (2012). Gas transport in firn: multiple-tracer characterisation and model intercomparison for NEEM, Northern Greenland. *Atmospheric Chemistry and Physics*, 12(9), 4259-4277.

Buizert, C., Sowers, T., and Blunier, T. (2013). Assessment of diffusive isotopic fractionation in polar firn, and application to ice core trace gas records. *Earth and Planetary Science Letters*, 361, 110-119.

Buizert, C., Cuffey, K. M., Severinghaus, J. P., Baggenstos, D., Fudge, T. J., Steig, E. J., Sowers, T. A. et al. (2015). The WAIS divide deep ice core WD2014 chronologyPart 1: methane synchronization (6831 kaBP) and the gas ageice age difference. *Climate of the Past*, 11(2).

Buizert, C., et al. in prep. Strongly reduced estimates of Antarctic cooling during the Last Glacial Maximum. Unpublished manuscript.

Casey, K. A., Fudge, T. J., Neumann, T. A., Steig, E. J., Cavitte, M. G. P., and Blankenship, D. D. (2014). The 1500 m South Pole ice core: Recovering a 40 ka environmental record. *Annals of Glaciology*, 55(68), 137–146.

Crowley, T. J., and G. R. North (1991). *Paleoclimatology*. New York, NY: Oxford University Press.

Cuffey, K. M., Clow, G. D., Alley, R. B., Stuiver, M., Waddington, E. D., and Saltus, R. W. (1995). Large arctic temperature change at the Wisconsin-Holocene glacial transition. *Science*, 270(5235), 455-458.

Cuffey, K. M., and Clow, G. D. (1997). Temperature, accumulation, and ice sheet elevation in central Greenland through the last deglacial transition. *Journal of Geophysical Research: Oceans*, 102(C12), 26383-26396.

Cuffey, K. M. and Steig, E. J. (1998). Isotopic diffusion in polar firn: Implications for interpretation of seasonal climate parameters in ice-core records, with emphasis on central Greenland. *Journal of Glaciology*, 44(147), 273–284.

Cuffey, K. M., Clow, G. D., Steig, E. J., Buizert, C., Fudge, T. J., Koutnik, M., Severinghaus, J. P. et al. (2016). Deglacial temperature history of West Antarctica. *Proceedings of the National Academy of Sciences*, 113(50), 14249-14254.

Dahl-Jensen, D., Thorsteinsson, T., Alley, R., and Shoji, H. (1997). Flow properties of the ice from the Greenland Ice Core Project ice core: the reason for folds?. *Journal of Geophysical Research: Oceans*, 102(C12), 26831-26840.

Dahl-Jensen, D., Mosegaard, K., Gundestrup, N., Clow, G. D., Johnsen, S. J., Hansen, A. W., and Balling, N. (1998). Past temperatures directly from the Greenland ice sheet. *Science*, 282(5387), 268-271.

Dansgaard, W. (1954). The ^{18}O-abundance in fresh water. *Geochimica et Cosmochimica Acta*, 6(5-6), 241–260.

Dansgaard, W. (1964). Stable isotopes in precipitation. *Tellus B*, 16(4), 436–468.

Dansgaard, W., and Johnsen, S. J. (1969). A flow model and a time scale for the ice core from Camp Century, Greenland. *Journal of Glaciology*, 8(53), 215-223.

Epifanio et al. in prep. The SP19 chronology for the South Pole Ice Core Part 2: Gas age scale, Delta-age, and smoothing of atmospheric records. Unpublished manuscript.

Fausto, R. S., Box, J. E., Vandecrux, B. R. M., van As, D., Steffen, K., MacFerrin, M. J., Charalampidis, C. et al. (2018). A snow density dataset for improving surface boundary conditions in Greenland ice sheet firn modeling. *Frontiers in Earth Science*, 6.

Fudge, T. J., Waddington, E. D., Conway, H., Lundin, J. M. D., and Taylor, K. (2014). Interpolation methods for Antarctic ice-core timescales: application to Byrd, Siple Dome and Law Dome ice cores. *Climate of the Past*, 10(3), 1195-1209.

Fudge, T. J., Markle, B. R., Cuffey, K. M., Buizert, C., Taylor, K. C., Steig, E. J., Koutnik, M. et al. (2016). Variable relationship between accumulation and temperature in West Antarctica for the past 31,000 years. *Geophysical Research Letters*, 43(8), 3795-3803.

Fudge, T.J., D.A. Lilien, M. Koutnik, H. Conway, C.M. Stevens, E.D. Waddington, E.J.

Steig, and A.J. Schauer (2019). Advection (non-climate) impact on the South Pole Ice Core. *Climate of the Past Discussions* doi:10.5194/cp-2019-66.

Gelman, A., Roberts, G. O., and Gilks, W. R. (1996). Efficient Metropolis jumping rules. *Bayesian Statistics*, 5(599-608), 42.

Genthon, G., Barnola, J. M., Raynaud, D., Lorius, C., Jouzel, J., Barkov, N. I., Kotlyakov, V. M. et al. (1987). Vostok ice core: climatic response to CO2 and orbital forcing changes over the last climatic cycle. *Nature*, 329(6138), 414.

Gkinis, V., Simonsen, S. B., Buchardt, S. L., White, J. W. C. and Vinther, B. M. (2014). Water isotope diffusion rates from the NorthGRIP ice core for the last 16,000 years - glaciological and paleoclimatic implications. *Earth and Planetary Science Letters*, 405, 132–141.

Goujon, C., Barnola, J. M., and Ritz, C. (2003). Modeling the densification of polar firn including heat diffusion: Application to closeoff characteristics and gas isotopic fractionation for Antarctica and Greenland sites. *Journal of Geophysical Research: Atmospheres*, 108(D24).

Gudmundsson, G. H., and Raymond, M. (2008). On the limit to resolution and information on basal properties obtainable from surface data on ice streams. *The Cryosphere*, 2(3), 413-445.

Hammer, C. U., Clausen, H. B., Dansgaard, W., Gundestrup, N., Johnsen, S. J., and Reeh, N. (1978). Dating of Greenland ice cores by flow models, isotopes, volcanic debris, and continental dust. *Journal of Glaciology*, 20(82), 3-26.

Herron, M. M., and Langway, C. C. (1980). Firn densification: an empirical model. *Journal of Glaciology*, 25(93), 373-385.

Huybrechts, P., Rybak, O., Pattyn, F., Ruth, U., and Steinhage, D. (2007). Ice thinning, upstream advection, and non-climatic biases for the upper 89% of the EDML ice core from a nested model of the Antarctic ice sheet. *Climate of the Past*, 3(3), pp.693-727.

Johnsen, S. J. (1977). Stable isotope homogenization of polar firn and ice. *Isotopes and Impurities in Snow and Ice*, 201–219.

Johnsen, S. J., Clausen, H. B., Cuffey, K. M., Hoffmann, G., Schwander, J. and Creyts, T. (2000). Diffusion of stable isotopes in polar firn and ice: The isotope effect in firn diffusion. *Physics of Ice Core Records*, 121–140.

Jones, T. R., Cuffey, K. M., White, J. W. C., Steig, E. J., Buizert, C., Markle, B. R., McConnell, J. R. and Sigl, M. (2017a). Water isotope diffusion in the WAIS Divide ice core during the Holocene and last glacial. *Journal of Geophysical Research: Earth Surface*, 122, 290-309.

Jones, T. R., White, J. W. C., Steig, E. J., Vaughn, B. H., Morris, V., Gkinis, V., Markle, B. R. and Schoenemann, S. W. (2017b). Improved methodologies for continuous flow analysis of stable water isotopes in ice cores. *Atmospheric Measurement Techniques*, 10, 617-632.

Jones et al., in prep. Seasonality of Accumulation. Unpublished manuscript.

Jouzel, J., Barkov, N. I., Barnola, J. M., Bender, M., Chappellaz, J., Genthon, C., Raynaud, D. et al. (1993). Extending the Vostok ice-core record of palaeoclimate to the penultimate glacial period. *Nature*, 364(6436), 407.

Jouzel, J., Alley, R. B., Cuffey, K. M., Dansgaard, W., Grootes, P., Hoffmann, G., Stievenard, M. et al. (1997). Validity of the temperature reconstruction from water isotopes in ice cores. *Journal of Geophysical Research: Oceans*, 102(C12), 26471-26487.

Jouzel, J., Vimeux, F., Caillon, N., Delaygue, G., Hoffmann, G., MassonDelmotte, V., and Parrenin, F. (2003). Magnitude of isotope/temperature scaling for interpretation of central Antarctic ice cores. *Journal of Geophysical Research: Atmospheres*, 108(D12).

Jouzel, J., Masson-Delmotte, V., Cattani, O., Dreyfus, G., Falourd, S., Hoffmann, G., Fischer, H. et al. (2007). Orbital and millennial Antarctic climate variability over the past 800,000 years. *Science*, 317(5839), 793-796.

Kahle, E. C., Holme, C., Jones, T. R., Gkinis, V., and Steig, E. J. (2018). A Generalized Approach to Estimating Diffusion Length of Stable Water Isotopes From IceCore Data. *Journal of Geophysical Research: Earth Surface*, 123(10), 2377-2391.

Khan, A., Mosegaard, K., and Rasmussen, K. L. (2000). A new seismic velocity model for the Moon from a Monte Carlo inversion of the Apollo lunar seismic data. *Geophysical Research Letters*, 27(11), 1591-1594.

Koutnik, M. R., Fudge, T. J., Conway, H., Waddington, E. D., Neumann, T. A., Cuffey, K. M., Taylor, K. C., et al. (2016). Holocene accumulation and ice flow near the West Antarctic Ice Sheet Divide ice core site. *Journal of Geophysical Research: Earth Surface*, 121(5), 907-924.

Lazzara, M. A., Keller, L. M., Markle, T., and Gallagher, J. (2012). Fifty-year Amundsen-Scott South Pole station surface climatology. *Atmospheric Research*, 118, 240-259.

Lilien, D. A., Fudge, T. J., Koutnik, M. R., Conway, H., Osterberg, E. C., Ferris, D. G., and Stevens, C. M. et al. (2018). Holocene IceFlow Speedup in the Vicinity of the South Pole. *Geophysical Research Letters*, 45(13), 6557-6565.

Lorius, C., Jouzel, J., Raynaud, D., Hansen, J., and Le Treut, H. (1990). The ice-core record: climate sensitivity and future greenhouse warming. *Nature*, 347(6289), 139.

Luz, B., and Barkan, E. (2010). Variations of 17O/16O and 18O/16O in meteoric waters. *Geochimica et Cosmochimica Acta*, 74(22), 6276-6286.

MacAyeal, D. R. (1993). Binge/purge oscillations of the Laurentide ice sheet as a cause of the North Atlantic's Heinrich events. *Paleoceanography*, 8(6), 775-784.

Martinerie, P., Raynaud, D., Etheridge, D. M., Barnola, J. M., and Mazaudier, D. (1992). Physical and climatic parameters which influence the air content in polar ice. *Earth and Planetary Science Letters*, 112(1-4), 1-13.

Martinerie, P., Lipenkov, V. Y., Raynaud, D., Chappellaz, J., Barkov, N. I., and Lorius, C. (1994). Air content paleo record in the Vostok ice core (Antarctica): A mixed record of climatic and glaciological parameters. *Journal of Geophysical Research: Atmospheres*, 99(D5), 10565-10576.

Masson-Delmotte, V., M. Schulz, A. Abe-Ouchi, J. Beer, A. Ganopolski, J.F. Gonzalez Rouco, E. Jansen, K. Lambeck, J. Luterbacher, T. Naish, T. Osborn, B. Otto-Bliesner, T. Quinn, R. Ramesh, M. Rojas, X. Shao and A. Timmermann (2013). Information from Paleoclimate Archives. In: Climate Change 2013: The Physical Science Basis. Contribution of Working Group I to the Fifth Assessment Report of the Intergovernmental Panel on Climate Change [Stocker, T.F., D. Qin, G.-K. Plattner, M. Tignor, S.K. Allen, J. Boschung, A. Nauels, Y. Xia, V. Bex and P.M. Midgley (eds.)]. *Cambridge University Press*, Cambridge, United Kingdom and New York, NY, USA.

Metropolis, N., Rosenbluth, A. W., Rosenbluth, M. N., Teller, A. H., and Teller, E. (1953). Equation of state calculations by fast computing machines. *The Journal of Chemical Physics*, 21(6), 1087-1092.

Morris, E. M., and Wingham, D. J. (2014). Densification of polar snow: Measurements, modeling, and implications for altimetry. *Journal of Geophysical Research: Earth Surface*, 119(2), 349-365.

Mosegaard, K., and Tarantola, A. (1995). Monte Carlo sampling of solutions to inverse problems. *Journal of Geophysical Research: Solid Earth*, 100(B7), 12431-12447.

Mosegaard, K. (1998). Resolution analysis of general inverse problems through inverse Monte Carlo sampling. *Inverse Problems*, 14(3), 405.

Mosegaard, K., and Tarantola, A. (2002). Probabilistic approach to inverse problems. *International Geophysics Series*, 81(A), 237-268.

Mosegaard, K., and Sambridge, M. (2002). Monte Carlo analysis of inverse problems. *Inverse problems*, 18(3), R29.

Neumann, T. A., Conway, H., Price, S. F., Waddington, E. D., Catania, G. A., and Morse, D. L. (2008). Holocene accumulation and ice sheet dynamics in central West Antarctica. *Journal of Geophysical Research: Earth Surface*, 113(F2).

Parrenin, F., Barker, S., Blunier, T., Chappellaz, J., Jouzel, J., Landais, A., Veres, D. et al. (2012). On the gas-ice depth difference (Δdepth) along the EPICA Dome C ice core. *Climate of the Past*, 8(2), 1089-1131.

Severinghaus, J. P., Sowers, T., Brook, E. J., Alley, R. B., and Bender, M. L. (1998). Timing of abrupt climate change at the end of the Younger Dryas interval from thermally fractionated gases in polar ice. *Nature*, 391(6663), 141.

Severinghaus, J. P., and Brook, E. J. (1999). Abrupt climate change at the end of the last glacial period inferred from trapped air in polar ice. *Science*, 286(5441), 930-934.

Severinghaus, J. P., Grachev, A., and Battle, M. (2001). Thermal fractionation of air in polar firn by seasonal temperature gradients. *Geochemistry, Geophysics, Geosystems*, 2(7).

Schwander, J., Stauffer, B., and Sigg, A. (1988). Air mixing in firn and the age of the air at pore close-off. *Annals of Glaciology*, 10, 141-145.

Sowers, T., Bender, M., Raynaud, D., and Korotkevich, Y. S. (1992). 15N of N2 in air trapped in polar ice: A tracer of gas transport in the firn and a possible constraint on ice agegas age differences. *Journal of Geophysical Research: Atmospheres*, 97(D14), 15683-15697.

Sigl, M., Fudge, T. J., Winstrup, M., Cole-Dai, J., Ferris, D., McConnell, J. R., Bisiaux, M. et al. (2016). The WAIS Divide deep ice core WD2014 chronologyPart 2: Annual-layer counting (031 ka BP). *Climate of the Past*, 12(3), 769-786.

Steen-Larsen, H. C., Waddington, E. D., and Koutnik, M. R. (2010). Formulating an inverse problem to infer the accumulation-rate pattern from deep internal layering in an ice sheet using a Monte Carlo approach. *Journal of Glaciology*, 56(196), 318-332.

Steig, E.J., Kahle, E.C., Schauer, A.J., Jones, T.R., Morris, V.M., Vaughn, B.H., and White, J.W.C. Continuous-flow analyses of the complete water isotope composition of ice cores. *Rapid Communications in Mass Spectrometry*. Unpublished manuscript.

Stenni, B., Jouzel, J., Masson-Delmotte, V., Rthlisberger, R., Castellano, E., Cattani, O., Selmo, E. et al. (2003). A late-glacial high-resolution site and source temperature record derived from the EPICA Dome C isotope records (East Antarctica). *Earth and Planetary Science Letters*, 217(1-2), 183-195.

Stenni, B., Masson-Delmotte, V., Selmo, E., Oerter, H., Meyer, H., Rothlisberger, R., Hoffmann, G. et al. (2010). The deuterium excess records of EPICA Dome C and Dronning Maud Land ice cores (East Antarctica). *Quaternary Science Reviews*, 29(1-2), 146-159.

Stenni, B., Buiron, D., Frezzotti, M., Albani, S., Barbante, C., Bard, E., Capron, E. et al. (2011). Expression of the bipolar see-saw in Antarctic climate records during the last deglaciation. *Nature Geoscience*, 4(1), 46.

Tarantola, A. (1987). Inverse problem theory: Methods for data fitting and model parameter estimation. *Elsevier*, Amsterdam.

Veres, D., Bazin, L., Landais, A., Toy Mahamadou Kele, H., Lemieux-Dudon, B., Parrenin, F., Chappellaz, J. et al. (2013). The Antarctic ice core chronology (AICC2012): an optimized multi-parameter and multi-site dating approach for the last 120 thousand years. *Climate of the Past*, 9(4), 1733-1748.

Vinther, B. M., Clausen, H. B., Johnsen, S. J., Rasmussen, S. O., Andersen, K. K., Buchardt, S. L., Svensson, A. et al. (2006). A synchronized dating of three Greenland ice cores throughout the Holocene. *Journal of Geophysical Research: Atmospheres*, 111(D13).

Whillans, I. M., and Grootes P. M. (1985). Isotopic diffusion in cold snow and firn. *Journal of Geophysical Research*, 90(D2), 3910–3918.

Winski, D. A., Fudge, T. J., Ferris, D. G., Osterberg, E. C., Fegyveresi, J. M., Cole-Dai, J., Buizert, C. et al. (2019). The SP19 chronology for the South Pole Ice CorePart 1: volcanic matching and annual layer counting. *Climate of the Past*, 15(5), 1793-1808.

Chapter 4

IMPACTS OF TOPOGRAPHY AND CO_2 CHANGE ON ANTARCTIC GLACIAL-INTERGLACIAL TRANSITIONS

Emma C. Kahle, Eric J. Steig, Dargan M. W. Frierson

Large changes in the climate system, such as the most recent glacial-interglacial transition, provide opportunities to study a robust signal in the paleoclimate record. Recent improvements in interpretation of East Antarctic ice-core data estimate a deglacial temperature increase of about 6°C, significantly less than estimates for the Arctic. General circulation models (GCMs) are important tools for examining the physical mechanisms underlying such a change in the climate system. In this work we use an aquaplanet GCM to simulate glacial-interglacial transitions with idealized topography and CO_2 changes. We find a simple relationship between elevation and temperature sensitivity to radiative forcing. Due to the high elevation of Antarctica, polar amplification of surface warming is damped. Without high albedo over ice, these simulations suggest a possible explanation related to the vertical structure of the atmosphere. This result is important for comparison of ice-core data from sites at differing elevations, as well as for model-data comparisons of reconstructed temperature change.

4.1 Introduction

Earth's climate system has cycled through glacial and interglacial periods for over two million years. The timing of these cycles is driven by orbital changes that alter the timing and distribution of insolation hitting Earth (Milankovitch, 1941; Hayes et al., 1976). The mean climate forcing imparted by these insolation changes is amplified by internal feedbacks within the climate system, resulting in large swings between glacial and interglacial climate states. Studying the climate dynamics and feedbacks that have driven large climate changes in the past improves understanding of Earth's climate system.

To study past climate changes, we can use either paleoclimate data or models of the climate system. Observations from proxies such as tree rings, ice cores, and ocean sediment cores provide information about changes that have occurred in the past (Evans et al., 2013). Climate models of varying complexity from simple, toy models to fully-coupled general circulation models (GCMs) provide information about how various processes may produce changes in climate (Hoskins, 1983). When reconstructions and simulations of past change between data and models are consistent, we have higher confidence in those estimates and can validate the utility of the model (Braconnot et al., 2007). When data and model estimates differ, we must reconcile the discrepancy.

Temperature reconstructions from ice cores have long been used as paleoclimatic data constraints on Earth's climate sensitivity (Manabe and Broccoli, 1985; Genthon et al., 1987; Lorius et al., 1990) and are often used as validation against paleoclimate results from GCMs (Annan and Hargreaves, 2015). A major focus has been on the most recent large-scale change in Earth's climate, the glacial-interglacial temperature change from the last glacial maximum (LGM) to the present day. Current estimates of the glacial-interglacial temperature change in East Antarctica using water-isotope paleothermometry are about 8 - 11°C (Genthon et al., 1987; Jouzel et al., 2003; Stenni et al., 2003). However, GCM results indicate a smaller change of about 5 - 8.5°C (*i.e.* Masson-Delmotte et al. (2006); Braconnot et al. (2007); Masson-

Delmotte et al. (2013)). Despite model-data agreement on mid-Holocene temperatures, this longstanding model-data discrepancy in LGM temperatures has led to scrutiny of the physics included in models against the assumed accuracy of the data reconstructions (Crowley and North, 1991; Masson-Delmotte et al., 2006).

The most recent temperature reconstructions from East Antarctic ice cores revise previous data estimates and agree well with GCM temperature estimates. With higher-resolution ice-core data, new analysis techniques that do not rely on the conventional linear-scaling of water-isotope records give glacial-interglacial estimates of about 6°C (Kahle et al., in prep.; Buizert et al., in prep.; Markle et al., in prep.). Smaller values require that the isotope-temperature relationship vary through time. The conventional East Antarctica isotope-temperature estimates are greater because this relationship is assumed to be constant (Jouzel et al., 2003). With improved interpretation of water-isotope data, the model-data mismatch is reconciled without revision of the physics included in climate models. As such, climate models can be used as tools to determine the physical mechanisms underlying glacial-interglacial temperature changes.

Within the context of Antarctic glacial-interglacial temperature changes, two of the most important forcings and feedbacks are changes in ice-sheet elevation and changes in atmospheric CO_2 concentration. Many modeling studies have shown that earth surface topography can affect global climate dynamics (e.g. (Kageyama and Valdes, 2000; Justino and Peltier, 2006; Hamon et al., 2012; Justino et al., 2015)), and specifically that the elevation of the Antarctic ice sheet can affect local and global atmospheric and oceanic circulation (e.g. (Justino et al., 2014; Knorr and Lohmann, 2014; Steig et al., 2015; Singh et al., 2016; Salzmann, 2017)). The importance of atmospheric CO_2 concentration in climate models has been widely studied (e.g. (Manabe and Wetherald, 1975)), and many studies have looked specifically at the impacts of atmospheric CO_2 changes in the high latitudes (e.g. Gallee et al. (1992); Loutre and Berger (2000); Singh et al. (2017)). Combining the effects of topography and CO_2 concentration, previous work has shown that a strong inversion over Antarctica is important for

setting the Antarctic temperature response to glacial-interglacial changes. While a negative lapse-rate feedback at low latitudes allows vertical mixing of surface warming, inversions over the Antarctic ice sheet trap warming at the surface, leading to amplified polar warming (Pithan and Mauritsen, 2014; Salzmann, 2017; Hahn et al., 2019).

Many of these studies use fully-coupled ocean-atmosphere models, representing the upper end of the model-complexity hierarchy (Hoskins, 1983; Held, 2005). Although these models incorporate as many details as possible about the climate system, the complexity of interactions can obscure the understanding of individual processes. On the opposite end of the model-complexity hierarchy, the simplest models seek to understand particular processes at the possible cost of neglecting key processes in the real climate system. Mid-complexity models are valuable tools in striking this balance between simulation and understanding (Held, 2005; Blackburn and Hoskins, 2013). In this study, we use a mid-complexity model designed to fill the gap between idealized modeling and high-end simulations.

To improve understanding of Antarctic glacial-interglacial warming, we compare idealized simulations using an aquaplanet GCM (as described in Kang et al. (2008)). We investigate the influence on temperature and other climate variables of Antarctic ice-sheet elevation and atmospheric CO_2 level. We seek to understand the impacts of each of these factors. With a suite of model experiments comparing LGM-like and pre-industrial-like topography and CO_2 states, we determine that reduced elevation enhances polar amplification of surface temperature even without a surface temperature inversion.

4.2 Methods

In this work, we use the aquaplanet version of the AM2 model, an atmospheric general circulation model developed at the Geophysical Fluid Dynamics Laboratory (Anderson et al., 2004; Kang et al., 2008). The model grid has a horizontal resolution of 2° of latitude by 2.5° longitude, with 24 vertical levels. The surface of the planet is covered by a motionless, slab

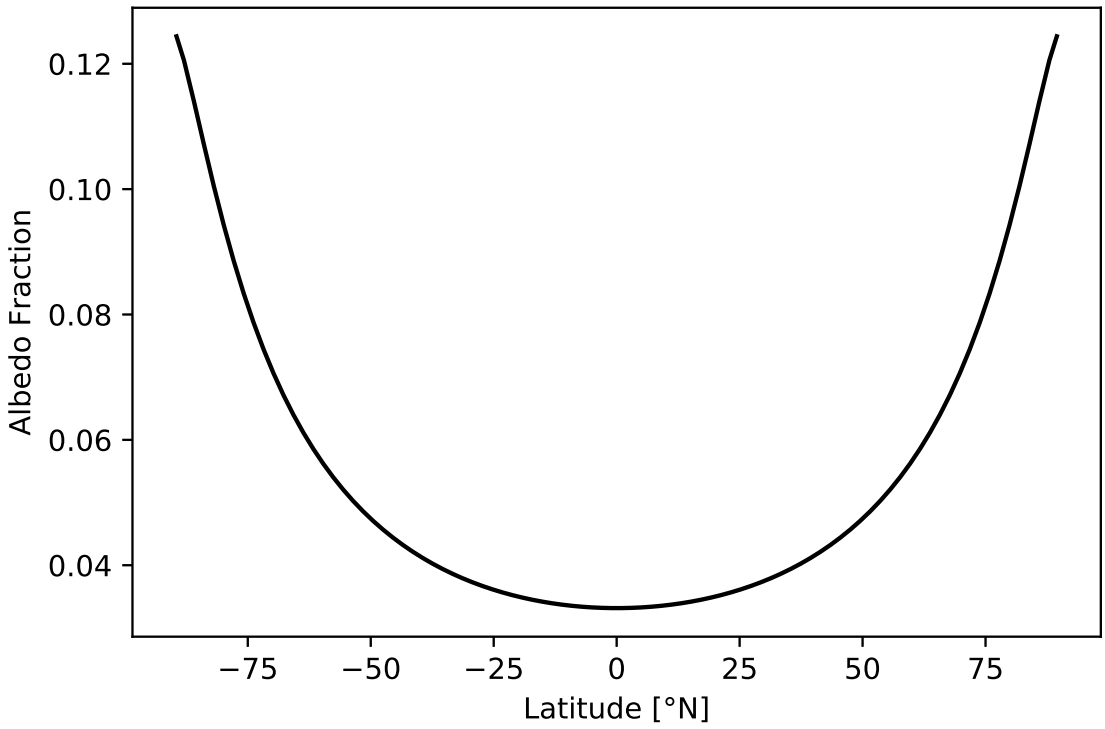

Figure 4.1: Albedo of the aquaplanet as it varies with zenith angle.

ocean of 2.4 meters depth. The ocean has a small heat capacity (1×10^7 J m^{-2} K^{-1}) to reduce the run time required to reach equilibrium. Ocean temperatures are allowed to drop below freezing, but no sea ice forms. The albedo of the surface varies with the angle of incidence (higher angle, higher albedo), following a simple analytic dependence on zenith angle (Taylor et al., 1996). The average albedo is approximately 0.06, an appropriate value for a dark ocean surface. Figure 4.1 shows the albedo as it varies with latitude. Finally, the obliquity of Earth's orbit is set to zero, resulting in a perpetual-equinox state. As such, there is no seasonal cycle, but the diurnal cycle is retained.

We test two different CO_2 levels, 180ppm and 280ppm, simulating glacial and interglacial states. We test three idealized topography configurations: a flat configuration (Flat), a

sloping cone (Cone), and an asymmetrical sloping-cone representing a higher East Antarctica and a lower West Antarctica (Step). The Flat runs provide a control against which to compare the effects of topography (Cone) and, in particular, asymmetric topography (Step). Figure 4.2 shows surface height maps and vertical profiles of each configuration. The height of Step is equal to that of Cone over East Antarctica and varies only over West Antarctica. The outlines of the continents are for reference only, as no simulations include any land surface. Note that the topography in Cone and Step extends to 50°S, beyond the outlined continent. The small irregularity in slope around 70°S reflects an artifact created by smoothing the topography. Each topography configuration is run at each CO_2 level, for a total of six model simulations, as outlined in Table 4.1.

Table 4.1: Summary of model simulations. Three topography configurations run at two CO_2 levels for a total of six simulations.

Name	**Topography Configuration**	**CO_2 Level**
Flat180	Flat	180 ppm
Flat280	Flat	280 ppm
Cone180	Cone	180 ppm
Cone280	Cone	280 ppm
Step180	Step	180 ppm
Step280	Step	280 ppm

We run each simulation for a total of 25 years. We disregard the first 5 years of each run as a spinup and average the remaining 20 years to yield the mean climate state. These choices for spinup and total run length are much longer than those used in previous work with this model (*e.g.* Kang et al. (2008) and Ceppi et al. (2013), who used run lengths of 7 and 8 years, respectively). Because we focus on the polar regions, which have a relatively small spatial area, we use longer run lengths to reduce the variance of the results. We evaluate the run length by comparing differences in the Flat runs. The top panel of Figure 4.3 shows

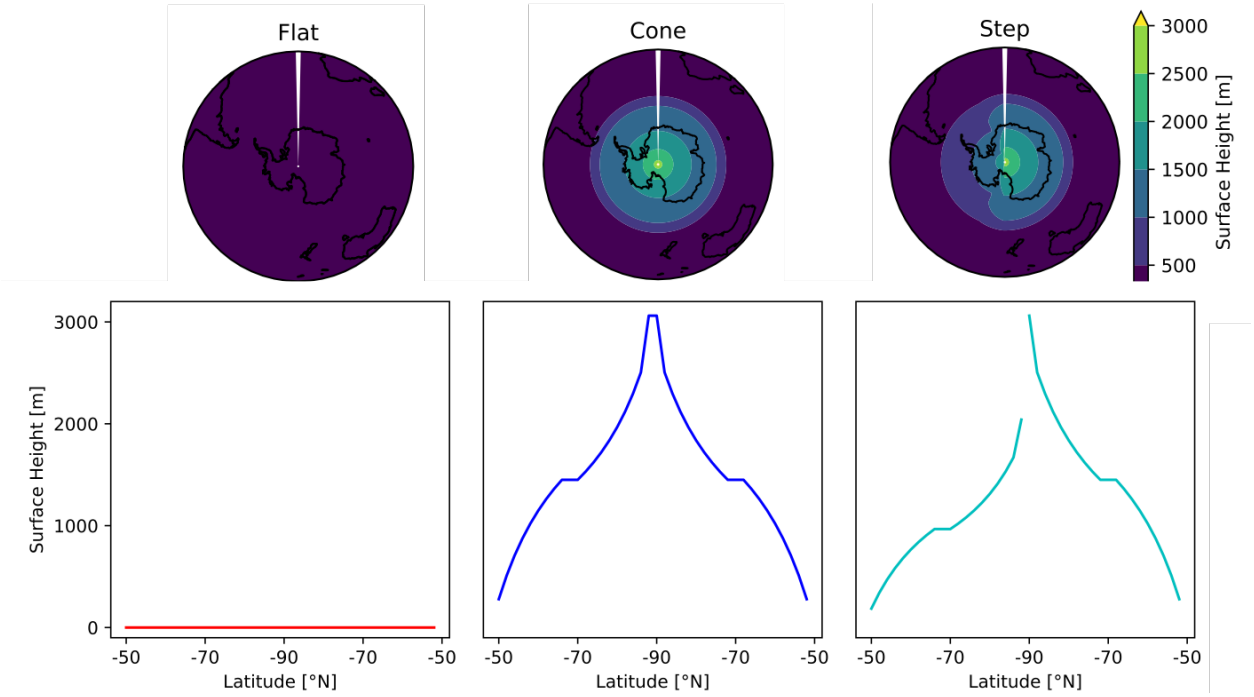

Figure 4.2: Surface height maps (upper panels) and vertical profiles (lower panels) of each topography configuration. Outlines of the continents are for reference only; there is no land surface in any of the configurations. Note that the topography in Cone and Step extends to 50°S, beyond the outlined continent.

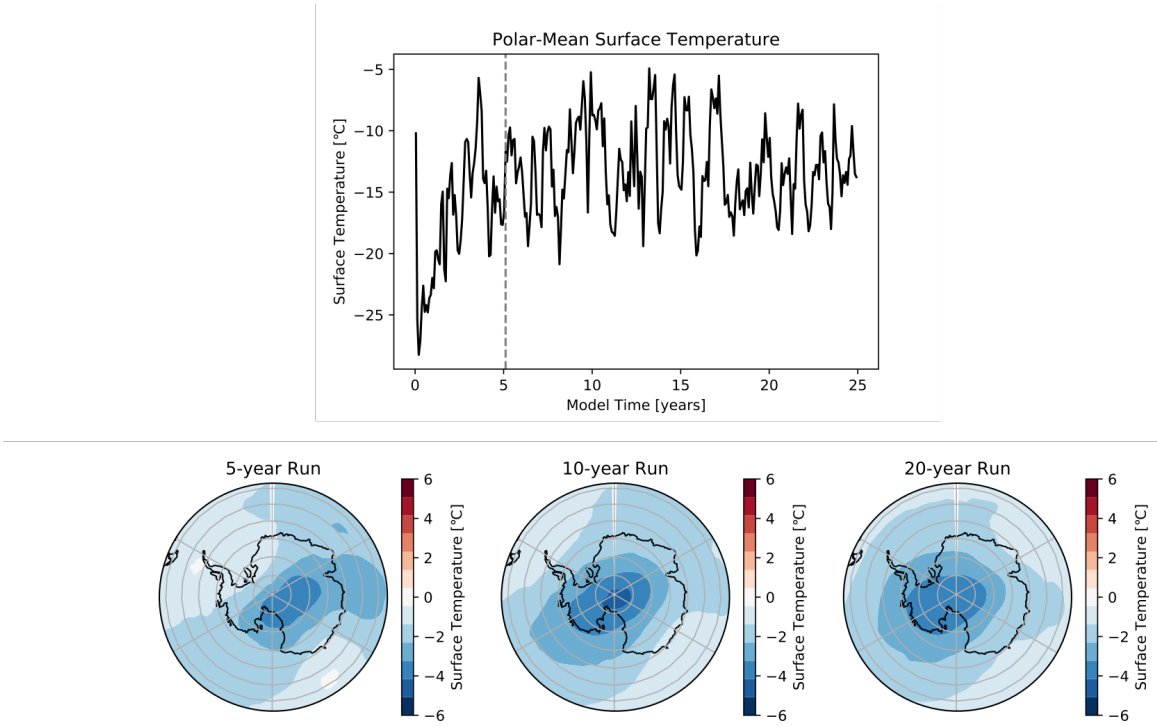

Figure 4.3: Top panel shows evolution of polar-mean surface temperature (80-90°S) through model time in Flat280. Vertical dotted line denotes end of 5-year spinup period. Bottom panels show a comparison of maps of surface temperature change at run lengths of 5, 10, and 20 years. Each bottom panel shows the difference in surface temperature between Flat280 and Flat180. Zonal symmetry increases with increasing run length.

the evolution through model time of the polar-mean surface temperature from 80-90°S. After removing the first five years as a spin up period, the mean of the temperature evolution is fairly constant. Because the equilibrium state of the Flat runs should be zonally symmetric, any deviation in zonal symmetry indicates noise relative to equilibrium. The bottom panels of Figure 4.3 show the improvement in zonal symmetry with longer run times. The difference in surface temperature between Flat280 and Flat180 becomes increasingly zonally symmetric as run length increases. As the majority of our analysis examines zonal-mean variables, the level of asymmetry produced at the 20-year run length is acceptable, and we keep this level in mind when analyzing spatial results.

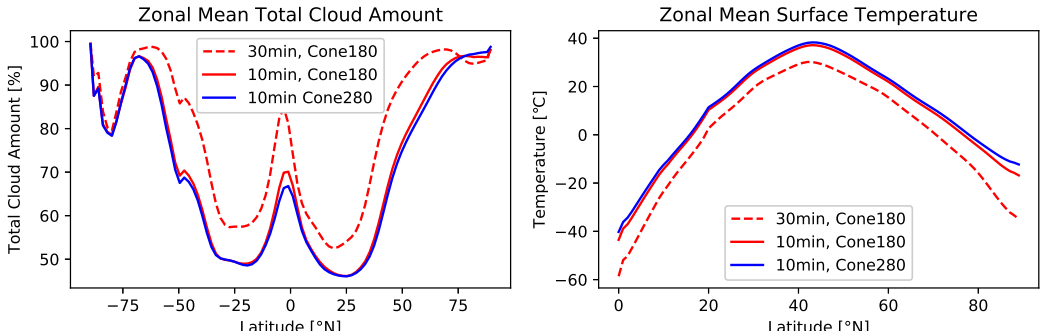

Figure 4.4: Effect of varying timesteps in the model run. Zonal-mean total cloud amount and zonal-mean surface temperature are plotted for timesteps of 10 and 30 minutes (solid red and dashed red). For comparison, the blue curve in each panel shows the much smaller change in response to a change in CO_2 holding the timestep constant at 10 minutes.

The model is run at a timestep of 10 minutes. This value is less than the default of 30 minutes, but was required to resolve numerical instabilities. Tests at different timesteps revealed large differences in mean-state results. Often, model runs at the 30-minute timestep became numerically unstable and did not produce the entire 25 years of results. When 25 years of results were successfully output, the longer timestep produced a global increase in cloud cover, mostly in low clouds. The mechanism in the longer-timestep run that created these clouds is not clear, but was associated with a decrease in global temperature due to increased outgoing-shortwave radiation. The magnitude of cooling associated with this cloud effect was much greater than the impact from changing the CO_2 level. Figure 4.4 illustrates this effect, showing in solid-red and dashed-red the difference in zonal-mean total cloud amount in the left panel and the difference zonal-mean surface temperature in the right panel. The blue curve shows the much smaller impact from a change in CO_2. We did not test timesteps shorter than 10 minutes, but point out that simulations with consistent timesteps of 10 minutes allow for robust comparisons in this analysis.

4.3 Results

We compare the results of each simulation. All topography comparisons are made at a constant CO_2 level of 280ppm.

4.3.1 Temperature

The surface temperature in Antarctica is affected by changes in both topography and CO_2 level. A reduction in topography yields local surface warming. In Figure 4.5, the upper panel shows the zonal-mean surface temperature of the Flat and Cone simulations, and the lower panel highlights the difference in surface temperature due to reduced topography (Flat280-Cone280). The dotted black line shows the difference in the surface potential temperature θ (surface temperature normalized to a constant pressure), as defined by:

$$\theta = T \left(\frac{P_0}{P} \right)^{R/c_p}, \tag{4.1}$$

where T is the surface temperature, the reference pressure $P_0 = 1000$ hPa, P is the pressure at the surface, R is the gas constant, and c_p is the heat capacity of dry air. This calculation assumes a dry adiabatic lapse rate, which is an appropriate assumption for Antarctica. The potential temperature shows that even when accounting for the effect of the lapse rate with changing elevation, there is still warming over the reduced topography. At all other latitudes, and particularly in the Southern Hemisphere tropics, there is a decrease in both surface temperature and potential temperature. This Northern Hemisphere result is entirely consistent with past work (*e.g.* Singh et al. (2016)). An asymmetrical reduction in topography produces even more warming over the lowered area, as shown in the maps of potential-temperature change in Figure 4.6. In the asymmetrical case, the warming signal is stronger from longitudes 0-90°W than from 90-180°W, with a region of cooling at slightly

lower latitudes along 180°W. The warming also extends over the unchanged East Antarctic topography within the high latitudes.

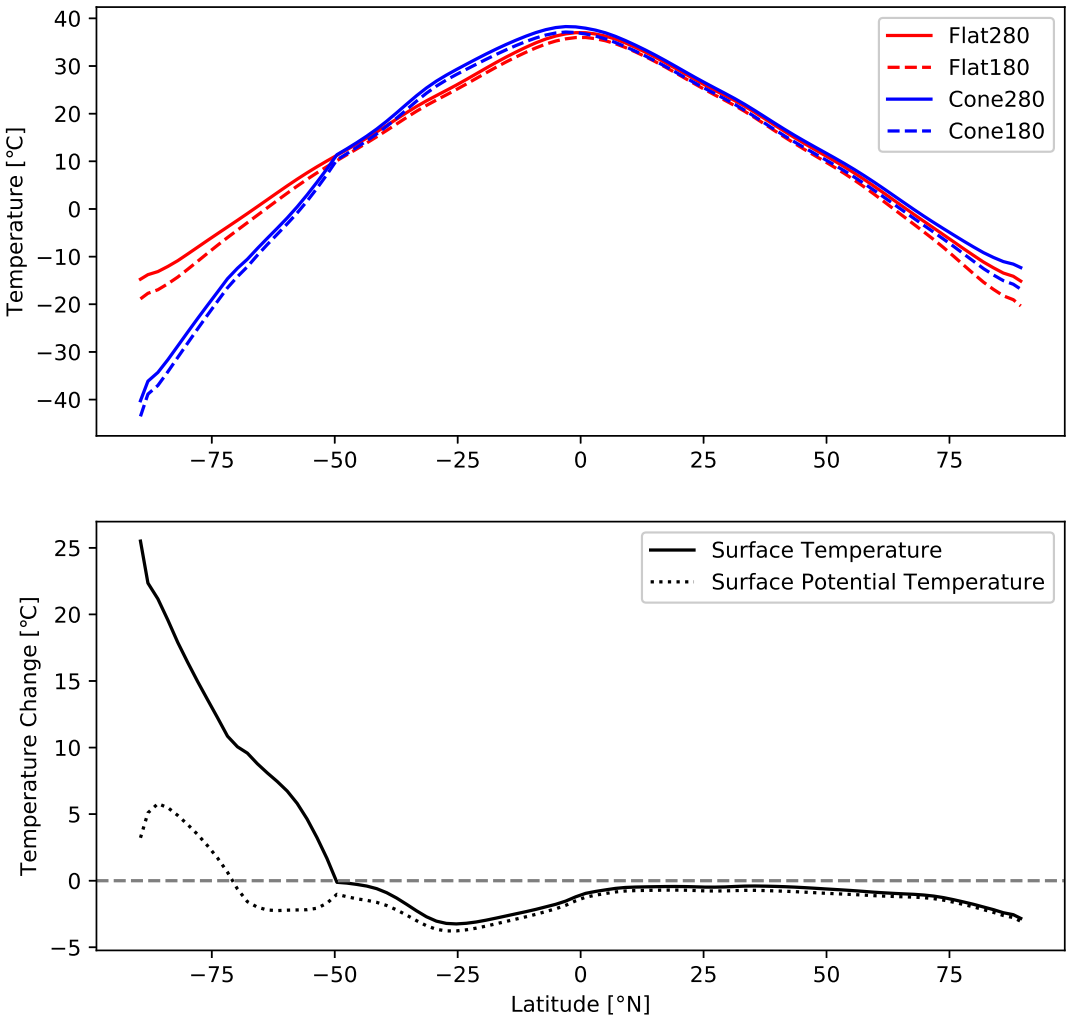

Figure 4.5: Zonal-mean surface and potential temperature. The upper panel shows surface temperature for Flat and Cone at each CO_2 level. The bottom panels show the change due to topography for surface and potential temperatures with CO_2=280ppm.

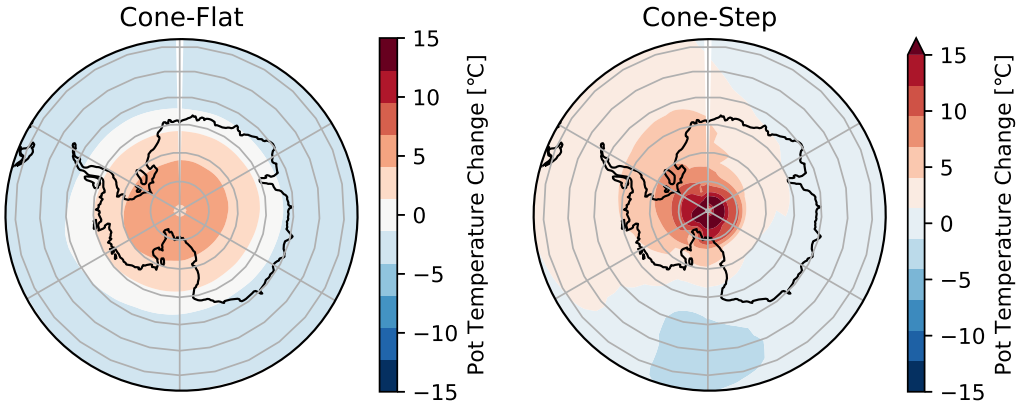

Figure 4.6: Response in surface potential temperature to a change in topography. The differences in Cone-Flat and Cone-Step both run with CO_2=280ppm.

The upper panel of Figure 4.5 illustrates that, regardless of topography, an increase in CO_2 yields an increase in surface temperature at all latitudes. Figure 4.7 highlights this response to increased CO_2 in Flat and Cone. There is a larger difference in the temperature responses over Antarctica compared with the high-northern latitudes. Figure 4.8 shows vertical profiles of the polar-mean temperature, averaging the temperature at a given height over all latitudes greater than 80°S. We divide the results of Step into Step East (longitudes 0-180°E) and Step West (longitudes 0-180°W). The left panel shows the absolute profiles for each simulation, and the temperature gradient just above the surface indicates the stability of the near-surface air. The Cone and Step East simulations have the largest temperature gradient with height just above the surface, and thus the least-stable surface air. Flat has a nearly-vertical temperature gradient above the surface, and thus the most-stable surface air. However, unlike temperature observations from Antarctica, none of the simulations produces a strong temperature inversion due to much lower albedo of the aquaplanet ocean compared to the ice-sheet surface. The right panel shows the responses of each simulation to an increase in CO_2. Flat shows the greatest surface warming, while Cone and Step East show the least surface warming. The surface warming response in Step West is intermediate between the

high topography and Flat.

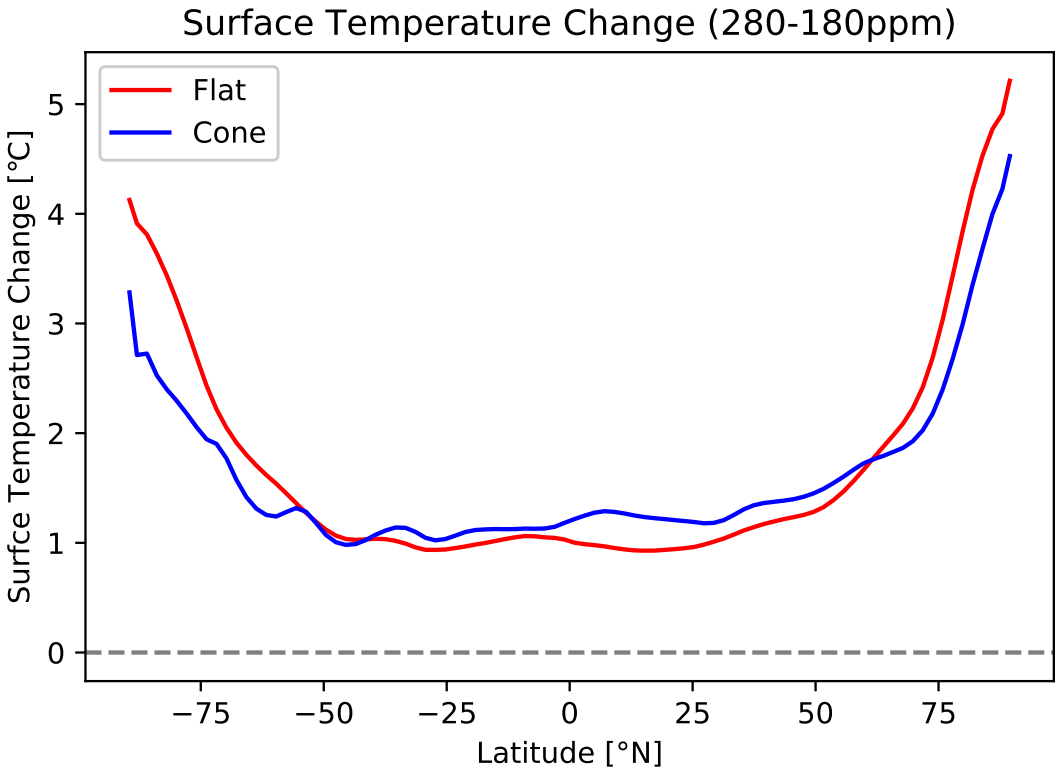

Figure 4.7: Zonal-mean surface temperature response to CO_2 change in Flat and Cone.

4.3.2 Energy Balance

The different components of the energy balance can be characterized by the top-of-atmosphere (TOA) net incoming radiation together with the outgoing longwave (LW) radiation. The TOA net radiation is defined as the difference between incoming shortwave (SW) radiation and outgoing SW and LW radiation:

$$Net\ Radiation_{TOA} = SW_{in} - (SW_{out} + LW_{out}) \tag{4.2}$$

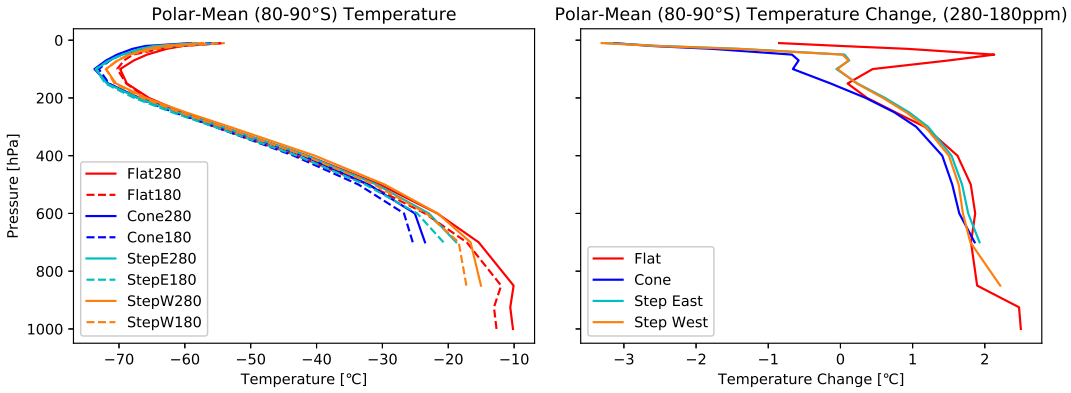

Figure 4.8: Vertical profiles of temperature averaged from 80-90°S. The left panel shows absolute profiles for each simulation, where Step results have been separated into Step East and Step West. The right panel shows the response in each topography configuration to an increase in CO_2.

The middle panels in Figure 4.9 show that a reduction in topography leads to three distinct changes in the radiation balance: 1) a local decrease in the net and increase in outgoing LW radiation, 2) an increase in the net and decrease in the LW radiation at mid-southern-latitudes, and 3) a southward shift of the local minimum in both the net and outgoing LW radiation. An increase in CO_2 has a smaller impact on the energy balance and varies only slightly with topography (right two panels). Over the topography, Cone and Flat have similar responses in outgoing LW radiation change, but Cone has a smaller change in the net radiation. Flat has a larger response in outgoing SW radiation (not shown) in order to balance Equation 4.2. In the tropics, the outgoing LW radiation decreases more in Flat than in Cone. Finally, in the high northern latitudes, Flat has a greater response in both net and LW radiation as compared with Cone, a difference not seen in the temperature result.

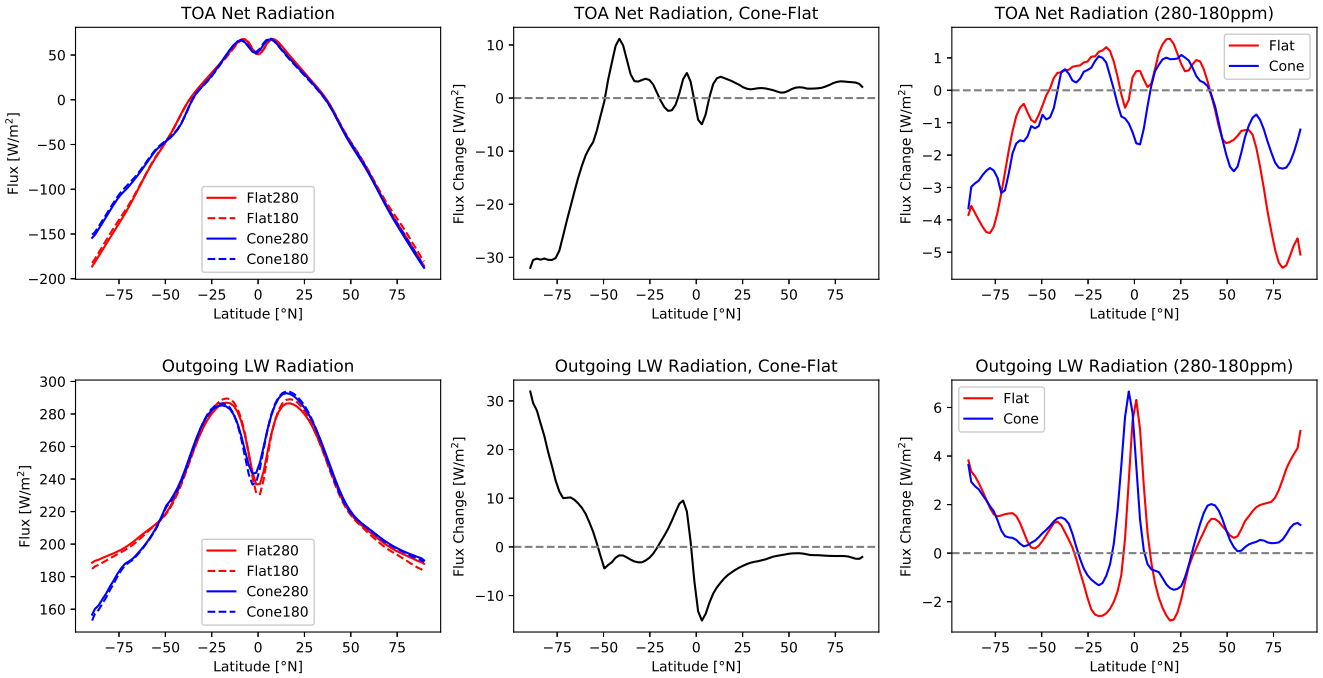

Figure 4.9: Radiation balance as described by top-of-atmosphere (TOA) net radiation (defined as positive for incoming radiation) and outgoing longwave (LW) radiation. Zonal mean plotted for Cone and Flat simulations (left panels), in addition to the responses to topography change at CO_2=280ppm (middle panels) and CO_2 change (right panels).

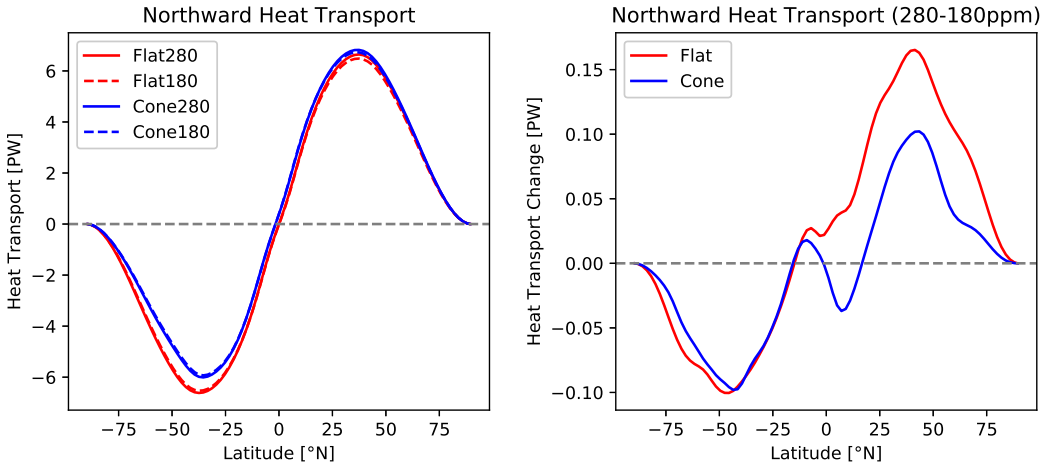

Figure 4.10: Northward heat transport calculated from integrating the TOA net radiation from 90°S to 90°N. Zonal mean for Cone and Flat shown on the left, and response in zonal mean to CO_2 change shown on right.

The northward heat transport (NHT) is determined by integrating the energy imbalance from the TOA net radiation over the surface of the Earth from 90°S to 90°N. With reduced topography, there is a decrease in the NHT, especially in the Southern Hemisphere (left panel of Figure 4.10). Flat has a greater NHT response to CO_2 change, especially in the Northern Hemisphere, but also from 50-80°S (right panel of Figure 4.10).

4.3.3 Clouds and Precipitation

The largest effect on clouds, both low and high, comes from a change in topography. The upper left panel in Figure 4.11 shows that low clouds increase significantly over the largest change in topography (70-90°S), while they decrease slightly on the sloping edge of the topography (70-50°S), and the response oscillates towards lower latitudes. High clouds experience the opposite effect, with a decrease over the reduced topography and increase over the sloping edge. High clouds also show a shift in maximum near the equator. In both high and low clouds there is a slight increase in northern latitudes.

The bottom panels of Figure 4.11 show the responses of clouds to changing CO_2. Increasing CO_2 causes a large decrease in all cloud cover near the equator. In mid-latitudes, there is a decrease in low clouds and slight increase in high clouds. Over Antarctica, the responses differ for Cone and Flat. In Cone, there is a decrease in low clouds and increase in high clouds, while in Flat there is a decrease in high clouds and little change in low clouds. In general, the trends in the total cloud amount follow closely the trends in the low cloud amount, suggesting that low clouds are more dominant than high clouds.

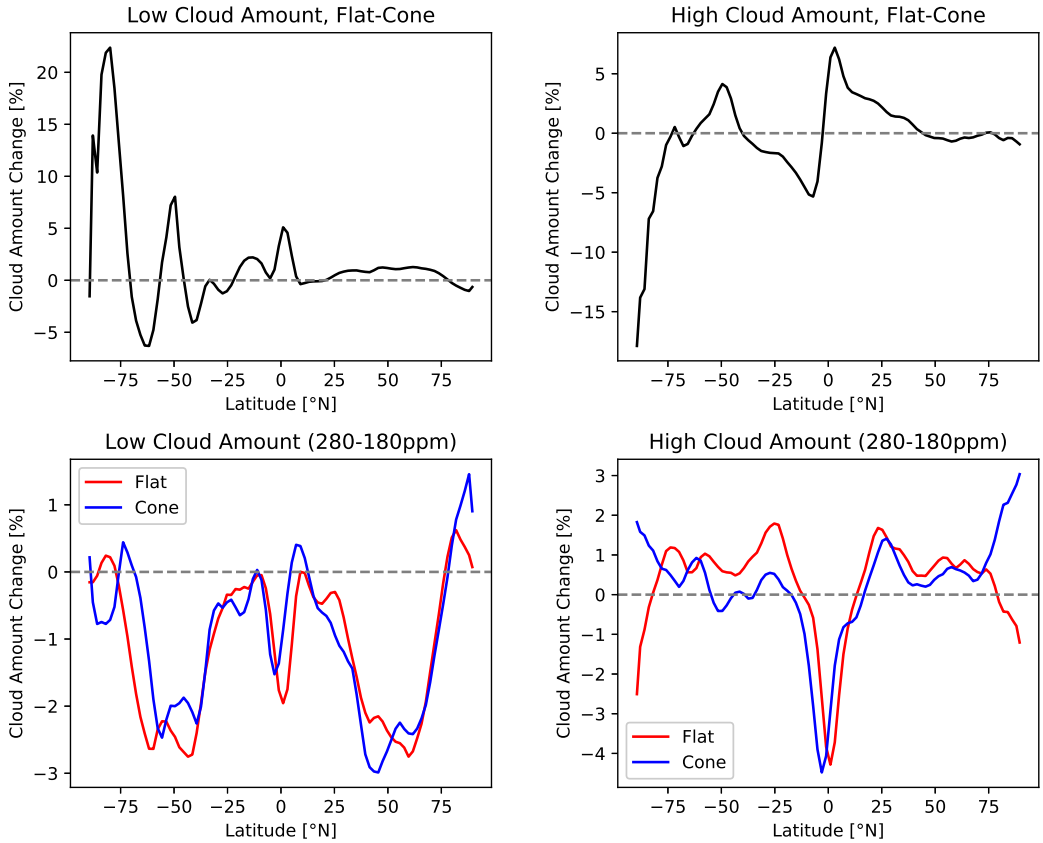

Figure 4.11: Responses in low and high cloud amounts. Top panels show responses to topography change with CO_2=280ppm, and bottom panels show responses to CO_2 change.

Precipitation is related to cloud cover, but the regions of largest change differ. The left panel of Figure 4.12 shows that the largest change in precipitation due to reduced topography is a northward shift of the low-latitude maximum. Following the pattern of low clouds, there is a small decrease in precipitation over the edge of the continent (50-70°S) and a small increase in precipitation over the middle of the continent (70-90°S). The right panel shows the response of the difference between moist static energy and dry static energy (MSE-DSE) to the reduced topography. There is a large decrease in MSE-DSE throughout all levels of the troposphere in the southern tropics.

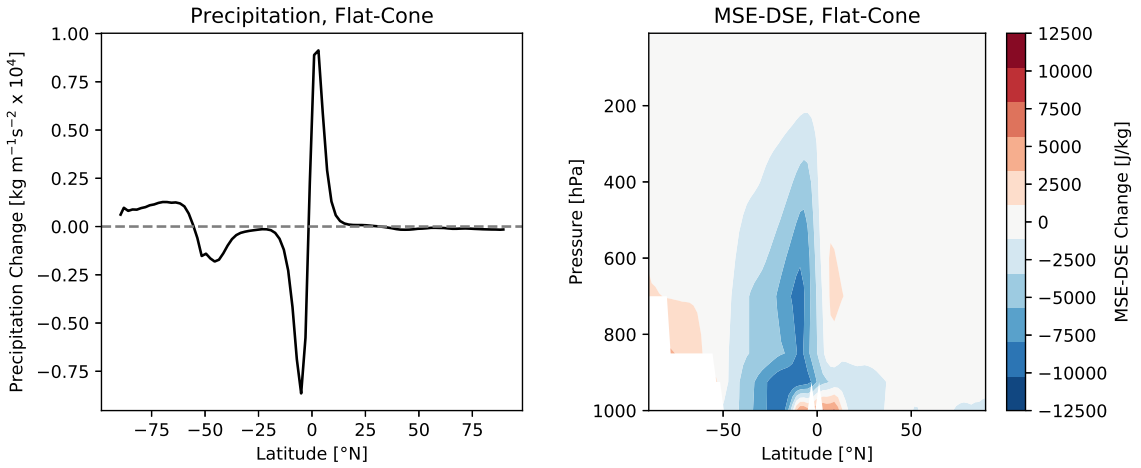

Figure 4.12: Response to reduced topography in total precipitation (left) and in the difference between moist static energy and dry static energy (MSE-DSE) (right). All runs at CO_2=280ppm

4.3.4 Winds

Figure 4.13 illustrates the surface-wind response to changes in topography. In Flat, the winds decrease with increasing latitude from westerlies around 60°S to almost zero at 90°S. With the addition of Cone topography, the sloping elevation leads to southerly winds at the highest latitudes, which tend towards easterlies due to the Coriolis force. Note that for this

particular comparison we show the addition, rather than the reduction, of topography to illustrate how winds are generated by an increase in topography. Asymmetric topography further affects the surface winds. Over East Antarctica, Step also creates strong easterlies. Over West Antarctica, Step results in an increase in westerly strength over West Antarctica, though the prevailing wind direction is still easterly.

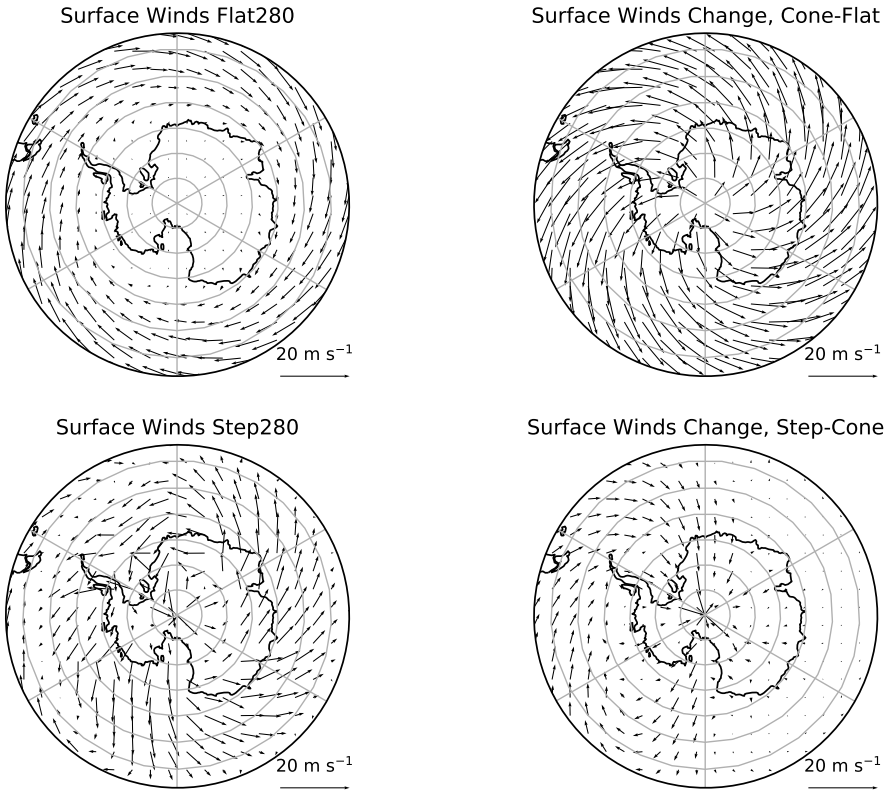

Figure 4.13: Response in surface winds to changes in topography. Upper left panel shows surfaces winds in Flat280. Upper right panel shows response to addition (rather than reduction) of Cone topography at CO_2=280ppm. Lower left panel shows surface winds in Step280. Lower right panel shows response in reducing topography from Cone to Step at CO_2=280ppm.

Response to changing CO_2 level affects the winds to a lesser degree than topography. The main feature seen in response to CO_2 change is an increase in westerly winds in the stratosphere in the tropics. This increase is amplified in Cone, and there is an additional increase in westerly winds at all pressure levels in the high northern latitudes of Cone.

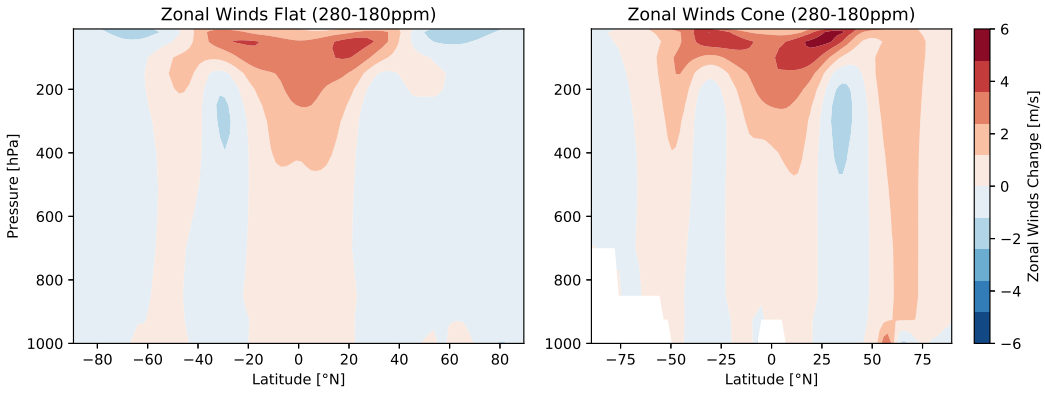

Figure 4.14: Vertical profile of zonal mean shown for zonal component of the wind. Left and right panels show the responses to CO_2 change in Flat and Cone, respectively.

4.4 Discussion

The results from our six model simulations provide insight into how Antarctic topography and the atmospheric CO_2 level impact climate dynamics on local and global scales. First we examine the impact of topography in isolation, concluding that this work confirms the results of many past studies on Antarctic elevation change. Second we consider the combined impact of changes in topography and CO_2 together. We find that an increase in topography damps polar amplification of surface warming.

4.4.1 Impact of Topography

A reduction in Antarctic topography leads to local warming and remote cooling at all other latitudes. This result has been found in previous GCM studies examining changes in Antarc-

tic topography (Ogura and Abe-Ouchi, 2001; Knorr and Lohmann, 2014; Singh et al., 2016). To accommodate the increased outgoing LW radiation due to this warming, southward energy transport increases. This mechanism is explained by Ogura and Abe-Ouchi (2001) and replicated in many other atmospheric GCM studies (*e.g.* Mechoso (1981); Simmonds and Law (1995); Quintanar and Mechoso (1995); Walsh et al. (2000)). These studies show that the increase in southward energy transport is accomplished by baroclinic eddies.

This change in the meridional heat-transport causes a northward shift of the intertropical convergence zone (ITCZ) in response to a decrease in Antarctic topography. This shift is reflected in the responses of the energy balance, the cloud cover, and the precipitation. The northward ITCZ shift drives cross-equatorial energy transport to transfer more energy southward. Previous studies have found that the ITCZ shifts towards the warmer hemisphere (Broccoli et al., 2006; Kang et al., 2008; Ceppi et al., 2013). This result is consistent with our result because an increase in topography is effectively an increase in energy due to decreased outgoing LW radiation over the continent. Other work emphasizes this shift in terms of achieving meridional energy balance, highlighting the ITCZ shift towards the more energetic hemisphere (Chiang and Bitz, 2005; Kang et al., 2008; Frierson and Hwang, 2012; Singh et al., 2016). Consistent with previous work, our results show the ITCZ shift away from the decreased topography in order to increase southward energy transport and balance the TOA radiative energy loss from topography reduction. Singh et al. (2016) showed that in atmosphere-only models, without the contribution of ocean heat transport, the atmosphere is solely responsible for increasing southward energy transport to balance the hemispheres. In the absence of ocean heat transport, the ITCZ shift in these simulations is greater than it would be if coupled to a circulating ocean.

The presence of topography has a significant impact on the dynamics of cloud formation over Antarctica. Over higher and colder topography, there is less moisture available to form clouds. With fewer low clouds, less SW radiation is reflected back to space. Despite this increase in SW radiation that reaches the surface, the outgoing LW radiation is still lower

over the topography due to the decrease in surface temperature. Therefore, the decrease in cloudiness that results from the presence of the ice sheet acts to damp the response of surface energy balance.

Strong, easterly down-sloping winds develop over Cone and Step, compared to the almost-static polar winds in Flat. The strong easterly component reflects the balance between the Coriolis force and surface friction (Parish and Waight, 1987). The pattern of surface wind change in West Antarctica in Step compared to Cone is associated with conservation of potential vorticity. As the easterlies flow downslope from longitude 0 to 45°W, the height of the atmosphere increases and the air column would be expected to spin up in the same direction as the planetary vorticity, resulting in a cyclonic circulation anomaly (Steig et al., 2015). The opposite effect occurs for winds heading upslope towards East Antarctica from 135°W to 180°W where the height of the atmosphere decreases. Steig et al. (2015) found the same result in a suite of models of increasing complexity. They showed that these changes in surface winds directly correspond to changes in potential temperature. In Figure 4.15 we make the same comparison and likewise conclude that changes in the winds are associated with temperature changes not accounted for by the lapse rate from elevation change.

4.4.2 Combined Impact of Topography and CO_2 Change

A significant outcome of this work is that polar amplification of warming due to increased CO_2 is damped locally by increased Antarctic topography. Figure 4.16 shows that with lower topography, an increase in CO_2 causes greater polar amplification. We calculate polar amplification as the polar surface-temperature change (80°S to 90°S) divided by the surface-temperature change in the tropics (30°S to 30°N). The normalized change provides a metric of polar amplification by accounting for differences in low-latitude temperature change in each simulation. The Step results are separated into East and West Antarctica, demonstrating that, even within the same simulation, this relationship holds over varying elevation. Comparing Flat and Cone, the presence of an idealized ice sheet damps polar amplification

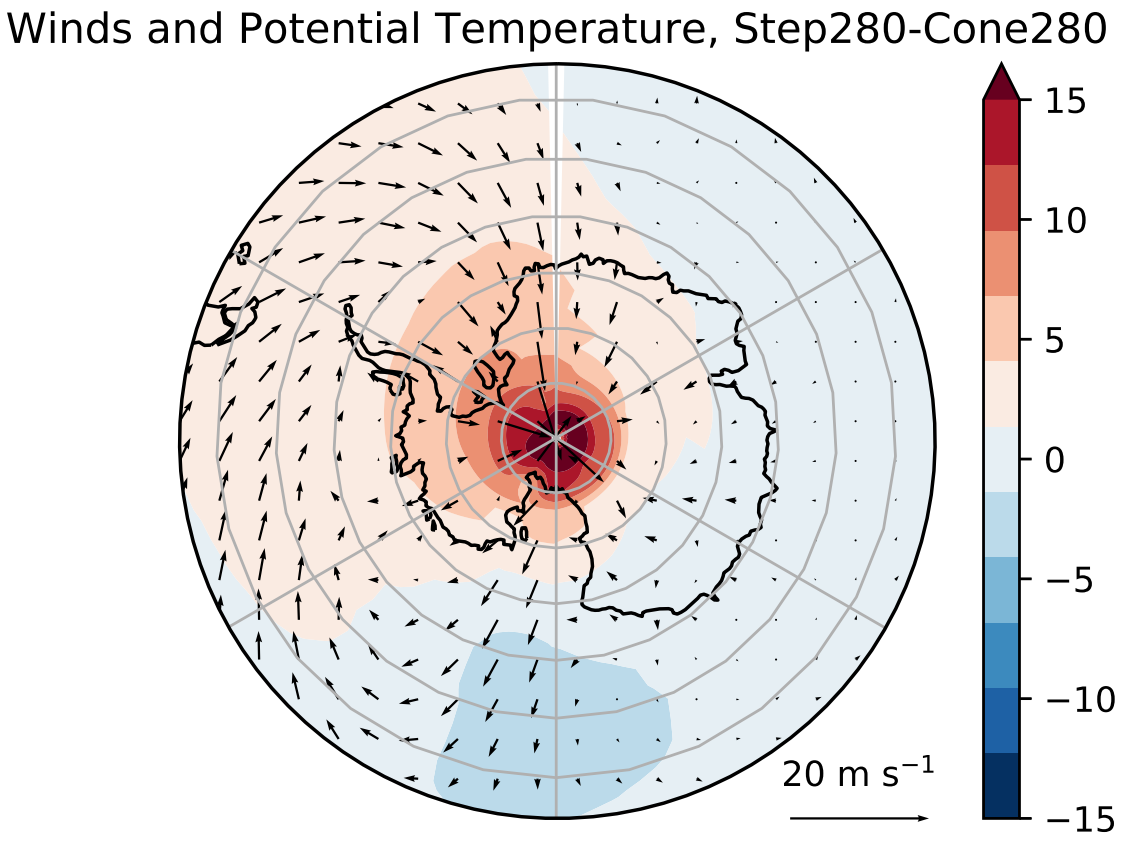

Figure 4.15: Response of surface winds and surface potential temperature to reduction in topography from Cone to Step with CO_2=280ppm.

by a factor of about 1.6, similar to the factor between Southern and Northern Hemisphere polar amplification found in the analysis of PMIP2 models by Masson-Delmotte et al. (2006).

This relationship can be further examined by considering the vertical profiles of temperature and temperature change over Antarctica. The left panel of Figure 4.8 shows the temperature profile, which defines the lapse rate Γ:

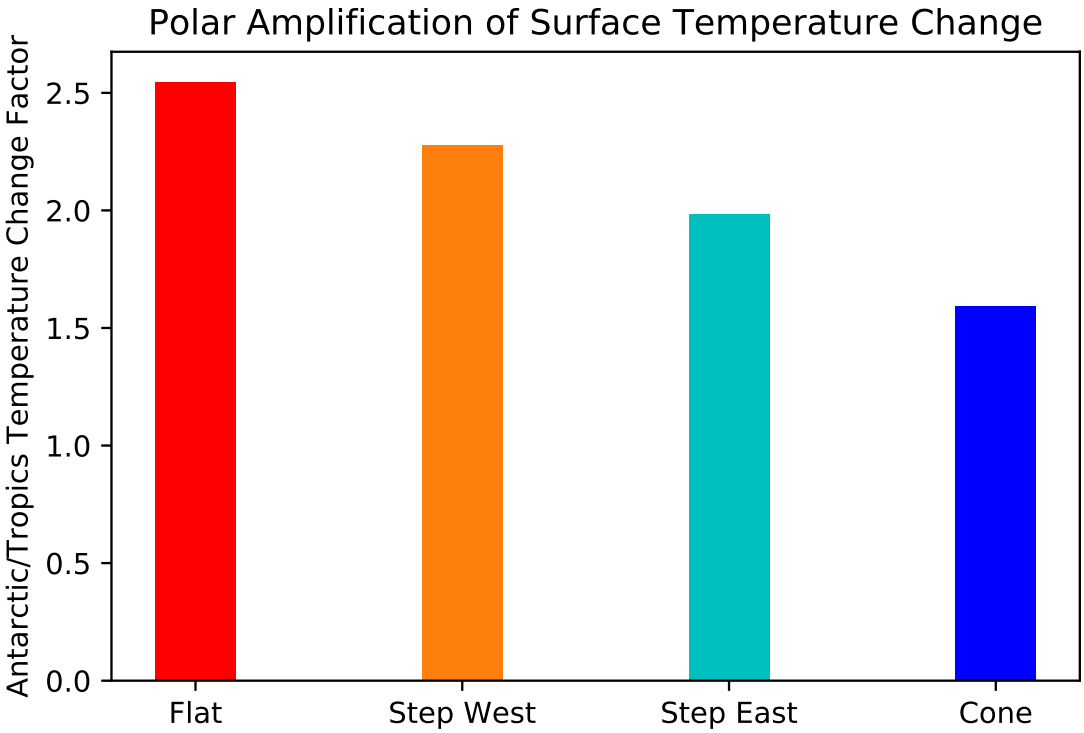

Figure 4.16: Response of polar-mean surface temperature to increased CO_2 for each simulation. Values are normalized by dividing the polar-mean surface temperature change (80°S-90°S) by the mean of the low-latitude surface temperature change (30°S-30°N) to get a metric for polar amplification of warming.

$$\Gamma = -\frac{dT}{dz}, \tag{4.3}$$

where T is temperature and z is height in the atmosphere. A smaller lapse rate Γ corresponds to a more stable air column based on the principles of static stability (Wallace and Hobbs, 2006). The right panel of Figure 4.8 shows the change temperature, or the change in lapse rate Γ, in response to increased CO_2. In all simulations, the temperature change is greatest at the surface. The surface warms 2.5°C over Flat, 2.2°C over Step West, 1.9°C over Step

East, and 1.8°C over Cone. Although the magnitude of surface warming decreases with elevation, all four vertical profiles of temperature change are quite similar at given pressure levels.

The temperature change gradient with height is indicative of a positive lapse-rate feedback across all simulations: the temperature change aloft is smaller than the change at the surface. This corresponds to a greater lapse rate Γ in response to increased CO_2, which results in a decrease of static stability. This result is in stark contrast to the temperature change profile typical in the tropics. In the low latitudes, surface temperature changes are small compared to the temperature changes in the upper troposphere, indicating a negative lapse-rate feedback where the vertical structure becomes more stable in response to surface warming.

The positive lapse-rate feedback in these simulations is connected to the relatively stable near-surface temperature structure. The left panel of Figure 4.8 shows that Γ is close to zero above each topography configuration. A stable near-surface strucutre, frequently observed over Antarctica and seen in more complex model results (Salzmann, 2017; Hahn et al., 2019), is often attributed to the surface-cooling effects of high albedo over ice as well as prolonged seasonal darkness in austral winter. However, stable profiles are present in these simulations even over a dark ocean surface with low albedo and in a perpetual-equinox state where all latitudes north of 90°S receive year-round sunlight. Even without the factors of albedo and seasonality of sunlight, the vertical temperature profiles in these simulations are stable enough to be associated with a positive lapse-rate feedback.

The stability of the vertical temperature profile is not identical across the simulations, but decreases with elevation as Γ increases. The vertical structure in Flat is the most stable with a Γ of approximately zero, while Γ increases with increasing elevation. This greater stability over lower topography is associated with more trapping of surface warming. A possible, simple explanation for this stability is that increased air mass at lower elevation allows for more radiative cooling near the surface, which in turn creates a more stable temperature profile. This increased stability then allows for more surface warming. In reality, many other

factors influence the stability of the vertical profile as well, including the stable boundary layer flux, which is highly uncertain in models, as well as surface type and roughness, which impact boundary layer turbulence.

Future work should explore how changes in albedo and seasonality of sunlight affect the vertical temperature structure over Antarctic topography. The stability of the vertical structure of the atmosphere appears to play an important role in setting polar amplification. Since most modeling work includes both high albedo and seasonality, the individual impact of these factors on the stability of the vertical structure has not been previously examined. Isolating the effects of these factors, which have been excluded from the current analysis, can help to inform our understanding of how each contributes to atmospheric stability over Antarctica.

The response in cloud cover to a CO_2 change also differs between topographies, but with the opposite effect of the observed temperature response. The cloud response has a warming effect over higher elevation as reflective low clouds decrease and warming high clouds increase over the topography (Figure 4.11). This radiative change (Figure 4.9) may be balanced in Cone by a relative increase in northward heat transport out of the Southern Hemisphere compared to Flat (Figure 4.10). If this cloud effect dominated the temperature response, higher topography would have enhanced polar amplification. Rather, this cloud response may damp the more dominant effect of the stability gradient with height. Without clouds, the difference in surface warming between Cone and Flat may be even greater.

Although this work focuses on the Southern Hemisphere, there are impacts of Antarctic topography and CO_2 change in the Northern Hemisphere as well. The CO_2 response of northward heat transport (Figure 4.10), the zonal wind component (Figure 4.14), and the energy balance (the TOA net radiation and outgoing LW radiation of Figure 4.9) all show different Northern Hemisphere responses between Cone and Flat. Proposing mechanisms for these Northern Hemisphere effects is beyond the scope of this work, but we note the significant impact of Antarctic topography on northern responses to CO_2 change. These remote Northern Hemisphere effects are consistent with previous work implementing similar

topography changes, and have been explored in some detail by Singh et al. (2016).

4.4.3 Implications

The result that lowering the elevation of Antarctica enhances polar amplification is important for understanding past Antarctic temperature changes. While past modeling work has highlighted the role of a strong surface inversion and impacts of sea ice, this analysis demonstrates that more fundamental processes in the atmospheric column may contribute to the stable vertical structure. This result improves our understanding of why polar amplification over the Antarctic continent is damped compared to the Arctic, where the mean topography is lower. Past work has posited a number of more complex explanations for the large polar amplification observed in Greenland ice-core data, including dust forcing, changes in Northern Hemisphere vegetation, and feedbacks from ice albedo that influence atmospheric circulation and heat transport (Masson-Delmotte et al., 2006). In the Southern Hemisphere, the damped temperature change has been explained by increased heat uptake by the Southern Ocean (Sokolov and Rintoul, 2009) as well as the presence of the ozone hole over the continent (Thompson and Solomon, 2002, 2009). We note that modern observations also show greater warming in West Antarctica than East Antarctica (Steig et al., 2009), which is also qualitatively consistent with our experimental results. While these and other factors in both hemispheres may certainly be important as well, differences in the stability of the atmosphere also contribute to the difference in polar amplification between hemispheres. The damped Antarctic polar amplification can explain the smaller glacial-interglacial temperature change estimated from GCMs and our ice-core data reconstructions (Chapter 3) compared to the change estimated in the Arctic.

This result highlights the need for realistic reconstruction of past ice-sheet topography in GCMs, particularly when comparing model results with ice-core data. Previous GCM simulations of the LGM use a wide variety of past Antarctic ice-sheet topographies. Differences in these topographies result in surface temperature differences as large as 5°C due to changes

in the lapse rate (Abe-Ouchi et al., 2015). While understanding of ice-sheet topography and ice distribution continues to improve (*e.g.* Argus et al. (2014); Lambeck et al. (2014); Peltier et al. (2015); Hall et al. (2015)), more work is needed to ensure realistic ice-sheet reconstructions are available for GCM runs.

On timescales shorter than glacial-interglacial transitions, the impact of elevation on surface warming is also important in interpreting differences in ice-core data from East and West Antarctica. Millennial variability in West Antarctic ice-core data tends to be greater than the same variability in East Antarctic cores (Fudge et al., 2013; Markle, 2017). At least a part of this difference can be explained by the lower elevation of West Antarctica. When analyzing ice-core data from cores at different elevations, the change in air stability with height should be considered.

4.5 Conclusion

In this work we use an aquaplanet GCM to simulate different combinations of idealized Antarctic topographies and CO_2 levels to examine glacial-interglacial-like changes. We test three topography configurations and two CO_2 levels. The results show significant effects from decreasing Antarctic topography on the surface temperature, the position of the ITCZ, and surface winds in Antarctica. In response to increased CO_2, a change in topography affects polar amplification of surface warming. A decrease in topography enhances polar amplification due to increase in the stability of near-surface air, even without typical factors that increase stability such as high albedo over an ice surface and prolonged darkness in austral winter. The effect of topography on polar amplification is important in interpreting ice-core data as well as for comparing data with GCM results.

BIBLIOGRAPHY

Abe-Ouchi, A., Saito, F., Kageyama, M., Braconnot, P., Harrison, S. P., Lambeck, K., Takahashi, K. et al. (2015). Ice-sheet configuration in the CMIP5/PMIP3 Last Glacial Maximum experiments. *Geosci. Model Dev.*, 8, 36213637.

Argus, D. F., Peltier, W. R., Drummond, R., and Moore, A. W. (2014). The Antarctica component of postglacial rebound model ICE-6G C (VM5a) based on GPS positioning, exposure age dating of ice thicknesses, and relative sea level histories. *Geophysical Journal International*, 198(1), 537-563.

Anderson, J. L., Balaji, V., Broccoli, A. J., Cooke, W. F., Delworth, T. L., Garner, S. T., et al. (2004). The new GFDL global atmosphere and land model AM2LM2: Evaluation with prescribed SST simulations. *Journal of Climate*, 17(24), 4641-4673.

Annan, J. D., and Hargreaves, J. C. (2015). A perspective on model-data surface temperature comparison at the Last Glacial Maximum. *Quaternary Science Reviews*, 107, 1-10.

Blackburn, M., and Hoskins, B. J. (2013). Context and aims of the Aqua-Planet Experiment. *Journal of the Meteorological Society of Japan* Ser. II, 91, 1-15.

Braconnot, P., Otto-Bliesner, B., Harrison, S., Joussaume, S., Peterchmitt, J. Y., Abe-Ouchi, A., Kageyama, M. et al. (2007). Results of PMIP2 coupled simulations of the Mid-Holocene and Last Glacial MaximumPart 1: experiments and large-scale features. *Climate of the Past*, 3(2), 261-277.

Broccoli, A. J., K. A. Dahl, and R. J. Stouffer (2006). Response of the ITCZ to Northern Hemisphere cooling. *Geophysical Research Letters*, 33, L01702.

Buizert, C., et al. in prep. Strongly reduced estimates of Antarctic cooling during the Last Glacial Maximum. Unpublished manuscript.

Ceppi, P., Hwang, Y. T., Liu, X., Frierson, D. M., and Hartmann, D. L. (2013). The relationship between the ITCZ and the Southern Hemispheric eddydriven jet. *Journal of Geophysical Research: Atmospheres*, 118(11), 5136-5146.

Chiang, J., and C. Bitz (2005). Influence of high latitude ice cover on the marine intertropical convergence zone. *Climate Dynamics*, 25 (5), 477496.

Crowley, T. J., and G. R. North (1991). *Paleoclimatology*. New York, NY: Oxford University Press.

Evans, M. N., Tolwinski-Ward, S. E., Thompson, D. M., and Anchukaitis, K. J. (2013). Applications of proxy system modeling in high resolution paleoclimatology. *Quaternary Science Reviews*, 76, 16-28.

Frierson, D., and Y.-T. Hwang (2012). Extratropical influence on ITCZ shifts in slab ocean simulations of global warming. *Journal of Climate*, 25, 720733.

Fudge, T. J., Steig, E. J., Markle, B. R., Schoenemann, S. W., Ding, Q., Taylor, K. C., Alley, R. B. et al. (2013). Onset of deglacial warming in West Antarctica driven by local orbital forcing. *Nature*, 500(7463), 440-444.

Gallee, H., Van Yperselb, J. P., Fichefet, T., Marsiat, I., Tricot, C., and Berger, A. (1992). Simulation of the last glacial cycle by a coupled, sectorially averaged climateice sheet model: 2. Response to insolation and CO2 variations. *Journal of Geophysical Research: Atmospheres*, 97(D14), 15713-15740.

Genthon, G., Barnola, J. M., Raynaud, D., Lorius, C., Jouzel, J., Barkov, N. I., Kotlyakov, V. M. et al. (1987). Vostok ice core: climatic response to CO2 and orbital forcing changes over the last climatic cycle. *Nature*, 329(6138), 414.

Hahn, L., Armour, K., Battisti, D., Pauling, A., Donohoe, A., and Bitz, C. M. (2019, December). Understanding Asymmetries in Arctic and Antarctic Lapse-Rate Feedbacks and Polar Amplification. In AGU Fall Meeting 2019. AGU.

Hall, B. L., Denton, G. H., Heath, S. L., Jackson, M. S., and Koffman, T. N. (2015). Accumulation and marine forcing of ice dynamics in the western Ross Sea during the last deglaciation. *Nature Geoscience*, 8(8), 625-628.

Hamon, N., Sepulchre, P., Donnadieu, Y., Henrot, A. J., Franois, L., Jaeger, J. J., and Ramstein, G. (2012). Growth of subtropical forests in Miocene Europe: The roles of carbon dioxide and Antarctic ice volume. *Geology*, 40(6), 567-570.

Hays, J. D., Imbrie, J., and Shackleton, N. J. (1976). Variations in the Earths orbit: pacemaker of the ice ages. *Science*, 194(4270), 1121-1132.

Held, I. M. (2005). The gap between simulation and understanding in climate modeling. *Bulletin of the American Meteorological Society*, 86(11), 1609-1614.

Hoskins, B. J. (1983). Dynamical processes in the atmosphere and the use of models. *Quarterly Journal of the Royal Meteorological Society*, 109(459), 121.

Jouzel, J., Vimeux, F., Caillon, N., Delaygue, G., Hoffmann, G., MassonDelmotte, V., and Parrenin, F. (2003). Magnitude of isotope/temperature scaling for interpretation of central Antarctic ice cores. *Journal of Geophysical Research: Atmospheres*, 108(D12).

Justino, F., and Peltier, W. R. (2006). Influence of present day and glacial surface conditions on the Antarctic Oscillation/Southern Annular Mode. *Geophysical Research Letters*, 33(22).

Justino, F., Marengo, J., Kucharski, F., Stordal, F., Machado, J., and Rodrigues, M. (2014). Influence of Antarctic ice sheet lowering on the Southern Hemisphere climate: modeling experiments mimicking the mid-Miocene. *Climate Dynamics*, 42(3-4), 843-858.

Justino, F., Silva, A. S., Pereira, M. P., Stordal, F., Lindemann, D., and Kucharski, F. (2015). The large-scale climate in response to the retreat of the West Antarctic Ice Sheet. *Journal of Climate*, 28(2), 637-650.

Kageyama, M., and Valdes, P. J. (2000). Impact of the North American icesheet orography on the Last Glacial Maximum eddies and snowfall. *Geophysical Research Letters*, 27(10), 1515-1518.

Kahle, E. C., et al. in prep. A Statistical Inverse Approach to Reconstruct Temperature, Accumulation Rate, and Layer Thinning from Measured Properties of the South Pole Ice Core. Unpublished manuscript.

Kang, S. M., Held, I. M., Frierson, D. M., and Zhao, M. (2008). The response of the ITCZ to extratropical thermal forcing: Idealized slab-ocean experiments with a GCM. *Journal of Climate*, 21(14), 3521-3532.

Knorr, G., and Lohmann, G. (2014). Climate warming during Antarctic ice sheet expansion at the Middle Miocene transition. *Nature Geoscience*, 7(5), 376.

Lambeck, K., Rouby, H., Purcell, A., Sun, Y., and Sambridge, M. (2014). Sea level and global ice volumes from the Last Glacial Maximum to the Holocene. *Proceedings of the National Academy of Sciences*, 111(43), 15296-15303.

Lorius, C., Jouzel, J., Raynaud, D., Hansen, J., and Le Treut, H. (1990). The ice-core record: climate sensitivity and future greenhouse warming. *Nature*, 347(6289), 139.

Loutre, M. F., and Berger, A. (2000). No glacialinterglacial cycle in the ice volume simulated under a constant astronomical forcing and a variable CO2. *Geophysical Research Letters*, 27(6), 783-786.

Manabe, S., and Broccoli, A. J. (1985). A comparison of climate model sensitivity with data from the last glacial maximum. *Journal of the Atmospheric Sciences*, 42(23), 2643-2651.

Manabe, S., and Wetherald, R. T. (1975). The effects of doubling the CO2 concentration on the climate of a general circulation model. *Journal of the Atmospheric Sciences*, 32(1), 3-15.

Markle, B. R. (2017). Climate dynamics revealed in ice cores: advances in techniques, theory, and interpretation (Doctoral dissertation).

Markle, B.R. and Steig, E.J., Improving temperature reconstructions from ice-core water-isotope records. *Climate of the Past*, Unpublished manuscript.

Masson-Delmotte, V., Kageyama, M., Braconnot, P., Charbit, S., Krinner, G., Ritz, C., and Gladstone, R. M. et al. (2006). Past and future polar amplification of climate change: climate model intercomparisons and ice-core constraints. *Climate Dynamics*, 26(5), 513-529.

Masson-Delmotte, V., M. Schulz, A. Abe-Ouchi, J. Beer, A. Ganopolski, J.F. Gonzalez Rouco, E. Jansen, K. Lambeck, J. Luterbacher, T. Naish, T. Osborn, B. Otto-Bliesner, T. Quinn, R. Ramesh, M. Rojas, X. Shao and A. Timmermann (2013). Information from Paleoclimate Archives. In: Climate Change 2013: The Physical Science Basis. Contribution of Working Group I to the Fifth Assessment Report of the Intergovernmental Panel on Climate Change [Stocker, T.F., D. Qin, G.-K. Plattner, M. Tignor, S.K. Allen, J. Boschung, A. Nauels, Y. Xia, V. Bex and P.M. Midgley (eds.)]. *Cambridge University Press*, Cambridge, United Kingdom and New York, NY, USA.

Mechoso, C., (1981). Topographic influences on the general circulation of the Southern Hemisphere: A numerical experiment. *Monthly Weather Review*, 109, 21312139.

Milankovitch, M. (1941). Canon of Insolation and the Ice Age Problem. *Royal Serbian Academy Special Publication* 133, Belgrade. [Translated by Israel Program for Scientific Translation, Jerusalem, 1969]

Ogura, T., and A. Abe-Ouchi, (2001). Influence of the Antarctic ice sheet on souther high latitude climate during the Cenozoic: albedo vs topography effect. *Geophysical Research Letters*, 28 (4), 587590.

Parish, T., and K. I. Waight (1987). The forcing of Antarctic katabatic winds. *Monthly Weather Review*, 115, 22142226.

Peltier, W. R., Argus, D. F., and Drummond, R. (2015). Space geodesy constrains ice age terminal deglaciation: The global ICE6G C (VM5a) model. *Journal of Geophysical Research: Solid Earth*, 120(1), 450-487.

Pithan, F., and Mauritsen, T. (2014). Arctic amplification dominated by temperature feedbacks in contemporary climate models. *Nature Geoscience*, 7(3), 181-184.

Quintanar, A., and C. Mechoso (1995). Quasi-stationary waves in the southern hemisphere. Part ii: Generation mechanisms. *Journal of the Atmospheric Sciences*, 8, 26732690.

Salzmann, M. (2017). The polar amplification asymmetry: role of Antarctic surface height. *Earth System Dynamics*, 8(2), 323-336.

Simmonds, I., and R. Law (1995). Associations between Antarctic katabatic flow and the upper level winter vortex. *International Journal of Climatology*, 15 (4), 403421.

Singh, H. K., Bitz, C. M., and Frierson, D. M. (2016). The global climate response to lowering surface orography of Antarctica and the importance of atmosphereocean coupling. *Journal of Climate*, 29(11), 4137-4153.

Singh, H. A., Rasch, P. J., and Rose, B. E. J. (2017). Increased ocean heat convergence into the high latitudes with CO2 doubling enhances polar-amplified warming. *Geophysical Research Letters*, 44, 10,58310,591.

Sokolov, S., and Rintoul, S. R. (2009). Circumpolar structure and distribution of the Antarctic Circumpolar Current fronts: 1. Mean circumpolar paths. *Journal of Geophysical Research: Oceans*, 114(C11).

Steig, E. J., Schneider, D. P., Rutherford, S. D., Mann, M. E., Comiso, J. C., and Shindell, D. T. (2009). Warming of the Antarctic ice-sheet surface since the 1957 International Geophysical Year. *Nature*, 457(7228), 459-462.

Steig, E. J., Huybers, K., Singh, H. A., Steiger, N. J., Ding, Q., Frierson, D. M., White, J. W. et al. (2015). Influence of West Antarctic ice sheet collapse on Antarctic surface climate. *Geophysical Research Letters*, 42(12), 4862-4868.

Stenni, B., Jouzel, J., Masson-Delmotte, V., Rthlisberger, R., Castellano, E., Cattani, O., Selmo, E. et al. (2003). A late-glacial high-resolution site and source temperature record derived from the EPICA Dome C isotope records (East Antarctica). *Earth and Planetary Science Letters*, 217(1-2), 183-195.

Taylor, J. P., Edwards, J. M., Glew, M. D., Hignett, P., and Slingo, A. (1996). Studies with a flexible new radiation code. II: Comparisons with aircraft shortwave observations. *Quarterly Journal of the Royal Meteorological Society*, 122(532), 839-861.

Thompson, D. W., and Solomon, S. (2002). Interpretation of recent Southern Hemisphere climate change. *Science*, 296(5569), 895-899.

Thompson, D. W., and Solomon, S. (2009). Understanding recent stratospheric climate change. *Journal of Climate*, 22(8), 1934-1943.

Walsh, K., I. Simmonds, and M. Collier (2000). Sigma-coordinate calculation of topographically forced baroclinicity around Antarctica. *Dynamics of Atmospheres and Oceans*, 33, 129.

Wallace, J. M., and Hobbs, P. V. (2006). Atmospheric science: an introductory survey (Vol. 92). Elsevier.

Appendix A

DERIVATIONS RELEVANT FOR UNDERSTANDING WATER-ISOTOPE DIFFUSION IN ICE-CORE RECORDS

Emma Carolyn Kahle

A.1 Introduction

Water-isotope diffusion in the firn is driven by processes that have long been established in the literature (Johnsen, 1977; Whillans and Grootes, 1985; Cuffey and Steig, 1998; Johnsen et al., 2000). Diffusion processes are characterized by underlying equations fundamental to the fields of physics and mathematics, first described in the early 19^{th} century. Perhaps because these theories are so widely accepted, detailed descriptions of the math involved are somewhat sparse in the water-isotope literature. As a result, it is difficult to find an overview that derives all the math and physics related to water-isotope diffusion. My goal in this Appendix is to create a comprehensive resource that compiles different mathematical approaches to the equations found throughout the water-isotope diffusion literature. The work below is not novel, but is an important synthesis of the existing mathematical theory. Additionally, the multiple approaches considered below lead to deeper understanding of the underlying physical processes behind all of the math.

A.2 Derivations of Water-Isotope Diffusivity

Water-isotope diffusivity describes the rate at which water molecules in the vapor phase spread through the interconnected air-pathways of the firn. This rate depends on several factors, including the saturation vapor pressure, the fractionation factor for the particular water-isotope ratio, and the shape and density of the firn. Both Whillans and Grootes (1985) and Johnsen et al. (2000) show how these factors are related through derivations of the diffusivity, but each paper takes a different approach. I fully describe each approach and compare the final formulations.

A.2.1 The Whillans and Grootes (1985) Approach

Whillans and Grootes (1985) (hereafter WG1985) derive an expression for the diffusivity in a mathematically rigorous way by writing the continuity equation in terms of δ values and firn densities. Note that in this derivation WG1985 do not differentiate between the heavy isotopes, O^{18} and D. Throughout these diffusivity derivations, subscripts v and s refer to the vapor and the solid phase and prime notation refers to the heavy isotopic species.

WG1985 start with the flux of molecules based on Fick's Law for diffusion. Vapor diffusion in the vertical direction z is described by the flux F of molecules of an isotopic species:

$$F = -D_f \frac{\partial n'_v}{\partial z}, \tag{A.1}$$

where D_f is the diffusivity in the firn and n'_v is the concentration of the heavy isotopic species in vapor.

The diffusivity in free air is a simple function of temperature, $D_a = D_a(T)$. Since firn is not free air, we account for the porosity ϕ as:

$$\phi = \left(1 - \frac{\rho_{firn}}{\rho_c}\right), \tag{A.2}$$

where ρ_c is the density of impermeable firn. WG1985 give two potential choices for the definition of ρ_c: 1) the density of bubble-free ice 0.92 Mg/m^{-3}, and 2) the density of pore close-off 0.83 Mg/m^{-3}. WG1985 choose the close-off density because after pores close off, air can no longer diffuse. Accounting for this porosity, diffusivity in the firn is:

$$\begin{aligned} D_f &= D_a\,\phi \\ D_f &= D_a\left(1 - \frac{\rho_{firn}}{\rho_c}\right). \end{aligned} \tag{A.3}$$

Note that WG1985 do not consider how constricted pore space interferes with free vapor motion.

The continuity equation relates the flux to the concentration of heavy isotopes throughout the firn:

$$\frac{dn'_f}{dt} = -\nabla \cdot F = -\frac{\partial F}{\partial z}, \tag{A.4}$$

where n'_f is the concentration in all the firn (solid and vapor), though the vast majority of molecules are in solid ice. We assume that molecule exchange between the solid and vapor phases is rapid and not rate-limiting.

Combining Equations A.1, A.2, A.3, and A.4, we get the standard form of the diffusion equation:

$$\frac{dn'_f}{dt} = -\frac{\partial}{\partial z}\left[-D_a\left(1 - \frac{\rho_f}{\rho_c}\right)\frac{\partial n'_v}{\partial z}\right]. \tag{A.5}$$

Now we need to write n'_f and n'_v in terms of δ values and firn densities. First, we define the isotope ratio δ as:

$$\delta = \frac{n'/n - S}{S}, \tag{A.6}$$

where n is the concentration of the light isotope (^1H or ^{16}O) and S is the standard ratio. We rearrange to get a relationship between the concentrations of heavy and light isotopes:

$$
\begin{aligned}
S\delta &= n'/n - S \\
S\delta + S &= n'/n \\
n(S\delta + S) &= n' \\
nS(1+\delta) &= n'.
\end{aligned} \tag{A.7}
$$

We find an expression for n_v from the ideal gas law:

$$n_v = \frac{p_{sat}}{RT}, \tag{A.8}$$

where n_v is the number of molecules per unit volume, p_{sat} is the saturation vapor pressure over ice, and R is the gas constant.

The concentration of heavy and light isotopes in the total firn is the sum:

$$n'_f + n_f = \frac{\rho_f}{m} + (n'_v + n_v), \tag{A.9}$$

where m is the molecular mass of water. This sum accounts for all isotopes, heavy and light, in both the solid and vapor phases. n_f dominates because $n_f \gg n'_f$ and $n_f \gg n_v$. Thus Equation A.9 simplifies to:

$$n_f \approx \frac{\rho_f}{m}. \tag{A.10}$$

The isotope ratio δ_v in the vapor phase is lower than that in ice because lighter isotopes will preferentially sublimate. This offset can be written as:

$$\Delta\delta = \delta_f - \delta_v$$
$$\delta_v = \delta_f - \Delta\delta. \tag{A.11}$$

Combining Equations A.7, A.8, A.10, and A.11 into expressions for n'_f and n'_v in terms of δ_f and $\Delta\delta$, we get:

$$n'_f = n_f\, S(1+\delta_f)$$
$$n'_f = \frac{\rho_f}{m} S(1+\delta_f) \tag{A.12}$$

$$n'_v = n_v\, S(1+\delta_v)$$
$$n'_v = \frac{p_{sat}\, S}{R\, T}(1+\delta_f-\Delta\delta). \tag{A.13}$$

We now rewrite Equation A.5 in terms of A.12 and A.13 as:

$$\frac{d}{dt}\left[\frac{\rho_f\, S}{m}\,(1+\delta_f)\right] = -\frac{\partial}{\partial z}\left[-D_a\left(1-\frac{\rho_f}{\rho_c}\right)\frac{\partial}{\partial z}\left(\frac{p_{sat} S}{RT}\,(1+\delta_f-\Delta\delta)\right)\right]. \tag{A.14}$$

Canceling out the standard ratio S and rewriting with the product rule:

$$(1+\delta_f)\,\frac{d\rho_f}{dt} + \rho_f \frac{d\delta_f}{dt} = \frac{m}{R}\frac{\partial}{\partial z}\left[D_a\left(1-\frac{\rho_f}{\rho_c}\right)\frac{\partial}{\partial z}\left(\frac{p_{sat}}{T}\,(1+\delta_f-\Delta\delta)\right)\right]. \tag{A.15}$$

We are not interested in $\frac{d\rho_f}{dt}$, so we subtract that term from both sides. To do so, we need to figure out what $(1+\delta_f)\frac{d\rho_f}{dt}$ is equal to on the right hand side of Equation A.15. We write an expression for $\frac{d\rho_f}{dt}$ from Equations A.5, A.8, and A.10.

$$\begin{aligned}
\frac{d\rho_f}{dt} &= \frac{d(mn_f)}{dt} \\
&= m\frac{dn_f}{dt} \\
&= m\frac{\partial}{\partial z}\left[D_a\left(1-\frac{\rho_f}{\rho_c}\right)\frac{\partial}{\partial z}\left(\frac{p_{sat}}{RT}\right)\right] \\
&= \frac{m}{R}\frac{\partial}{\partial z}\left[D_a\left(1-\frac{\rho_f}{\rho_c}\right)\frac{\partial}{\partial z}\left(\frac{p_{sat}}{T}\right)\right]. \qquad \text{(A.16)}
\end{aligned}$$

We multiply by a factor of $(1+\delta_f)$:

$$(1+\delta_f)\frac{d\rho_f}{dt} = (1+\delta_f)\frac{m}{R}\frac{\partial}{\partial z}\left[D_a\left(1-\frac{\rho_f}{\rho_c}\right)\frac{\partial}{\partial z}\left(\frac{p_{sat}}{T}\right)\right]. \qquad \text{(A.17)}$$

To simplify the following equations, we define $\omega = D_a\left(1-\frac{\rho_f}{\rho_c}\right)$.

Now we subtract Equation A.17 from A.15:

$$\begin{aligned}
&\left[(1+\delta_f)\frac{d\rho_f}{dt} + \rho_f\frac{d\delta_f}{dt}\right] - \left[(1+\delta_f)\frac{d\rho_f}{dt}\right] \qquad \text{(A.18)} \\
= \;& \frac{m}{R}\left[\frac{\partial}{\partial z}\left(\omega\frac{\partial}{\partial z}\left[\frac{p_{sat}}{T}(1+\delta_f-\Delta\delta)\right]\right) - (1+\delta_f)\frac{\partial}{\partial z}\left[\omega\frac{\partial}{\partial z}\left(\frac{p_{sat}}{T}\right)\right]\right],
\end{aligned}$$

which simplifies to:

$$\rho_f \frac{d\delta_f}{dt}\frac{R}{m} = \frac{\partial}{\partial z}\left[\omega\frac{\partial}{\partial z}\left(\frac{p_{sat}}{T}\right)+\omega\frac{\partial}{\partial z}\left(\frac{p_{sat}}{T}\delta_f\right)-\omega\frac{\partial}{\partial z}\left(\frac{p_{sat}}{T}\Delta\delta\right)\right]-\frac{\partial}{\partial z}\left[\omega\frac{\partial}{\partial z}\left(\frac{p_{sat}}{T}\right)\right]-\delta_f\frac{\partial}{\partial z}\left[\omega\frac{\partial}{\partial z}\left(\frac{p_{sat}}{T}\right)\right] \quad (A.19)$$

$$= \frac{\partial}{\partial z}\left[\omega\frac{\partial}{\partial z}\left(\frac{p_{sat}}{T}\right)+\frac{\omega p_{sat}}{T}\frac{\partial}{\partial z}\delta_f+\omega\delta_f\frac{\partial}{\partial z}\left(\frac{p_{sat}}{T}\right)-\frac{\omega p_{sat}}{T}\frac{\partial}{\partial z}\Delta\delta-\omega\Delta\delta\frac{\partial}{\partial z}\left(\frac{p_{sat}}{T}\right)\right]$$
$$-\omega\frac{\partial^2}{\partial z^2}\left(\frac{p_{sat}}{T}\right)-\frac{\partial}{\partial z}\omega\frac{\partial}{\partial z}\left(\frac{p_{sat}}{T}\right)-\omega\delta_f\frac{\partial^2}{\partial z^2}\left(\frac{p_{sat}}{T}\right)-\delta_f\frac{\partial}{\partial z}\omega\frac{\partial}{\partial z}\left(\frac{p_{sat}}{T}\right) \quad (A.20)$$

$$= \frac{\omega p_{sat}}{T}\frac{\partial^2}{\partial z^2}\delta_f+\frac{\partial}{\partial z}\frac{\omega p_{sat}}{T}\frac{\partial}{\partial z}\delta_f+\frac{\partial}{\partial z}\left(\omega\delta_f\right)\frac{\partial}{\partial z}\left(\frac{p_{sat}}{T}\right)-\frac{\omega p_{sat}}{T}\frac{\partial^2}{\partial z^2}\Delta\delta-\frac{\partial}{\partial z}\frac{\omega p_{sat}}{T}\frac{\partial}{\partial z}\Delta\delta$$
$$-\omega\Delta\delta\frac{\partial^2}{\partial z^2}\left(\frac{p_{sat}}{T}\right)-\frac{\partial}{\partial z}(\omega\Delta\delta)\frac{\partial}{\partial z}\left(\frac{p_{sat}}{T}\right)-\delta_f\frac{\partial}{\partial z}\omega\frac{\partial}{\partial z}\left(\frac{p_{sat}}{T}\right) \quad (A.21)$$

$$= \frac{\partial}{\partial z}\left(\frac{\omega p_{sat}}{T}\frac{\partial}{\partial z}\delta_f\right)+\frac{\partial}{\partial z}\left(\frac{p_{sat}}{T}\right)\left[\frac{\partial}{\partial z}(\omega\delta_f)-\delta_f\frac{\partial}{\partial z}\omega\right]-\frac{\partial}{\partial z}\left(\frac{\omega p_{sat}}{T}\frac{\partial}{\partial z}\Delta\delta\right)-\omega\Delta\delta\frac{\partial^2}{\partial z^2}\left(\frac{p_{sat}}{T}\right)$$
$$-\frac{\partial}{\partial z}\left(\frac{p_{sat}}{T}\right)\left(\omega\frac{\partial}{\partial z}\Delta\delta+\Delta\delta\frac{\partial}{\partial z}\omega\right) \quad (A.22)$$

$$= \frac{\partial}{\partial z}\left[\frac{\omega p_{sat}}{T}\frac{\partial}{\partial z}\delta_f\right]-\frac{\partial}{\partial z}\left[\frac{\omega p_{sat}}{T}\frac{\partial}{\partial z}\Delta\delta\right]+\frac{\partial}{\partial z}\left(\frac{p_{sat}}{T}\right)\left[\omega\frac{\partial}{\partial z}\delta_f+\delta_f\frac{\partial}{\partial z}\omega-\delta_f\frac{\partial}{\partial z}\omega\right]-\omega\frac{\partial}{\partial z}\left(\frac{p_{sat}}{T}\right)\frac{\partial}{\partial z}\Delta\delta$$
$$-\omega\Delta\delta\frac{\partial^2}{\partial z^2}\left(\frac{p_{sat}}{T}\right)-\Delta\delta\frac{\partial}{\partial z}\omega\frac{\partial}{\partial z}\left(\frac{p_{sat}}{T}\right)-\omega\frac{\partial}{\partial z}\Delta\delta\frac{\partial}{\partial z}\left(\frac{p_{sat}}{T}\right)+\omega\frac{\partial}{\partial z}\Delta\delta\frac{\partial}{\partial z}\left(\frac{p_{sat}}{T}\right) \quad (A.23)$$

$$= \frac{\partial}{\partial z}\left[\frac{\omega p_{sat}}{T}\frac{\partial}{\partial z}\left(\delta_f-\Delta\delta\right)\right]+\omega\frac{\partial}{\partial z}\left(\frac{p_{sat}}{T}\right)\frac{\partial}{\partial z}\delta_f-\omega\frac{\partial}{\partial z}\left(\frac{p_{sat}}{T}\right)\frac{\partial}{\partial z}\Delta\delta$$
$$-\Delta\delta\left[\omega\frac{\partial^2}{\partial z^2}\left(\frac{p_{sat}}{T}\right)+\frac{\partial}{\partial z}\omega\frac{\partial}{\partial z}\left(\frac{p_{sat}}{T}\right)\right]. \quad (A.24)$$

Terms in Equation A.18 are multiplied out to produce Equation A.19. Then the product rule is applied to get to Equation A.20. Next the product rule is applied again and we subtract terms to get to Equation A.21. Then the reverse product rule and factoring are used to combine terms in Equation A.22. In Equation A.23, the product rule is applied again and a new term $\omega\frac{\partial}{\partial z}\Delta\delta\frac{\partial}{\partial z}\left(\frac{p_{sat}}{T}\right)$ is added and subtracted in different places. To get to Equation A.24, more factoring and canceling of terms.

Finally, more factoring and reverse product rule yields the most simplified version:

$$\begin{aligned}\rho_f\frac{d\delta_f}{dt}\cdot\frac{R}{m} &= \frac{\partial}{\partial z}\left[\frac{\omega\, p_{sat}}{T}\frac{\partial}{\partial z}\left(\delta_f-\Delta\delta\right)\right] \\ &\quad +\omega\left[\frac{\partial}{\partial z}\left(\frac{p_{sat}}{T}\right)\right]\frac{\partial}{\partial z}\left(\delta_f-\Delta\delta\right) \\ &\quad -\Delta\delta\frac{\partial}{\partial z}\left[\omega\frac{\partial}{\partial z}\left(\frac{p_{sat}}{T}\right)\right]. \end{aligned} \tag{A.25}$$

$$\frac{d\delta_f}{dt} = \frac{m}{\rho_f R}\frac{\omega\, p_{sat}}{T}\left[\frac{\partial^2}{\partial z^2}\left(\delta_f-\Delta\delta\right)+0\times\frac{\partial^2}{\partial z^2}\left(\delta_f-\Delta\delta\right)-0\right] \tag{A.26}$$

This expression for $\frac{d\delta_f}{dt}$ can be solved directly by Crank-Nicolson techniques. Alternatively, we can simplify Equation A.25 by assuming that T and ρ do not change with depth. The $\Delta\delta$ in the partial on the right hand side of Equation A.26 goes to zero because it does not depend on depth. We end up with:

$$\frac{d\delta_f}{dt} = \frac{m\, p_{sat}\,\Omega_a}{R\,T}\left(\frac{1}{\rho_f}-\frac{1}{\rho_c}\right)\frac{\partial^2\delta_f}{\partial z^2}. \tag{A.27}$$

Now we have the diffusion equation. To find the WG1985 diffusivity constant D_f, we pick out the term before the second spatial derivative:

$$D_f = \frac{m\, p_{sat}\, D_a}{RT} \left(\frac{1}{\rho_f} - \frac{1}{\rho_c} \right). \tag{A.28}$$

A.2.2 The Johnsen et al. (2000) Approach

Johnsen et al. (2000) (hereafter J2000) derives an expression for the diffusivity in a more conceptual way by considering the residence times of a heavy isotope water molecule ($H_2^{18}O$) in each of the solid and vapor phases. The derivation tracks the heavy isotope as it moves through a firn consisting of mostly light isotopes.

J2000 begins by considering how much time a water molecule spends in the vapor and solid phases. We define terms for the residence times in each phase:

Δt_v = mean time a molecule is freely moving around as vapor (disregarding being temporarily stuck to an ice surface)

Δt_s = mean time a molecule spends deeper in solid ice (not on surface of crystals)

In some ice-core data, we observe that the annual cycle can completely vanish, so we make the assumption that all molecules repeatedly transfer between these two phases. The extent of diffusion experienced by molecules, diffusion length σ will depend on the amount of time spent in the vapor phase:

$$\sigma \propto \Delta t_v. \tag{A.29}$$

Given this relationship, our goal is to find an expression, in terms of firn properties, for the ratio of the time the heavy isotope spends in the vapor phase compared to the time the heavy isotope spends in the solid phase:

$$r \equiv \frac{\Delta t'_v}{\Delta t'_s}. \tag{A.30}$$

To find an expression for r, we must make two assumptions about the firn grains. First, individual firn grains are well-mixed, with constant isotopic composition throughout. Second, firn grains are in isotopic equilibrium with the vapor. Both of these simplifying assumptions are made by WG1985 as well.

The ratio r depends on the reservoir size of each molecules in each phase as well as the transfer rates from one phase to the other. The transfer rates of isotopes into each phase are proportional to the negative concentration of isotopes already in that phase. For example, if the concentration of an isotope in the vapor phase increases, more of those isotopes will move to the solid phase and thus the number of those isotopes in the vapor phase will decrease. Mathematically:

$$\frac{dN'_v}{dt} \propto -n'_v \quad \text{and} \quad \frac{dN'_s}{dt} \propto -n'_s, \tag{A.31}$$

where N is the number isotopes in 1 kg of firn and n is the concentration of isotopes. We can define some constants k'_v and k'_s such that:

$$\frac{dN'_v}{dt} = -k'_v \cdot n'_v \quad \text{and} \quad \frac{dN'_s}{dt} = -k'_s \cdot n'_s. \tag{A.32}$$

Specific pore space volume and specific solid ice volume are defined as:

$$V_p = \frac{1}{\rho_f} - \frac{1}{\rho_{ice}} \quad \text{and} \quad V_s = \frac{1}{\rho_{ice}}, \tag{A.33}$$

where ρ_f is the density of the firn and ρ_{ice} is the density of solid ice. Substituting these volumes in to Equation A.32,

$$\frac{dN'_v}{dt} = -k'_v \cdot \frac{N'_v}{V_p} \quad \text{and} \quad \frac{dN'_s}{dt} = -k'_s \cdot \frac{N'_s}{V_s}. \tag{A.34}$$

The definition of residence time gives:

$$\frac{dN'_v}{dt} = \frac{-N'_v}{\Delta t_v} \quad \text{and} \quad \frac{dN'_s}{dt} = \frac{-N'_s}{\Delta t_s}, \tag{A.35}$$

and in steady-state we can make the assumption that the transfer rates between the phases are the same:

$$\begin{aligned} \frac{dN'_v}{dt} &= \frac{dN'_s}{dt} \\ \frac{-N'_v}{\Delta t_v} &= \frac{-N'_s}{\Delta t_s} \\ \frac{N'_v}{N'_s} &= \frac{\Delta t_v}{\Delta t_s} \\ &= r \ll 1. \end{aligned}$$

By assuming isotopic equilibrium between the vapor and solid phases, we can define the fractionation factor α for the isotopic ratios in water vapor over ice as:

$$\alpha = \frac{N'_s/N_s}{N'_v/N_v}. \tag{A.36}$$

Rearranging,

$$\begin{aligned} \frac{1}{\alpha}\frac{N_s'}{N_s} &= \frac{N_v'}{N_v} \\ \frac{1}{\alpha}\frac{N_v}{N_s} &= \frac{N_v'}{N_s'} \\ &= r. \end{aligned} \tag{A.37}$$

Next we start to relate firn properties to the expression for r. We write the number of molecules in the solid phase of 1 kg of firn, assuming that $N_s' \gg N_v'$ and thus $N_{tot}' \approx N_s'$, as:

$$N_s' = \frac{A_v}{m'} \tag{A.38}$$

where A_v is Avogadro's Number and m' is the molecular mass of a $H_2^{18}O$ water molecule in units of kg mol^{-1}.

We write the number of molecules in the vapor phase N_v' with the ideal gas law:

$$PV = \frac{N_v' R\, T}{N_A}. \tag{A.39}$$

Solving for N_v' and plugging in the values we have defined thus far,

$$N_v' = \frac{A_v\, p_{sat}\, V_p}{R\, T}, \tag{A.40}$$

where p_{sat} is the saturation vapor pressure of $H_2^{16}O$ over ice. With these values we now write r as:

$$\begin{aligned} r = \frac{N_v'}{N_s'} &= \frac{A_v\, p_{sat}\, V_p / R\, T}{A_v / m'} \\ r &= \frac{m'\, p_{sat}\, V_p}{R\, T}. \end{aligned} \tag{A.41}$$

We have now reached an expression for r in terms of properties of the firn.

Next we relate the expression for r to the diffusion length. If we consider the diffusivity of the firn D_f to be constant through the firn, we can write the diffusion length σ as the root-mean-square of the vertical position z of a molecule after some time t as:

$$\begin{aligned} \sigma = \quad \langle z^2 \rangle^{1/2} \quad &= \sqrt{2 D_f t} \\ \sigma^2 = \quad \langle z^2 \rangle \quad &= 2 D_f t. \end{aligned} \tag{A.42}$$

D_f takes into account the time the heavy isotope spends in both vapor and solid phases. The change in the square of its diffusion length depends on the amount of time the molecule will stay in the vapor phase:

$$\Delta\sigma^2 = 2 \frac{D_a}{\tau} \Delta t_v, \tag{A.43}$$

where D_a is the diffusivity of the heavy isotope in free air, and where τ, the tortuosity, accounts for the shape of the air pathways in the pore space. Note that τ is defined by how much molecules are slowed down in their movement through the firn.

Next we divide each side by the residence time in the solid phase:

$$\frac{\Delta\sigma^2}{\Delta t_s} = 2 \frac{D_a}{\tau} \frac{\Delta t_v}{\Delta t_s} \tag{A.44}$$

$$\frac{d\sigma^2}{dt} = 2 D_e r, \tag{A.45}$$

where the effective diffusivity, $D_e = D_a/\tau$, takes into account the tortuosity. During the amount of time Δt_s, most molecules will have also spent the amount of time Δt_v in the pore space, and we assume that $\Delta t_v \ll \Delta t_s$. We can thus say that the left hand side of Equation

A.44 is equal to the total derivative because $dt = \Delta t_s + \Delta t_v \approx \Delta t_s$. Thus we have related the change in diffusion length to our ratio of residence times r.

Equation A.45 relates r to D_e, the diffusivity of the heavy isotope in the vapor phase, but we need it in terms of D_f, the total diffusivity of the firn, including time spent in the solid phase. We can compare the derivative of Equation A.42 with Equation A.45 to see that:

$$\frac{d\sigma^2}{dt} = 2\,D_f = 2\,D_e\,r \tag{A.46}$$

$$D_f = D_e\,r. \tag{A.47}$$

This says that the diffusivity of the total firn is simply the effective diffusivity D_e times the ratio of the time spent in the vapor phase to the time spent in the solid phase, which makes sense intuitively. Now combining our expressions for D_e and r, we can write the firn diffusivity as:

$$D_f = \frac{D_a}{\tau}\frac{1}{\alpha}\frac{m'\,p_{sat}\,V_p}{R\,T}. \tag{A.48}$$

Rearranging slightly and substituting in $V_p = \frac{1}{\rho_f} - \frac{1}{\rho_{ice}}$ from Equation A.33,

$$D_f = \frac{m\,p_{sat}\,D_a}{R\,T\,\alpha\,\tau}\left(\frac{1}{\rho_f} - \frac{1}{\rho_{ice}}\right). \tag{A.49}$$

This is the final J2000 formulation for the diffusivity in entire firn, accounting for the shape of the air pathways as well as the time spent in both the solid and vapor phases.

It is informative to separate this expression into the following terms:

$$D_f = (m')\left(\frac{1}{RT}\right)\left(\frac{p_{sat}}{\alpha}\right)\left(\frac{D_a}{\tau}\right)\left(\frac{1}{\rho_f} - \frac{1}{\rho_{ice}}\right)$$

The m' term accounts for a conversion from mass to number. The $\frac{1}{RT}$ term accounts for a conversion from volume to number. The $\frac{p_{sat}}{\alpha}$ term accounts for the adjustment to the saturation vapor pressure to reflect that of the heavy isotope rather than the light. The $\frac{D_a}{\tau}$ term accounts for the adjustment to the free air diffusivity to reflect that of twisted air channels in the firn. Lastly, the $\frac{1}{\rho_f} - \frac{1}{\rho_{ice}}$ term accounts for the volume of space available for the molecules to diffuse through.

A.2.3 Comparison of Approaches

We compare the final formulations of each paper, Equation A.28 for WG1985 and Equation A.49 for J2000.

The only differences between these formulations are due to the fact that J2000 takes into account both tortuosity of the firn τ and the fractionation factor α. J2000 included tortuosity to account for the shape of airspace (tortuosity) in addition to the extent of airspace (porosity). J2000 also explains that the fractionation factor α can be inserted in WG1985 if it is included in the expression for the isotope offset $\Delta\delta$. Instead of:

$$\Delta\delta = \delta_f - \delta_v \approx \alpha - 1, \tag{A.50}$$

the relationship between δ_f, δ_v, and α can be defined as:

$$(1 + \delta_f) = \alpha(1 + \delta_v). \tag{A.51}$$

After some algebra, using this definition instead will yield α in the same spot in Equation A.28 as in Equation A.49. Thus the J2000 formulation is slightly more accurate because it includes α directly rather than making an approximation.

Here we show how the α term appears in the diffusivity equation. The definitions of δ_f, δ_v, and $\Delta\delta$ can be manipulated and substituted into Equation A.25. Manipulating J2000's definition above yields:

$$\delta_f - \Delta\delta = \delta_v = \frac{1+\delta_f}{\alpha} - 1 \tag{A.52}$$

$$\Delta\delta = \frac{(1+\delta_f)(\alpha-1)}{\alpha}. \tag{A.53}$$

Substitute these expressions into the right side of Equation A.25.

$$\begin{aligned} \rho_f \frac{d\delta_f}{dt} \cdot \frac{R}{m} &= \frac{\partial}{\partial z}\left[\frac{\omega\, p_{sat}}{T}\frac{\partial}{\partial z}\left(\frac{1+\delta_f}{\alpha} - 1\right)\right] \\ &\quad + \omega\left[\frac{\partial}{\partial z}\left(\frac{p_{sat}}{T}\right)\right]\frac{\partial}{\partial z}\left(\frac{1+\delta_f}{\alpha} - 1\right) \\ &\quad - \frac{(1+\delta_f)(\alpha-1)}{\alpha}\frac{\partial}{\partial z}\left[\omega\frac{\partial}{\partial z}\left(\frac{p_{sat}}{T}\right)\right]. \end{aligned} \tag{A.54}$$

When we make the assumption again that temperature does not vary over depth, the second and third terms on the right hand side go to zero, leaving us with:

$$\rho_f \frac{d\delta_f}{dt} \cdot \frac{R}{m} = \frac{\omega\, p_{sat}}{T}\frac{\partial^2}{\partial z^2}\left(\frac{1+\delta_f}{\alpha} - 1\right). \tag{A.55}$$

Rearranging,

$$\begin{aligned} \frac{d\delta_f}{dt} &= \frac{m\,\omega\, p_{sat}}{RT\rho_f}\frac{\partial^2}{\partial z^2}\left(\frac{1+\delta_f-\alpha}{\alpha}\right) \\ \frac{d\delta_f}{dt} &= \frac{m\,\omega\, p_{sat}}{RT\rho_f}\frac{1}{\alpha}\frac{\partial^2}{\partial z^2}\left(1+\delta_f-\alpha\right) \end{aligned} \tag{A.56}$$

The factors of 1 and α in the second spatial derivative go to zero because they do not depend on depth. We can substitute the expression back in for $\omega = D_a(1 - \frac{\rho_f}{\rho_c})$ and divide by ρ_f, leaving us with:

$$\frac{d\delta_f}{dt} = \frac{m\, p_{sat} D_a}{RT\alpha}\left(\frac{1}{\rho_f} - \frac{1}{\rho_c}\right)\frac{\partial^2 \delta_f}{\partial z^2}$$

Picking out the diffusivity coefficient, as before, now includes α in the denominator, equivalent to the J2000 formulation. Furthermore, if tortuosity were taken into account as $D_e = \frac{D_a}{\tau}$, τ would also appear in the denominator and the two formulations would be identical.

Thus we have compared these two different approaches to derivations of the diffusivity of water vapor in the firn. We see that, accounting for tortuosity and fractionation factor, they result in the same expression for diffusivity. The WG1985 approach is a mathematical way to define the diffusion occurring in the firn, through the definition of fluxes of molecules. The J2000 approach avoids working through a differential equation by characterizing the actual mechanisms at work and tracking the heavy isotopes through the processes that move them through the firn.

A.3 Derivations of the Water-Isotope Diffusion Equation

Based on Fick's second law, the basic advection-diffusion equation for isotopes moving through the firn layer of an ice sheet can be written as follows:

$$\frac{\partial \delta}{\partial t} = D\frac{\partial^2 \delta}{\partial z^2} - \dot{\epsilon} z \frac{\partial \delta}{\partial z}, \tag{A.57}$$

where δ is the isotope ratio, D is the diffusivity coefficient, z is the vertical coordinate assuming an origin fixed on a sinking layer of firn, and $\dot{\epsilon}$ is the vertical strain rate. Johnsen (1977) states the solution to this partial differential equation as:

$$\delta(z,t) = \frac{1}{\sigma\sqrt{2\pi}} \int_{-\infty}^{\infty} \delta(z'_{strained}, 0) \exp\left(\frac{-(z-z')^2}{2\sigma^2}\right) dz', \tag{A.58}$$

where the $z_{strained}$ accounts for the cumulative effect of the vertical strain rate $\dot{\epsilon}$:

$$z_{strained} = z\, e^{-\int_0^t \dot{\epsilon_z}(\tau) d\tau}. \tag{A.59}$$

In this section we present two approaches to deriving this solution. The first approach is an analytical derivation starting from the heat equation. the second is a statistical derivation that considers the random-walk process associated with diffusion. Though quite different, both approaches produce the same solution.

A.3.1 Analytical Derivation

This analytical derivation is based on the resources contained within Strang (2006). We start with the heat equation, written in terms of the isotope ratio δ and the diffusivity D:

$$\frac{\partial \delta}{\partial t} = D \frac{\partial^2 \delta}{\partial z^2}. \tag{A.60}$$

We can solve this PDE using the common technique of separation of variables. We assume that the solution $\delta(z,t)$ can be written as the product of two functions, one that depends only on t and one that depends only on z:

$$\delta(z,t) = G(t)E(z). \tag{A.61}$$

We can take derivatives of $\delta(z,t)$ and rewrite Equation A.60 as

$$G'E = GE'' \tag{A.62}$$

$$\frac{G'(t)}{G(t)} = \frac{E''(z)}{E(z)}. \tag{A.63}$$

Since these ratios are equal, they must be equal to some constant, and we can find a family of solutions that will satisfy Equation A.62:

$$E(z) = De^{\imath kz} \quad E''(z) = -Dk^2 e^{\imath kz} \tag{A.64}$$
$$G(t) = e^{-k^2 t} \quad G'(t) = -k^2 e^{-k^2 t}.$$

Using these solutions, we write our solution to Equation A.61 as:

$$\delta(z,t) = De^{\imath kz} e^{-k^2 t}. \tag{A.65}$$

We account for all solutions from all linear combinations by integrating over all k:

$$\delta(z,t) = \frac{1}{2\pi D} \int_{-\infty}^{\infty} \hat{\delta}_0(k) e^{\imath kz} e^{-k^2 t} dk. \tag{A.66}$$

Here $\hat{\delta}_0(k)$ is included to satisfy the initial conditions $\delta(z,0)$ at $t = 0$. We can check Equation A.66 by plugging in this initial condition.

$$\delta(z,0) = \frac{1}{2\pi D} \int_{-\infty}^{\infty} \hat{\delta}_0(k) e^{\imath kz} dk.$$

We compare this expression to the definition of the inverse Fourier transform (Equation A.67) to see that the initial condition $\delta(z,0)$ is satisfied.

$$x(t) = \frac{1}{2\pi D} \int_{-\infty}^{\infty} \hat{x}(\omega) e^{\imath\omega t} d\omega \tag{A.67}$$

With Equation A.66 we have successfully derived the general solution to Equation A.60.

To derive the fundamental solution for a specified initial condition, we first consider an initial condition that is a delta function, or a point source: $\delta(z, 0) = \Delta(z)$ at $t = 0$. This initial condition is convenient because its Fourier transform is $\hat{\delta}_0(k) = 1$.

Plugging this initial condition into Equation A.66 we get:

$$\delta(z, t) = \frac{1}{2\pi D} \int_{-\infty}^{\infty} e^{\imath kz} e^{-k^2 t} dk. \tag{A.68}$$

Next we take the partial derivative with respect to z of both sides:

$$\frac{\partial \delta}{\partial z} = \frac{1}{2\pi D} \int_{-\infty}^{\infty} \imath k e^{\imath kz} e^{-k^2 t} dk. \tag{A.69}$$

We rearrange to separate for integration by parts:

$$\frac{\partial \delta}{\partial z} = \frac{1}{2\pi D} \int_{-\infty}^{\infty} \left(\imath e^{\imath kz}\right) \left(k e^{-k^2 t}\right) dk. \tag{A.70}$$

With compute the integration by parts with:

$$\begin{aligned} u &= \imath e^{\imath kz} & v &= -\frac{1}{2t} e^{-k^2 t} \\ \tfrac{du}{dk} &= -z e^{\imath kz} & \frac{dv}{dk} &= k e^{-k^2 t}. \end{aligned}$$

Applying integration by parts, we get:

$$\frac{\partial \delta}{\partial z} = \frac{1}{2\pi D}\left[\left(-\imath e^{\imath kz}\frac{1}{2t}e^{-k^2}\right)_{-\infty}^{\infty} - \int_{-\infty}^{\infty}\frac{1}{2t}e^{-k^2 t}ze^{\imath kz}dk\right]. \tag{A.71}$$

The term on the left inside the square brackets goes to zero when evaluated from $-\infty$ to ∞, and we are left with:

$$\frac{\partial \delta}{\partial z} = -\frac{1}{4\pi tD}\int_{-\infty}^{\infty} e^{-k^2 t}ze^{\imath kz}dk. \tag{A.72}$$

We compare Equation A.72 to the expression for $\delta(z,t)$ in Equation A.68 to see the simple result:

$$\frac{\partial \delta}{\partial z} = -\frac{z\delta}{2t}. \tag{A.73}$$

This is a linear ODE that is solved by:

$$\delta = ce^{-z^2/4tD}. \tag{A.74}$$

We can solve for c based on conservation of the initial condition through time:

$$\begin{aligned}\int_{-\infty}^{\infty}\delta(z,t)dz &= \int_{-\infty}^{\infty}\delta(z,0)dz \\ &= \int_{-\infty}^{\infty}\Delta(z)dz \\ &= 1.\end{aligned}$$

We apply this conservation criterion to solve for c:

$$\int_{-\infty}^{\infty} ce^{-z^2/4tD}dz = 1 \tag{A.75}$$

$$c = \frac{1}{\int_{-\infty}^{\infty} e^{-z^2/4tD}dz}. \tag{A.76}$$

We recognize the denominator as the integral of a Gaussian, whose solution is known:

$$\int_{-\infty}^{\infty} e^{-ax^2}dx = \sqrt{\frac{\pi}{a}}.$$

In our case, $a = \frac{1}{4tD}$, and thus we can solve for c as:

$$c = \frac{1}{\sqrt{4tD\pi}}. \tag{A.77}$$

Now our solution to Equation A.74 can be written as:

$$\delta(z,t) = \frac{1}{\sqrt{4\pi tD}}e^{-z^2/4tD}. \tag{A.78}$$

This is the fundamental solution from a point source (recall that our initial condition used in this solution was a delta function). To build up to an initial condition of continuous spatial extent, we next consider the possibility that our initial condition delta function $\Delta(z)$ is located a different point $z = z'$, such that:

$$\delta(z,0) = \Delta(z - z') \quad \text{at} \quad t = 0.$$

Now argument of the exponential in our solution shifts by z':

$$e^{-z^2/4tD} \quad \text{becomes} \quad e^{-(z-z')^2/4tD}.$$

Any initial condition $\delta(z,0)$ can be written as the combination of point sources at many locations z', and we can linearly combine all initial conditions with:

$$\delta(z,0) = \int_{all\ Z} \Delta(z-z')\delta(z',0)dz'.$$

The solution for an initial condition extending over all points in z can be written as an integral of the responses to $\Delta(z-z')$:

$$\delta(z,t) = \frac{1}{\sqrt{4\pi tD}} \int_{-\infty}^{\infty} \delta(z',0) \exp\left(\frac{-(z-z')^2}{4tD}\right) dz'. \tag{A.79}$$

With $\sigma = \sqrt{2Dt}$, we have:

$$\delta(z,t) = \frac{1}{\sigma\sqrt{2\pi}} \int_{-\infty}^{\infty} \delta(z',0) \exp\left(\frac{-(z-z')^2}{2\sigma^2}\right) dz', \tag{A.80}$$

identical to the solution in Johnsen (1977) before $z_{strained}$ accounts for the advection.

A.3.2 Statistical Derivation

Lasaga (2014) derives the same solution through a statistical framework, using the idea of a discrete random walk. A particle starts at $z = 0$ and at each time step can move a distance L either upwards with probability p or downwards with probability $q = 1 - p$. We would like

to know what the probability is that after N steps the particle is at some position $z = mL$, where $-N \leq m \leq N$.

We denote the number of steps the particle takes upwards, n_U, and the number of steps the particle takes downwards, n_D. We write:

$$N = n_U + n_D \tag{A.81}$$

$$m = n_U - n_D, \tag{A.82}$$

and thus:

$$n_U = \frac{1}{2}(N + m) \tag{A.83}$$

$$n_D = \frac{1}{2}(N - m). \tag{A.84}$$

We write the probability $P_N(m)$ of arriving at position $z = mL$ after N steps as the product of the probability of taking a particular sequence of steps to that position, $p^{n_U}q^{n_D}$, times the number of different sequences of steps that will end at that position (because multiple sequences of steps will end at the same z position, i.e. UUUD, UUDU, UDUU, and DUUU all end at $m = 2$):

$$P_N(m) = p^{n_U}q^{n_D}\frac{N!}{n_U!n_D!}. \tag{A.85}$$

Plugging in Equations A.83 and A.84, we get:

$$P_N(m) = \frac{N!}{[\frac{1}{2}(N+m)]![\frac{1}{2}(N-m)]!}p^{n_U}q^{n_D}. \tag{A.86}$$

We now make a couple of assumptions to simplify Equation A.86. First, we can assume that $p = q = \frac{1}{2}$, that the particle is equally likely to step up or down. Second, we assume that the particle has taken many steps ($N \gg 1$) and that the number of steps taken is much greater than the distance from the starting point ($N \gg m$). With these assumptions, we can use Stirling's Approximation:

$$\ln n! = n \ln n - n + \frac{1}{2} \ln n + \frac{1}{2} \ln 2\pi$$

We rewrite Equation A.86 with this approximation and set $p = q = \frac{1}{2}$ to get:

$$\begin{aligned} \ln P_N(m) &= N \ln N - \frac{1}{2}(N+m) \ln[\frac{1}{2}(N+m)] \\ &\quad -\frac{1}{2}(N-m) \ln[\frac{1}{2}(N-m)] + \frac{1}{2} \ln N - \frac{1}{2} \ln[\frac{1}{2}(N+m)] \\ &\quad -\frac{1}{2} \ln[\frac{1}{2}(N-m)] - \frac{1}{2} \ln(2\pi) + N \ln \frac{1}{2}, \end{aligned} \tag{A.87}$$

which simplifies to:

$$\begin{aligned} \ln(N+m) &= \ln \left[N \left(1 + \frac{m}{N} \right) \right] \\ &= \ln N + \ln \left(1 + \frac{m}{N} \right) \end{aligned} \tag{A.88}$$

For small x, we can use the assumption that:

$$\ln(1+x) \sim x - \frac{1}{2}x^2,$$

and thus,

$$\ln\left(1+\frac{m}{N}\right)=\frac{m}{N}-\frac{1}{2}\frac{m^2}{N^2}. \tag{A.89}$$

So, Equation A.88 becomes:

$$\ln(N+m)=\ln N+\frac{m}{N}-\frac{1}{2}\frac{m^2}{N^2}, \tag{A.90}$$

and, similarly,

$$\ln(N-m)=\ln N-\frac{m}{N}-\frac{1}{2}\frac{m^2}{N^2}. \tag{A.91}$$

Plugging Equations A.90 and A.91 into Equation A.87 and simplifying, we get:

$$\ln P_N(m)=-\frac{1}{2}\ln N+\frac{1}{2}\ln 2-\frac{1}{2}\ln\pi-\frac{m^2}{2N}+\frac{m^2}{2N^2}. \tag{A.92}$$

Neglecting the term of order $\frac{1}{N^2}$ and combining the remaining terms leaves us with:

$$P_N(m)=\left(\frac{1}{\pi N}\right)^{1/2}e^{-m^2/2N}. \tag{A.93}$$

Equation A.93 shows the result expected from diffusion from a point source, based only on the assumptions of a random walk and of many time steps. However, this equation describes the discrete probability of the particle taking steps of size L. To get an expression for the continuous probability $W(z,t)$ that the particle will be at any point z at time t, we must generalize m to z and N to t.

We define the relations:

$$z = mL \tag{A.94}$$

$$N = vt, \tag{A.95}$$

where v is the frequency of steps.

Because the particle can only reach an even numbered position at an even time step or an odd numbered position at an odd time step (i.e. N and m are either both even or both odd), $P_N(m)$ is the discrete probability of the particle being anywhere between $z = mL$ and $z = (m+2)L$. Thus the discrete probability can be related to the continuous probability as:

$$P_N(m) = W(z,t)2L. \tag{A.96}$$

Using this relation and plugging in known expressions:

$$\begin{aligned} W(z,t) &= \frac{P_N(m)}{2L} \\ &= \frac{1}{2L}\left(\frac{2}{\pi N}\right)^{1/2} e^{-(m^2/2N)} \\ &= \frac{1}{2L}\left(\frac{2}{\pi vt}\right)^{1/2} e^{-[(m^2/L^2)/2vt]} \\ &= \frac{1}{(2\pi L^2 vt)^{1/2}} e^{-(z^2/2vL^2t)}. \end{aligned} \tag{A.97}$$

And with the definition $D \equiv \frac{1}{2}vL^2$,

$$W(z,t) = \frac{1}{2\sqrt{\pi Dt}} e^{-(z^2/4Dt)}. \tag{A.98}$$

We now have an expression for the continuous probability of particles originating from a point source diffusing to a particular point at a particular time. However, we want the

solution for a continuous source with spatial extent. Because the diffusion equation is linear, it obeys the law of superposition, and we can generalize our point source solution by treating a continuous source as the sum of individual source slabs of arbitrarily small width dz.

If our point of interest is located at z and one of the slabs making up the continuous source is located at z', we can write the contribution of this single slab to the concentration of particles at point z as:

$$\delta(z,t) = \frac{\delta(z',0)}{2\sqrt{\pi D t}} \exp\left(-\frac{(z-z')^2}{4Dt}\right) dz' \tag{A.99}$$

where $\delta(z',0)$ is the initial concentration at point z.

We sum the contributions from all the slabs making up the continuous source by integrating the above equation over the entire source. For a source of infinite extent we get:

$$\delta(z,t) = \int_{-\infty}^{\infty} \frac{\delta(z',0)}{2\sqrt{\pi D t}} \exp\left(\frac{-(z-z')^2}{4Dt}\right) dz' \tag{A.100}$$

Defining the diffusion length $\sigma = \sqrt{2Dt}$, we again are left with the solution to the same solution as in Johnsen (1977) before $z_{strained}$ accounts for the advection:

$$\delta(z,t) = \frac{1}{\sigma\sqrt{2\pi}} \int_{-\infty}^{\infty} \delta(z',0) \exp\left(\frac{-(z-z')^2}{2\sigma^2}\right) dz' \tag{A.101}$$

A.4 Water-Isotope Diffusion Length

The diffusion length σ can also be derived using a statistical approach (Lasaga, 2014). We start by introducing the probability $W(z',\tau)$ that a particle at position z at time t will diffuse

to position $z + z'$ at time $t + \tau$. If the concentration at time t is known everywhere, then the concentration after time τ can be written as:

$$\delta(z, t + \tau) = \sum_{all\ z'} \delta(z - z', t) W(z', \tau) \tag{A.102}$$

This equation accounts for particles arriving at location z from all other locations $z - z'$. Expanding the concentration terms as a Taylor series,

$$\delta(z, t + \tau) = \delta(z, t) + \tau \frac{\partial \delta}{\partial t} + \dots \tag{A.103}$$

and

$$\delta(z - z', t) = \delta(z, t) - z' \frac{\partial \delta}{\partial z} + \frac{z'^2}{2} \frac{\partial^2 \delta}{\partial z^2} + \dots \ . \tag{A.104}$$

Plugging these two expressions into Equation A.102,

$$\begin{aligned} \delta(z, t) + \tau \frac{\partial \delta}{\partial t} + \dots = \delta(z, t) \sum_{all\ z'} W(z', \tau) - \frac{\partial \delta}{\partial z} \sum_{all\ z'} z' W(z', \tau) \\ + \frac{1}{2} \frac{\partial^2 \delta}{\partial z^2} \sum_{all\ z'} z'^2 W(z', \tau) + \dots \ . \end{aligned} \tag{A.105}$$

At time τ, the particles must exist somewhere in space, so by the definition:

$$\sum_{all\ z'} W(z', \tau) = 1. \tag{A.106}$$

We can use the definition of averages to write:

$$\sum_{all\ z'} z' W(z', \tau) = \langle z' \rangle, \tag{A.107}$$

and

$$\sum_{all\ z'} z'^2 W(z', \tau) = \langle z'^2 \rangle. \tag{A.108}$$

The angular brackets $\langle \quad \rangle$ represent a statistical average. Using Equations A.103 to A.108, we rewrite Equation A.102 in the same terms as the basic diffusion equation (Equation A.57):

$$\frac{\partial \delta}{\partial t} = \frac{\langle z'^2 \rangle}{2\tau} \frac{\partial^2 \delta}{\partial z^2} - \frac{\langle z' \rangle}{\tau} \frac{\partial \delta}{\partial z}. \tag{A.109}$$

Comparing Equations A.57 and A.109, we can write statistical expressions for the diffusion coefficient and the velocity:

$$v = \frac{\langle z' \rangle}{\tau} \tag{A.110}$$

$$D = \frac{\langle z'^2 \rangle}{2\tau}. \tag{A.111}$$

Equation A.111 can be rearranged as:

$$\begin{aligned} \langle z'^2 \rangle^{\frac{1}{2}} &= \sqrt{2D\tau} \\ &= \sigma \end{aligned} \tag{A.112}$$

This equation is equivalent to the diffusion length σ. Equation A.112 gives some insight into the statistical meaning of the diffusion length as the root mean square of the vertical

distance moved z'. This understanding aligns with our discussion of diffusion length in earlier chapters as the average vertical distance moved by a water molecule relative to its initial position post-deposition.

BIBLIOGRAPHY

Cuffey, K. M. and Steig, E. J. (1998). Isotopic diffusion in polar firn: Implications for interpretation of seasonal climate parameters in ice-core records, with emphasis on central Greenland. *Journal of Glaciology*, 44(147), 273–284.

Johnsen, S. J. (1977). Stable isotope homogenization of polar firn and ice. *Isotopes and Impurities in Snow and Ice*, 201–219.

Johnsen, S. J., Clausen, H. B., Cuffey, K. M., Hoffmann, G., Schwander, J. and Creyts, T. (2000). Diffusion of stable isotopes in polar firn and ice: The isotope effect in firn diffusion. *Physics of Ice Core Records*, 121–140.

Lasaga, Antonio C. Kinetic theory in the earth sciences. Princeton University Press, 2014.

Strang, Gilbert. The Heat Equation and Convection-Diffusion. "Mathematical Methods for Engineers", MIT Course, 2006. http://ocw.mit.edu/courses/mathematics/18-086-mathematical-methods-for-engineers-ii-spring-2006/readings/am54.pdf

Whillans, I. M., and Grootes P. M. (1985). Isotopic diffusion in cold snow and firn. *Journal of Geophysical Research*, 90(D2), 3910–3918.